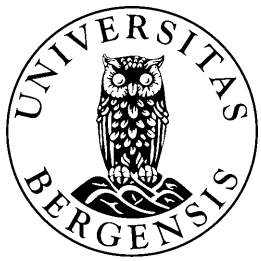

Candidatus Scientiarum Thesis

High-Latitude Boundary Phenomena and Magnetospheric Processes During the January 9-12 1997 CME Event: NOAA-12, Wind and Groundbased Observations

by

Kjellmar Oksavik

Department of Physics
University of Bergen
August 1998

Nordlyset

i sin evig vekslende skjønnhet

flammer over himmelen...

Se på det,

drikk glemsel og drikk håp av det

- det er selv som den higende menneskesjel.

Som dens irrende uro vil det omspenne

den hele hvelving;

blir dog bare glitrende lysflukt.

I sin ville lek vakrere enn alt,

vakrere enn morgenrøden

- men det bærer ikke bud om dagens komme -

Fridtjof Nansen, 1894
(In Norwegian)

***THE AURORAL STATION**, Longyearbyen, January 28 1998*

Preface

Acknowledgements

The interesting cand.scient. project leading to this thesis has been the first very close cooperation between the Space Physics group here at UiB and the University Courses on Svalbard (UNIS). Therefore, I would like to thank my excellent supervisor professor Finn Søraas, who came up with this splendid idea, and associate professor Jøran Moen, UNIS, for fruitful discussions and provision of groundbased optical data from Svalbard and facilities during my stays in Longyearbyen. Both have been very interested, understanding and helpful. Secondly, I would also like to thank Dr. Dave Evans, Space Environment Center, Boulder, Colorado, who kindly provided us with NOAA-12 and NOAA-14 data.

Fellow Dag Lorentzen, UNIS, and chief engineer Bjørn Lybekk, UiO, have contributed with documentation and information. Elisabeth Thorsen, UiB, has processed the PIXIE images. Cand.scient. Gard Atle Skauge, UiB, has most kindly helped me solving my MATLAB and FrameMaker problems. The WWW has also been useful to get information, especially the CDA-web, where all the Wind satellite data is taken from. The principal investigators of the Wind experiments are: R. Lepping (MFI), K. Ogilvie (SWE) and R. Lin (3-DP).

This thesis is written in FrameMaker 5.0. A software package was also written for MATLAB 5.0 to plot the NOAA satellite data. However, this several MB of source code is not listed here of space limitations. The other plots were also created using mostly MATLAB 5.0 and some IDL.

During my studies I have been three times to Svalbard, and I have participated and talked at to conferences; *"NATO ASI"* in Longyearbyen, June 4-13 1997 and "FYSIKERMØTET 1998" in Oslo, June 10-12 1998. For financial support I would therefore like to thank:

- The Space Physics group, the University of Bergen
- The Faculty, the University of Bergen
- NATO
- The Norwegian Physical Society

Not to be forgotten are my supportive family and friends.

Kjellmar Oksavik
Bergen, August 1998

Table of Contents

Chapter 1

INTRODUCTION

A brief presentation of the background of this thesis and its present composition

1.1 Space Physics

1.1.1 The Sun

The Sun, being the centre for the Earth's annual circulation, is the main energy source of the whole Solar-system. All life at the Earth is maintained by the solar power in the light emissions through the photosynthesis. The Sun emits electromagnetic radiation over a wide frequency spectrum; visible light, X-rays, UVs and IRs. The Sun also works as an important source supplying highly ionized plasma into the interplanetary medium. Trough the Sun's interplanetary magnetic field (IMF), reconnected to the terrestrial magnetic field, many interesting and yet not well understood processes take place when the solar plasma interact with the Earth.

1.1.2 The Aurora Borealis

The perhaps most famous process is the Aurora Borealis, "The Northern Lights", caused by charged particles streaming down along the magnetic field in both the northern and southern hemisphere giving raise to optical emissions from the upper atmosphere, the ionosphere.

1.1.3 The Dayside Aurora

The region where the Sun-Earth connection is believed to be most direct is in the geomagnetic dayside near the polar cusps. Here, the IMF is able to merge with terrestrial field lines and transport solar wind plasma along open magnetic field lines directly down into the ionosphere. However, the rate at which this process take place, the spatial extent and the relative importance are still discussed. Other processes like diffusion and viscous interaction, transferring plasma across closed field lines, are also matters of actual concern. Therefore, it is of great importance to decide this degree of coupling, and the major clue is to precisely specify the open/closed field line boundary.

The most straight forward method in theory; to track the magnetic field lines through simultaneous multi-point magnetic field measure-

ments, is both very expensive (require hundreds or thousands of simultaneous operating satellites) and is in practice quite impossible. However, by using known particle characteristics and the particles tracing the magnetic field much information may still be gained about the magnetic field structure and the open/closed boundary. In combination with optical observations from the ground, this constitute a major tool to explore these phenomena.

Svalbard has proved to be the ideal location for such studies. The perfect geomagnetic location and the pre-existing local infrastructure have resulted in the University Courses on Svalbard (UNIS) and several scientific installations. EISCAT ESR, the Auroral Station and the optical site in Ny Ålesund combined with spaceborn measurements have all contributed to major discoveries of the high-latitude dayside aurora during the later years, and still will.

The dayside aurora was first studied by the Russians in the 1960s, [e.g. Feldstein and Starkov, 1967]. From all-sky camera films they found the high-latitude dayside aurora to shift equatorward during increased geomagnetic activity. Later [Vorobjev et al., 1975] reported dayside poleward moving forms: *"Individual auroral forms of auroras move towards the pole; each form exists for 5-10 min, rises at the equatorial boundary of the luminescence region and disappears after a poleward drift of two degrees."* A decade later, [e.g. Sandholt et al., 1986] also reported poleward moving auroral forms ("the midday breakup"), where the direction of motion is controlled by the IMF By component, [e.g. Sandholt et al., 1993]. Most recently, [Sandholt et al., 1998] have classified the dayside aurora into different types.

From the launch of the first satellites into polar orbits in the late 1960s, the particle population at the geomagnetic dayside has been investigated. These particle observations soon revealed the existence of different regions in the high-latitude magnetosphere. Some of the first signs of a dayside polar cusp region (although not first reported) were probably found in particle observations from the ESRO IA and IB satellites. [Søraas, 1972; Søraas et al., 1977, Figure 6; Søraas et al., 1980] show some examples of these low altitude ESRO satellite passes. Nevertheless, these papers were not the earliest ones to report observations of this region. [Heikkila and Winningham, 1971] and [Frank, 1971] first published observations of the cusp in low and high altitudes, respectively. Heikkila and Winningham presented observations of soft electrons and protons from the polar orbiting Isis 1 satellite, while Frank used the Imp 5 satellite.

Later, the dayside particle precipitation has been further studied and divided into regions. The automatic classification of the dayside particle precipitation into regions; cusp, LLBL, mantle, BPS and CPS by [Newell and Meng, 1992; Newell and Meng, 1994] has contributed to the general understanding of these dayside magnetospheric regions.

1.2 January 9 to 12, 1997

1.2.1 "The Practice of Space Physics"

On January 11 1997 a $200 million geosynchronous communication satellite suddenly failed. A press release from AT&T January 15 1997 stated: *"The Telstar 401 satellite experienced an abrupt failure of its telemetry and communications this morning (01/11/97) at 6:15 a.m. Eastern Standard Time affecting service for all customers."* Afterwards it is not clear what actually happened, whether the

break down was directly caused by the disturbed conditions in space or if the actual time of failure was just a coincidence.

However, the huge economical aspects and the commercial interests involved clearly illustrates the needs and the importance of forecasting the space weather. [Maynard and Siscoe, 1998] have presented a brief overview of these efforts in predicting the space weather and some ideas for the future. To get reliable forecasts, good models are needed, and proper models must be based and tested on a huge amount of observations.

1.2.2 The CME Event

On January 10 1997 a huge cloud of fast-streaming high-energized plasma, a Coronal Mass Ejection, hit the Earth's magnetosphere. A review on Coronal Mass Ejections is given by e.g. [Crooker et al., 1997]. This gave the ideal situation for studies of the magnetospheric processes that take place both before, during and after a rapid and intense injection of plasma. In other words, this experiment-like event offered us some good opportunities to maybe understand some of the physics taking place in the magnetospheric and ionospheric environment.

1.2.3 The Purpose

The purpose of this thesis is to contribute to exactly that by first to present in-situ particle and solar wind data from the period January 9 to 12 1997 and then try to draw some conclusions from this huge data set. Furthermore, these data will be directly complemented with groundbased observations from Svalbard, when available. The major instruments used in the study are the TED and MEPED detectors on-board the NOAA-12 satellite, solar wind instruments on the Wind spacecraft and an All-Sky camera and two Meridian Scanning Photometers from Longyearbyen and Ny Ålesund. Observations from other instruments are introduced when suitable.

1.2.4 Outline

All the instruments used are presented in Chapter 2, before an overview of the whole January 9-12 1997 period, as observed by the Wind satellite and the TED and MEPED particle detectors on-board the polar orbiting NOAA-12 satellite, is given in Chapter 3. Chapter 4 provides a brief review of the different regions in the dayside aurora and presents some of the basic theories. Chapter 5 first introduces the groundbased optical observations from Svalbard. These measurements are then directly compared with NOAA-12 observations during five passes where the satellite track was within the field-of-view. These observations are also discussed and put into the context of previous work, before the conclusions and ideas of future work are outlined in Chapter 6. Undefined abbreviations can cause chaos, so a listing of those used in this thesis is given in Appendix A. Appendix B briefly summarizes the basic steps of a technique developed in Chapter 5 to transform from elevation angle at a groundbased station to the equivalent magnetic latitude. Finally, the references are listed.

1.3 Notation - Some Confusion

Often single terms may have several different interpretations. This can give raise to confusion, so an explanation may be necessary.

1.3.1 Proton or Ion

What do you call a positive-charged unspecified particle, an 'ion' or a 'proton'? By definition, the negative charged electrons make no confusion. A positive-charged particle makes

more trouble. From chemistry, ‘ions’ may be both negative and positive charged, and a ‘proton’ is often another word for the positive ionized hydrogen. Consequently, in this thesis I have just chosen to let the words ‘proton’ and ‘ions’ denote all the positive charged types of particles; hydrogen and heavier ions.

Chapter 2

INSTRUMENTATION

A brief overview of the space and ground instruments used in this study

2.1 The NOAA-12 Satellite

NOAA-12 was successfully launched from Vandenberg by an Atlas-E rocket on May 14 1991. The satellite got into an orbit with an inclination of 98.6^{o}, perigee of 804 km, apogee of 824 km and period of 101.2 min., see Figure 2.1.

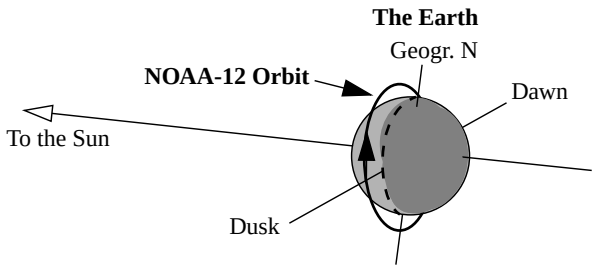

FIGURE 2.1 Sketch of the NOAA-12 orbit. An arrow indicates the direction of orbiting. The sketch shows how NOAA-12 always is lapping near the dusk-dawn meridian plane in an sunsyncrone orbit. (NOTE: The scaling of distances is incorrect.)

If the footprint coordinates is plotted in a magnetic local time vs. invariant latitude reference system, Figure 2.1 is confirmed. In Figure 2.2 the MLT/ILAT footprints from January 9-12, 1997 is displayed. This figure shows how NOAA-12 mostly passes the noon-midnight meridian slightly on the dayside for the northern hemisphere and on both the day- and nightside for the southern hemisphere.

NOAA-12 is 3.71 m long and 1.88 m in diameter, with a total mass of 735 kg in orbit. A 2.37 x 4.91 m^2 solar array is the power source, see Figure 2.3. The satellite has a designed lifetime of 3 years and a three axis stabilization [“The Satellite Encyclopedia”, WWW].

The US satellite NOAA-12 is an important part of the National Oceanic and Atmospheric Administration (NOAA) and Television and InfraRed Observation Satellite (TIROS) program. During the years, seven TIROS/NOAA satellites have been launched, and maximum two satellites have been operating at any time; one orbiting near the dusk-dawn meridian

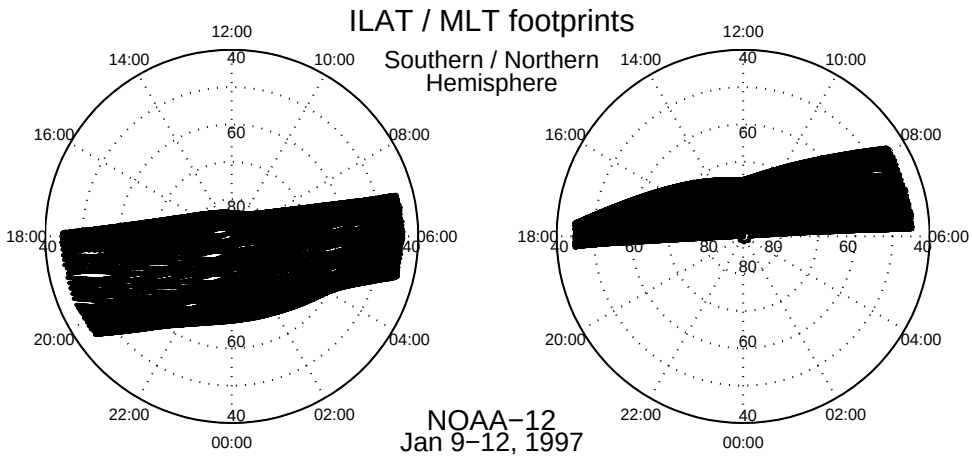

FIGURE 2.2 NOAA-12 MLT/ILAT footprints from January 9-12, 1997. The southern hemisphere is to the left and the northern to the right.

plane and the other near the noon-midnight meridian plane. The main purpose has been to do meteorological investigations.

Fortunately, the spacecraft also carry some equipment for studies of the environment in space. The Space Environment Monitor (SEM-2) is a multichannel charged-particle spectrometer sensing the fluxes of charged particles at the satellite altitude. Huge and rapid changes in the magnetospheric and ionospheric environment can result in a lot of problems for people both in space and at the ground. Huge fluxes of very high-energetic particles during extreme disturbed conditions is a danger both for astronauts (may develop cancer) and satellite electronics and solar panels in space. These particles can also have still unknown effects on the climate. Problems with radio communications, navigation and power supplies at the ground are some matters of actual concern too. Therefore, SEM-2 is designed to sense particles over a wide energy range, from 0.3 to 6900 keV. SEM-2 consists of the “Total Energy Detector” (TED) and “Medium Energy Proton and Electron Detector” (MEPED) detectors and a data processing unit (DPU), Figure 2.3.

2.1.1 The TED Detector

The Total Energy Detector (TED) measures the total energy electron and proton fluxes in the 300 eV to 20 keV energy range. Two independent measurements are made looking outwards at 0° and 30° from the local vertical, well within the atmospheric loss cone at mid- and high-latitudes*. Each measurement is also subdivided into 11 energy channels, shown in Table 2.1, and is done independently for both electrons and protons.

The detection principle is based on electrostatic analysers (ESA). The ESA is selecting particles according to their charge and energy using two curved plates at different electrical potentials. Only those particles of the appropriate charge and energy, can pass entirely through the ESA. At the outlet of the ESA, a Continuous Dynode Electron Multiplier (CDEM) produces a pulse for each particle passed by the ESA. By stepping the voltage

* The 0°channel usually detects particles with pitch angles less than ~15° and almost never larger than ~35°, while the 30° channel mostly observes particles with pitch angles in the ~40°-45° range and generally less than ~55°.

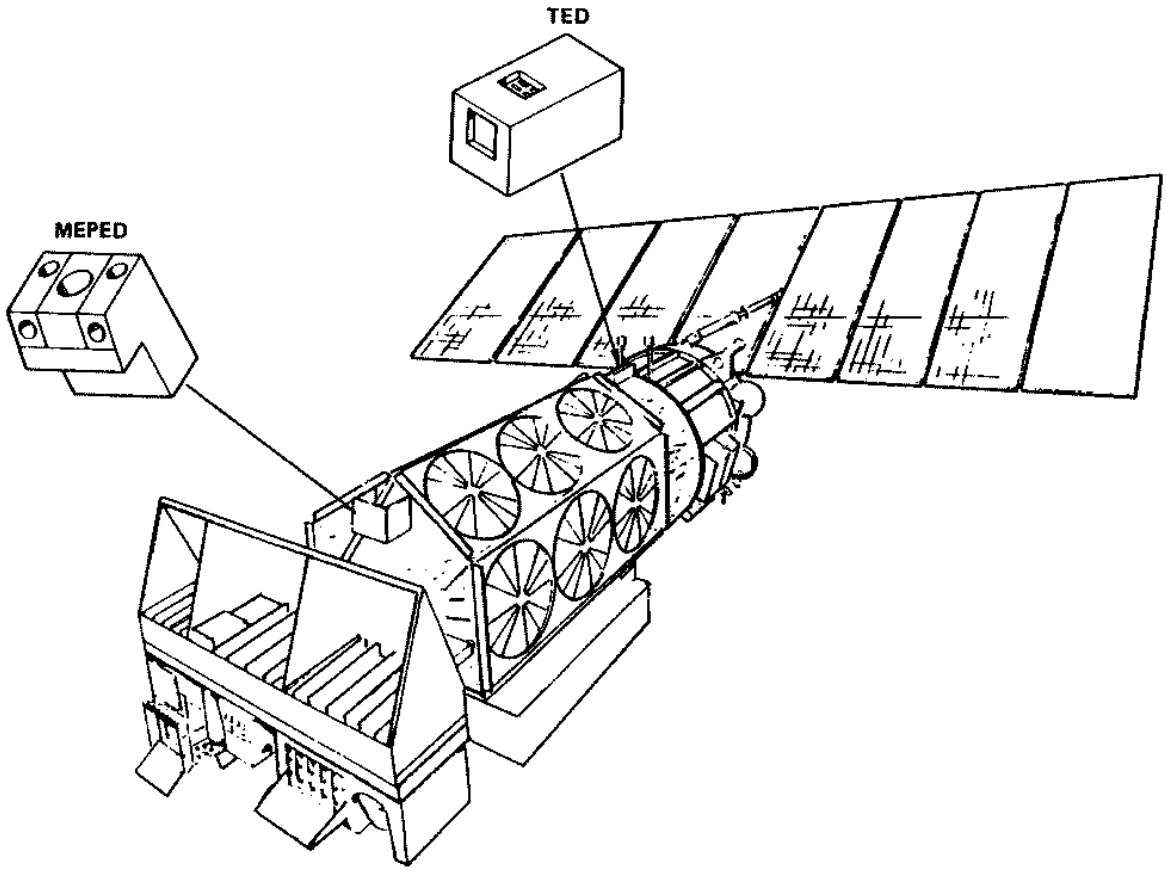

FIGURE 2.3 Sketch of the NOAA-12 satellite [Raben et al., 1995]. (The HEPAD sensor is removed.)

applied to the ESA curved plates through a series of exponential values, one can allow particles of increasing energy to pass through.

Four ESA detector systems are mounted in two pairs. The two detector systems within each pair are altered between measuring electrons and protons in a two second cycle. The first second of the cycle is devoted to measuring electrons, the second one protons, and so on. During each half cycle the detector system runs through the sequence in Figure 2.4. During the first 1/13 s the background is measured. In the following 11/13 s the analysers sweep through Channel 1 to 11 integrating 1/13 s at each channel. The last 1/13 s of the half cycle the instrument is reset and no data is taken, before the procedure repeats, measuring the other particle type instead.

Every 2 s the maximum of counts accumulated in the 11 channels and the corresponding channel number where this occurred is transmitted from both detector pairs and particle species. The four channel numbers then give the characteristic energies. In addition, the counts from the channels 1, 3, 5 and 7 (indicated in Table 2.1 by the *'s) are also telemetried to the ground almost every 8 s[†].

[†] Every fourth 8 s interval the background measurement from each detector is transmitted instead. Therefore, the final transmission sequence is 8, 8, 8 and 16 s.

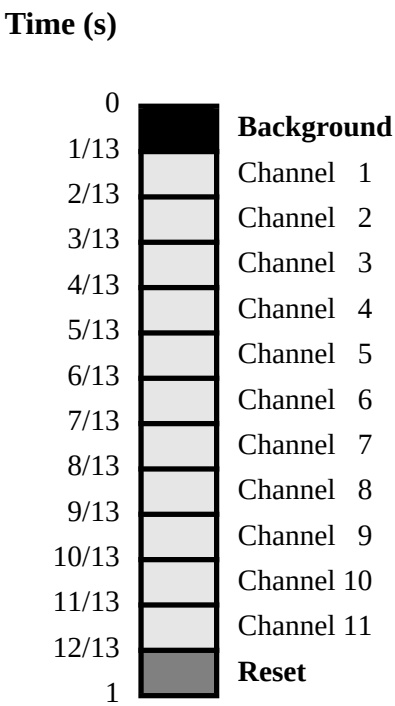

FIGURE 2.4 One half for the TED duty-cycle. The duty cycle is repeated once more.

2.1.2 The MEPED Detector

The Medium Energy Proton and Electron Detector (MEPED) provides both directional and omni-directional measurements. The three omni-directional Proton Sensors are in the 16 to 215 MeV energy range, but they are not used in this study and will not be commented on.

The directional sensors, called telescopes, make independent measurements of electrons and protons. The geometric factor for all the directional telescopes is 9.5×10^{-3} cm^2 sr, and the directional measurements are made pointing outwards from the Earth at 10 degrees and 80 degrees to the local vertical, which corresponds to observing precipitating and trapped particles, respectively. This is e.g. seen from the atmospheric loss cone α_{850} at the spacecraft's altitude, given by:

$$\sin\alpha_{850} \leq \sqrt{\frac{B_{850}}{B_{120}}} \qquad (2.1)$$

where B_{850} is the geomagnetic field strength at the spacecraft's altitude and B_{120} at the magnetic mirroring point of the last trapped particle. Assuming a magnetic mirroring point in 120 km altitude, from Equation 2.1 the atmospheric loss cone is found to be 45^o to 50° in 850 km altitude in the northern hemisphere above 50° geographic latitude. The 10° detector is generally observing particles with pitch angles less than ~15° and never larger than ~30°, while the 80° detector always is detecting particles with pitch angles larger than 65°, generally larger than 80°.

The two electron telescopes contain a single 700 μm thin 25 mm^2 solid state detector (SSD) each. The SSD is covered by a 0.51 μm nickel foil, reducing the detector's response to photons, low-energy electrons (<10 keV) and protons up to about 150 keV. Pulse-height discrimination gives three energy thresholds from 30 keV to 300 keV, see Table 2.2. Each integral energy band has an upper energy limit of 1000 keV.

The two proton telescopes are each containing two solid state detectors (SSD). The front SSD has an effective area of 25 mm^2 and thickness of 200 μm, and the back one an effective area of 50 mm^2 and thickness of 200 μm. A 2500 nT magnet is mounted across the input of the telescope to prevent any less than 1.5 MeV electrons from reaching the SSD detectors. The front detector is coated with an 18 μg/cm^2 aluminium layer to reduce the detector's sensitivity to photons, and this layer also serves as an electrical contact. On average, a 50 keV to 200 keV proton deposit only about 8 keV in this very thin aluminium layer. The lower and

Channel Number	Energy range (eV)	Centre energy (eV)
*1	300-458	379
2	458-773	616
*3	773-1088	931
4	1088-1718	1403
*5	1718-2349	2033
6	2349-3610	2979
*7	3610-4870	4250
8	4870-7392	6131
9	7392-9914	8653
10	9914-14957	12436
11	14957-20000	17479

TABLE 2.1 The energy range covered by the NOAA-12 electron and proton TED detector, [Raben et al., 1995]. (A * means that the fluxes from this channel is telemetried to ground.)

Particle	Energy (keV)
Protons	30 - 80
	80 - 250
	250 - 800
	800 - 2500
	> 2500 integral
Electrons	> 30 integral
	> 100 integral
	> 300 integral
Ions (Z ≥ 2)	6000-55000

TABLE 2.2 Energy range for the MEPED 10 and 80 degrees directional sensors, [Raben et al., 1995].

higher energy protons deposit even less energy. Thus, pulse-height discrimination and coincidence logic is used to select four differential energy bands from 30 to 2500 keV and one integral channel for energies larger than 2.5 MeV, see Table 2.5.

The noise levels of the TED and MEPED detectors are both very low, comparable with the minimum count-rate, and can thus be ignored in the discussion. A more complete description of both the satellite and the instruments onboard is given by [Raben et al., 1995].

2.2 Groundbased Instruments at Svalbard

In 1978 The Auroral Station ("Nordlysstasjonen") was built in Adventdalen just outside Longyearbyen at Svalbard. The Auroral Station is an optical site for ground-based observations of the dayside and nightside auroral activity above Svalbard. The University of Tromsø is the owner of the site, and the Optics Group at the Geophysical Institute at the University of Alaska contributes both with instruments and finances. From the opening of the University Courses on Svalbard (UNIS) in 1993, the Geophysics Group at UNIS now also has become a significant user of the Station in teaching, scientific research and the daily maintenance of the Station.

At the Auroral Station several instruments are more or less continuously running each winter; a flux gate magnetometer, several All-Sky Cameras (ASC), a Meridian Scanning Photometer (MSP) and several spectrometers/ spectrographs. Some kilometres further up the Advent valley, on the Mine-7 mountain, the Svalbard EISCAT radar is situated, but the ESR was not running during the actual period studied and is omitted here.

2.2.1 The All-Sky TV Camera

The Auroral Station has an All-Sky TV Camera (ASC) operating primarily at the 630.0 nm red line-emissions from oxygen[‡]. This is the UiO/UNIS camera, owned by UiO and maintained and driven by UNIS. The instrument is described in [Moen and Lorentzen, 1997].

The processing of the All-Sky Camera data from the real image as seen by the camera, to the transformed image projected down onto the map, is done by running the GeoMapper programme on a PC. UNIS has this software installed on one of their computers. The programme takes the geographical position of the observing camera and the assumed height of the auroral emissions as input (250 km altitude is used). Then, for each pixel in the real image, the corresponding position for the emissions is calculated and projected onto the map.

Note: It is important to be careful in using this method, as noted by [Moen et al., 1995]. The assumption of the emissions only coming from a very thin layer is not the real case. In fact the emissions have a certain extent in height. Therefore, possible errors caused by spurious effects are introduced. [Moen et al., 1995] mention that east-west elongated rayed arc structures moving in the east-west direction may lead to an artificial rotation. Also the question of which assumed height to be chosen for the emissions, is not straight forward. A to high height causes a to large radial distance from the observing station on the final map. However, using this technique carefully gives a good indication of where the emissions took place and makes it more easy to directly

[‡] In January 1997 only the 630.0 nm channel was operative. From the winter season 1997/1998 several extra bands were included, e.g. 557.7 nm and 427.8 nm.

compare optical observations with observations onboard a spacecraft.

2.2.2 The Meridian Scanning Photometer - Longyearbyen

The Auroral Station also had a Meridian Scanning Photometer (MSP) running. This was the University of Alaska Fairbanks MSP. Scanning along the north-south magnetic meridian from horizon to horizon, the Longyearbyen MSP easily display the north-south motion of the aurora. The main scientific objective of this MSP is to identify the local time position of the ionospheric signatures of the separatrix and the cusp [Moen and Lorentzen, 1997]. A second purpose is to use the MSP in Longyearbyen in conjunction with the MSP in Ny Ålesund to determine the auroral heights.

The Longyearbyen MSP spends 16 sec to make one scan and has a spatial resolution of 1 angular degree. The spectral resolution is typically 0.4 nm [Moen and Lorentzen, 1997]. During the winter 1996/1997 the MSP was operating in four wavelengths; 630.0 nm, 557.7 nm, 486.1 nm and 427.8 nm.

2.2.3 The Meridian Scanning Photometer - Ny Ålesund

There was also one MSP active in Ny Ålesund. The Ny Ålesund MSP was operating at 630.0 nm and 557.7 nm. However, this MSP was not scanning from horizon to horizon. Instead, on January 12 1997 the MSP was scanning from 10 to 165 degrees from the northern horizon along the magnetic meridian (personal communication with Bjørn Lybekk, UiO, spring 1998).

2.2.4 Optical Field-of-View

Figure 2.5 displays the Ny Ålesund and Longyearbyen geographic field-of-view when the emission altitudes of 250 km and 120 km are assumed. These heights are typical for the 630 nm and 557 nm bands, respectively, and they are consistent with the discussion in Section 5.4. In doing the projections a curved Earth and emission layer is assumed, cf. Appendix B.

The Ny Ålesund MSP (the red line and labels) was scanning from 10 to 165˚ from the northern horizon as shown in Figure 2.5, while the Longyearbyen MSP (the blue line and labels) was scanning from 0 to 180˚ (in fact outside the figure display). However, the observations made at these very low elevation angles (<10˚ from the horizons) are of little value and are ignored. In Figure 2.5 the circular UiO/UNIS All-Sky TV camera geographic field-of-view is also projected to 250 km altitude for reference. Due to a low detection efficiency at very low elevations these ASC images are usually cut at 70˚ from zenith before the projection. Therefore, in Figure 2.5 the ASC field-of-view is shown for zenith angles <70˚.

From Figure 2.5 the latitudinal width per 1˚ elevation increases as the MSP line-of-sight approaches one of the horizons. For a higher altitude this effect becomes even more visible. This effect is also the reason for only showing the Longyearbyen MSP intensities at >15˚ above the horizons in Section 5.4.2, equivalent to 15-165˚ from the northern horizon.

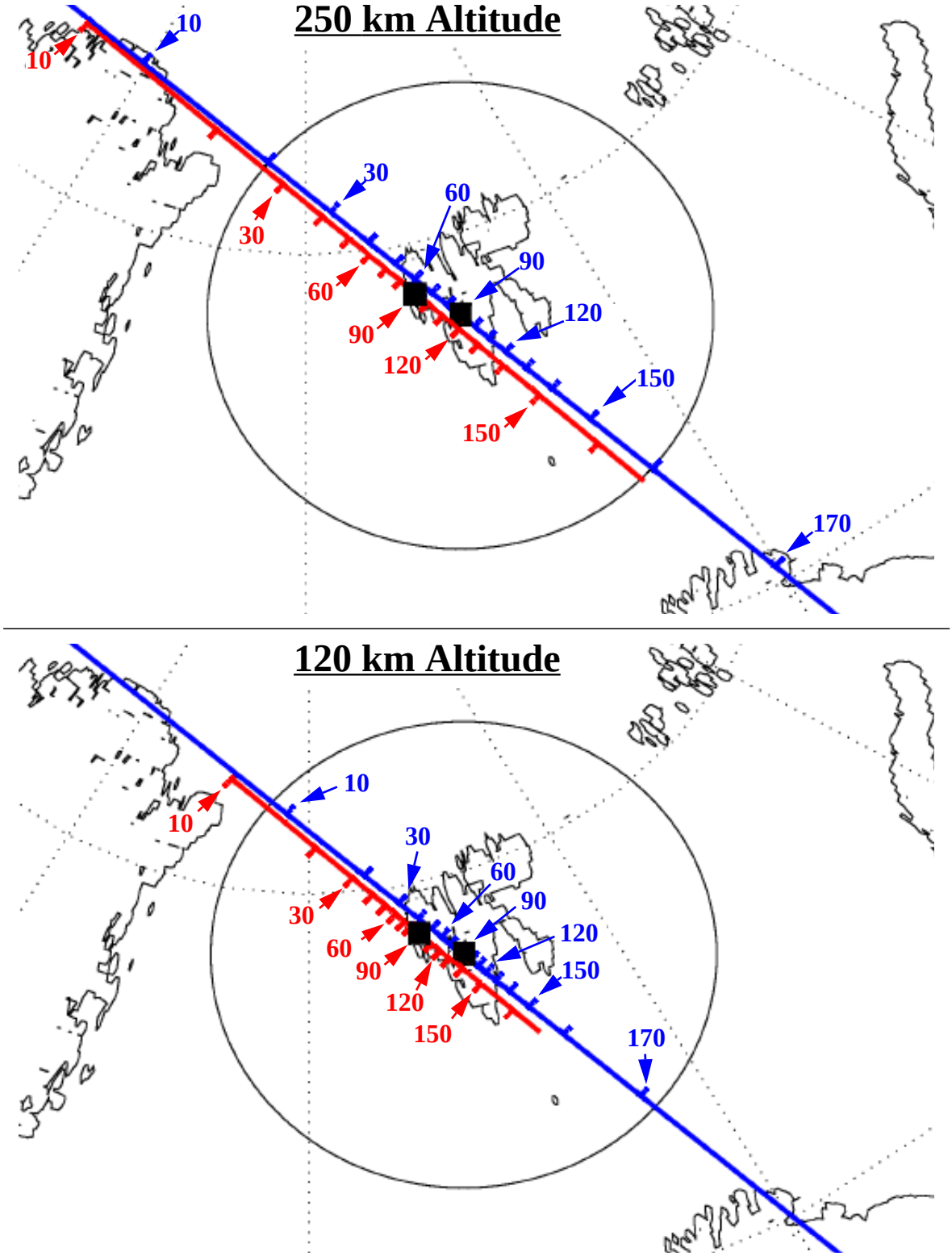

FIGURE 2.5 **Ny Ålesund** and **Longyearbyen** MSP elevation angles (from the northern horizon) projected to 250 km and 120 km altitude. The UiO/UNIS 630 nm ASC field-of-view (within 70˚ from zenith at Longyearbyen) is projected to 250 km altitude for reference.

2.3 The Wind Spacecraft

Wind was launched from Cape Canaveral, USA, November 1 1994 at 23:31 UTC as a part of the International Solar Terrestrial Physics (ISTP) program. Wind has a designed lifetime of three to five years, and the main purpose is to measure the incoming solar wind, magnetic fields and particles. Wind is cylindrical, approximately 2.8 m in diameter, and 1.25 m high and has a mass of 1250 kg, see Figure 2.6. The spacecraft is spin-stabilized and has a spin rate of 20 rpm around an axis within 1° of the normal to the ecliptic plane. The Wind spacecraft is further described in [Harten and Clark, 1995] and by the [*"NSSDC Master Catalog Display Spacecraft"*, WWW].

The first nine months of operation, Wind was placed in a double-lunar swingby orbit near the ecliptic plane, with the apogee from 80-250 Re and the perigee between 5-10 Re. This orbit was achieved by making use of the lunar gravity. During January 9-12 1997 Wind was on its way towards the apogee, moving from $\{X_{GSE} = 75, Y_{GSE} = -61, Z_{GSE} = -2\}$ to $\{108, -53, -6\}$.

Later, Wind was inserted into its final orbit about the sunward Sun-Earth gravitational equilibrium point (L1), varying from 235- 265 Re. In this orbit Wind continuously measures the incoming solar wind, magnetic fields and particles and provides an approximately one-hour warning to the other ISTP spacecraft of changes in the solar wind.

Wind contains 8 instruments which consists of 24 separate sensors, [Harten and Clark, 1995]. However, only three of the instruments are used here:

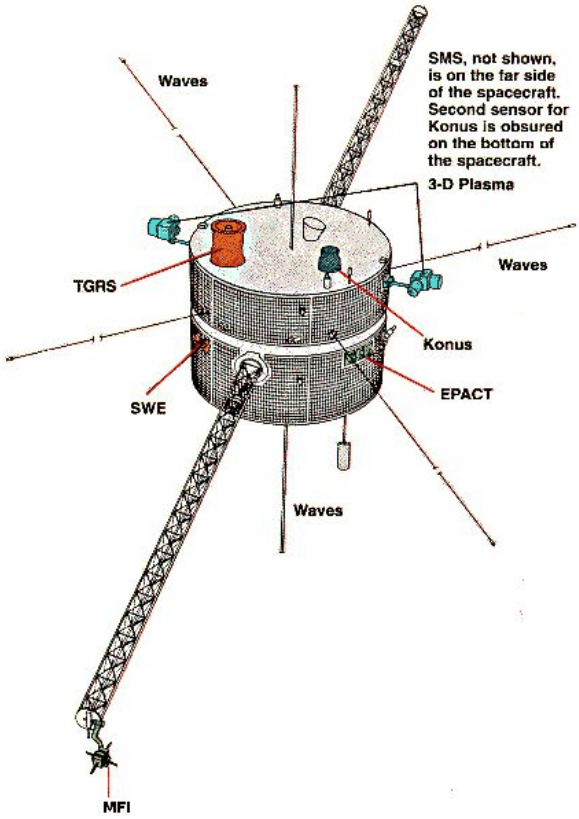

FIGURE 2.6 The Wind spacecraft, from [*"NSSDC Master Catalog Display Spacecraft"*, WWW].

2.3.1 The Magnetic Field Investigation (MFI)

The Magnetic Field Investigation (MFI) experiment is described by [Lepping et al., 1995]. The basic instrument is a boom-mounted dual triaxial fluxgate magnetometer and associated electronics. The instrument provides:

1. Near real-time data as "Key Parameter Data' (nominally one magnetic field vector per 92 s)
2. Rapid data (10.9 samples of the magnetic field vector each second)

3. Snapshot memory data and Fast Fourier Transform data based on 44 magnetic field vectors per second

Only the first group of the interplanetary magnetic field observations is presented in this thesis. R. Lepping (NASA/GSFC) is the Principal Investigator (PI) of the MFI experiment.

2.3.2 The Solar Wind Experiment (SWE)

The Solar Wind Experiment (SWE) is presented by [Ogilvie et al., 1995]. This experiment consists of:

1. Two Faraday cup (FC) sensors (150 eV-8 keV)
2. A vector electron and ion spectrometer (VEIS) (7 V-24.8 keV)
3. A 'strahl' sensor (studying the electron 'strahl' close to the magnetic field direction)
4. An on-board calibration system

The 'Key Parameters' (velocity, density and temperature) of the solar wind is extracted from detailed three-dimensional measurements made by the Faraday cup. The solar wind most probable thermal speed $\sqrt{2kT/M}$ and the solar wind velocity in GSE-coordinates are presented in this thesis. K. Ogilvie (NASA/GSFC) is the Principal Investigator (PI) of the SWE experiment.

2.3.3 The 3-D Plasma (3-DP)

The 3-D Plasma (3-DP) experiment is explained by [Lin et al., 1995]. This experiment first of all provides measurements of solar wind electron and ion velocities, temperatures and densities, as well as suprathermal electron and ion fluxes in four energy bands. However, in this thesis only the electron and ion densities and temperatures are presented. R. Lin (UC Berkeley) is the is the Principal Investigator (PI) of the 3-DP experiment.

Chapter 3

January 9-12, 1997

An overview of the interplanetary conditions from Wind and the NOAA-12 electron and proton observations during the CME-event January 9-12, 1997

3.1 The CME Event

On January 6 1997 the first signs of a "Halo" Coronal Mass Ejection (CME) was observed around 16 UT in coronagraphs* from the SOHO spacecraft. Figure 3.1 shows an image of the solar corona obtained at 18:50 UT. This event developed into a huge magnetic bubble, a magnetic cloud, formed by a strong magnetic field. Inside, the strong magnetic pressure balances the gas pressure resulting in a lower density, however at the surface the density increases, and in front of the magnetic bubble a shock wave is created.

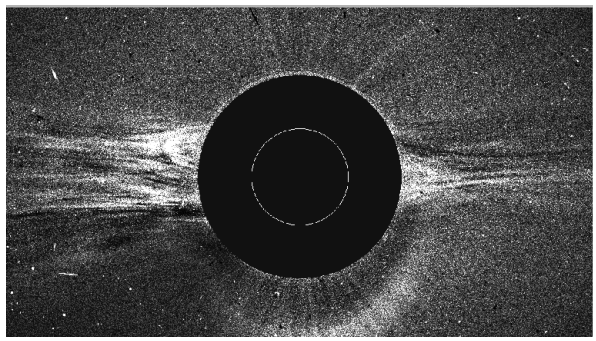

FIGURE 3.1 SOHO-LASCO/C2: A "Halo" CME at 18:50 UT on January 6 1997. [ISTP Sun-Earth Connections Event Solar Observations, WWW]

Some days later, on January 10 this event passed SOHO (X_{GSE} ~ 230 Re) on its way towards the Earth. At 00:10 UT a first sudden rise in the solar wind speed and density was observed, and a second jump was seen at 04:30 UT. These changes were also observed by the Wind spacecraft (X_{GSE} ~85 Re). A shock front was detected about 01:00 UT followed by a magnetic cloud around 04:30 UT. When hitting the Earth, it worked as a great source of energy effecting the particle populations in the magnetosphere. Therefore, we should expect huge changes in the fluxes of both trapped and precipitating particles.

* A coronagraph is a specially designed telescope using a blocking disk in front of the aperture lens.

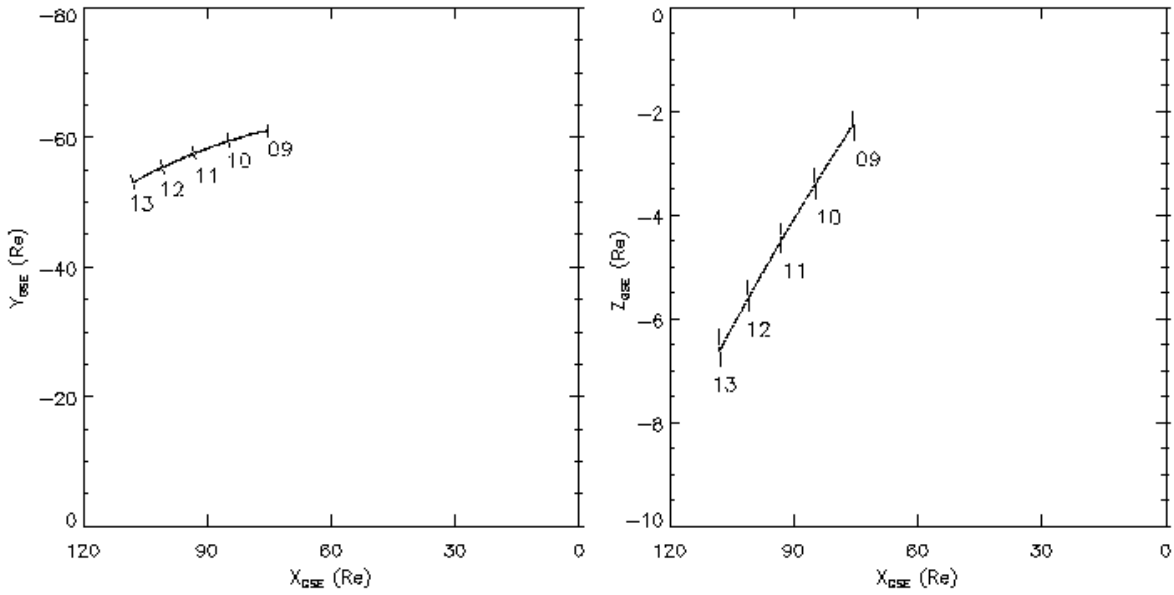

FIGURE 3.2 The orbit of the Wind spacecraft January 9-12 1997.

3.2 Interplanetary Conditions

First of all, an overview of what is believed to be some of the most important magnetospheric input parameters, the interplanetary conditions, is very useful. The Wind spacecraft, as described in Section 2.3 on page 23, is well suited for measuring the solar wind parameters. During January 9 to 12 1997 Wind moved sunwards in GSE-coordinates† from $\{X_{GSE} = 75, Y_{GSE} = -61, Z_{GSE} = -2\}$ to {108, -53, -6}, see Figure 3.2.

3.2.1 Wind Data

The solar wind parameters from January 9 to 12 1997 from Wind are shown in Figure 3.3. Some important features are seen in the interplanetary magnetic field components in the upper panel:

- The first one is the very long southward directed IMF, where IMF Bz is constantly negative from 04:41 to 16:21 UT on January 10 followed by a northward IMF from 16:21 UT on January 10 to 02:58 UT on January 11.
- The second one is the continuous negative IMF By starting at 07:52 UT on January 10 and ending at 02:04 UT on January 11.
- The third one is the IMF Bx-component being negative from 05:53 UT on January

† The Geocentric Solar Ecliptic (GSE) coordinate system. The X-axis always points from the Earth towards the Sun, while the Z-axis points towards the ecliptic North Pole. During the year this system thereby rotates, however the diurnal rotation is very small. This system is therefore well suited for referencing data of solar wind and interplanetary magnetic field. (For a complete listing of frequently used coordinate systems and how to transform between different systems, see [Hapgood, 1992].)

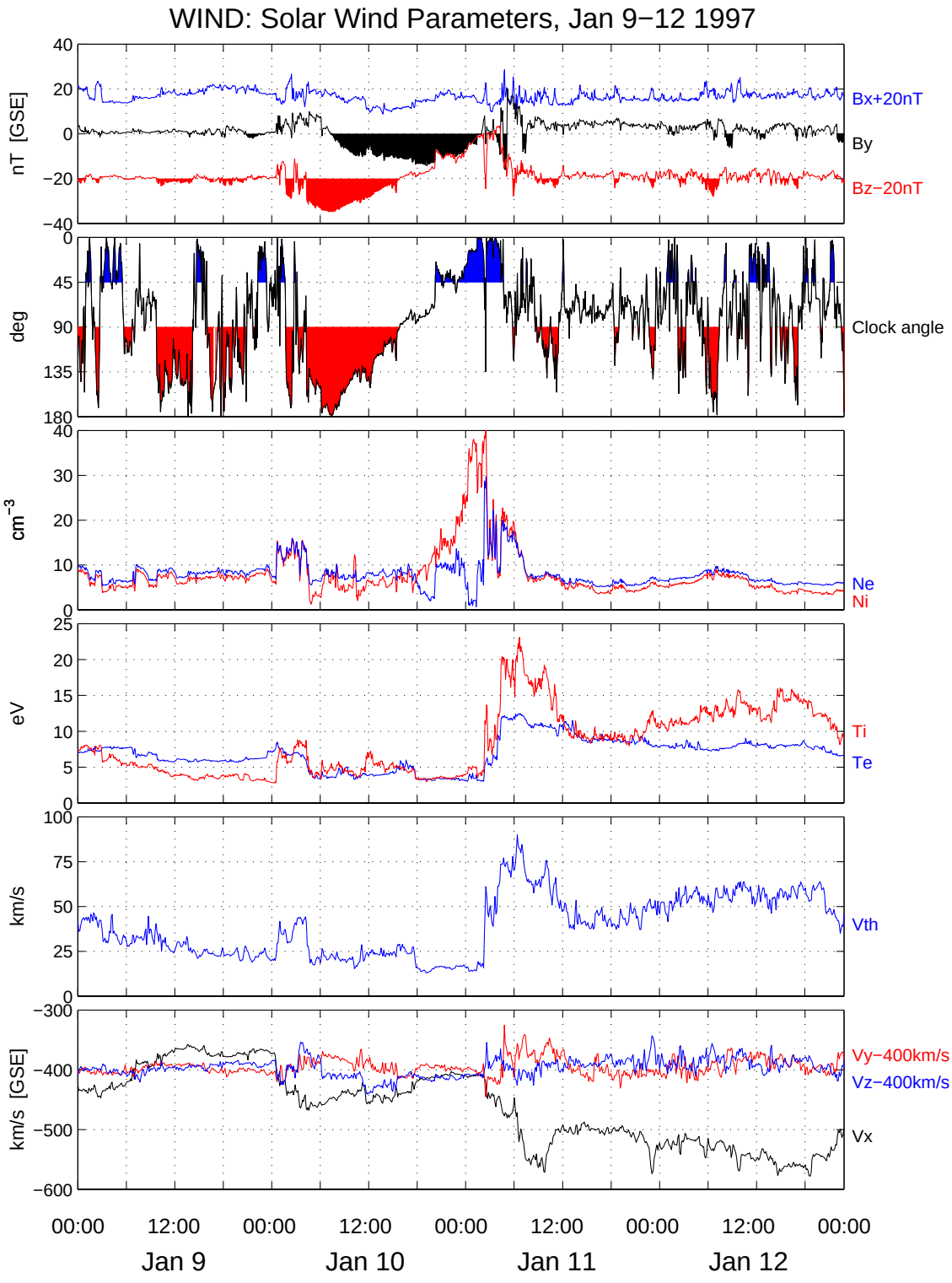

FIGURE 3.3 Some useful Solar Wind Parameters from the Wind spacecraft during the CME-Event, January 9 to 12, 1997. The times when the IMF By and Bz components are negative, and when the IMF clock angle is < 45° and > 90° have been shaded. (The data set has been run through a low-pass filter, since the most rapid fluctuations are not of interest here.)

10 to 02:58 UT on January 11. (The latter being the same time as the IMF became very weak, which is called a magnetic hole.)

More features may also be noted in the panels 3 to 6 of Figure 3.3:

- The very low minimum in the electron density in panel two of ~1-2 electrons/cm^3 at 00:53 to 01:59 UT on January 11, followed by a very intense peak of ~20-35 electrons/cm^3 at 02:54 to 03:17 UT.
- The peak in the ion density in panel three of ~20-47 electrons/cm^3 at 23:34 UT January 10 to 03:20 UT January 11.
- The peak in the electron temperature in panel four of ~10-13 eV at 04:58 to 11:56 UT January 11 and the corresponding peak in the ion temperature of ~15-25 eV at 04:58 to 11:11 UT on January 11.
- The rapid change in the solar wind most probable thermal speed in panel five from well below 25 km/s to well above 50 km/s at 02:56 UT on January 11. The thermal speed stayed high for the whole rest of the period, January 11 to 12, and reached a maximum value of nearly 100 eV at 06:30 and 07:06 UT on January 11.
- The increase in the anti-sunward solar wind velocity, in the negative GSE X-direction, seen at 04:01 UT on January 11, where the Vx gets smaller than -450 km/s. Vx stayed less than -450 km/s for the rest of the period, January 11 and 12, and several times nearly reached -600 km/s. The Vy- and Vz-components mostly stayed in the interval -50 to 50 km/s, most often very near 0 km/s, all the actual days.

3.2.2 The IMF Clock Angle

In the second panel of Figure 3.3 the IMF clock angle is displayed. The clock angle θ is defined here simply as by [e.g. Sandholt et al., 1998]:

$$\theta = \begin{cases} \operatorname{atan}\left(\left|\frac{B_y}{B_z}\right|\right) & \text{for Bz} > 0 \\ 180^\circ - \operatorname{atan}\left(\left|\frac{B_y}{B_z}\right|\right) & \text{for Bz} < 0 \end{cases} \quad (3.1)$$

Here B_y and B_z are the Y and Z components of the IMF, respectively. Therefore, the clock angle gives the rotation of the IMF in the Y-Z plane. 0° (180°) clock angle denote strongly northward (southward) IMF, while 90° clock angle indicate a dominating By component and the Bz component close to zero.

[Sandholt et al., 1998] have divided the IMF clock angles into three regimes; CAR 1, CAR 2 and CAR 3, where $0^\circ < \theta < 45^\circ$, $45^\circ < \theta < 90^\circ$ and $90^\circ < \theta < 180^\circ$. In the second panel of Figure 3.3, regime CAR 1 is indicated with blue and CAR 3 with red colours. The reason for this sorting in regimes, is that Sandholt et al. found the clock angle to order the dayside aurora quite well.

The most remarkable pattern in the IMF clock angle during January 9-12 1997 is the very long period with the clock angle in the CAR 3 regime. From 04:41 UT to 16:21 UT on January 10 the clock angle continuously stayed in CAR 3 regime. At the same time the Bz component was << 0. This combination would strongly increase the reconnection rate at the low-latitude magnetopause, and an expansion of the dayside polar cap towards lower latitudes would be expected. Afterwards followed a period of CAR 2 until 20:49 UT, which should slowly reduce the reconnection rate, so the low-altitude open-closed field line

boundary could gradually redraw polewards. From 23:31 UT on January 10 to 05:01 UT on January 11 was CAR 1, with the Bz >> 0 (except some shorter excursions to CAR 3 at ~02:58 UT and 03:05-03:09 UT). Now, the low-latitude magnetopause reconnection rate should fade and the open-closed field line boundary move severely further polewards.

3.2.3 The Time Shift Effect

When comparing solar wind data from a spacecraft far upstream from the Earth with simultaneous satellite data from the ionosphere and optical data from the ground, the time delay must be taken into account. Some estimate must be made of which amount of time the information in the solar wind needs to propagate from Wind's position and down into the polar ionosphere. With other words; when is the response seen in the ionosphere?

[Lockwood et al., 1989, and references therein] have presented a solution to this problem. Given the time lag T_{sb} between the satellite and the subsolar bow shock, the propagation time T_{bm} from the bow shock across the magnetosheath to the subsolar magnetopause, the communication time T_{mi} between the magnetopause and the cleft ionosphere and the final ionospheric propagation delay T_{is} to the station where the groundbased observations are done, the total time delay T_{tot} is found:

$$T_{tot} = T_{sb} + T_{bm} + T_{mi} + T_{is} \qquad (3.2)$$

A simplified version of Equation 3.2 is given by [Lockwood et al., 1989]:

$$T_{tot} = \frac{1}{V_{SW}}\left[X_s - 1.3X_m - \left(Y_s \cdot \frac{B_X}{B_Y}\right) + 2.6X_m\right] + T_{is} + 120 \quad (s) \qquad (3.3)$$

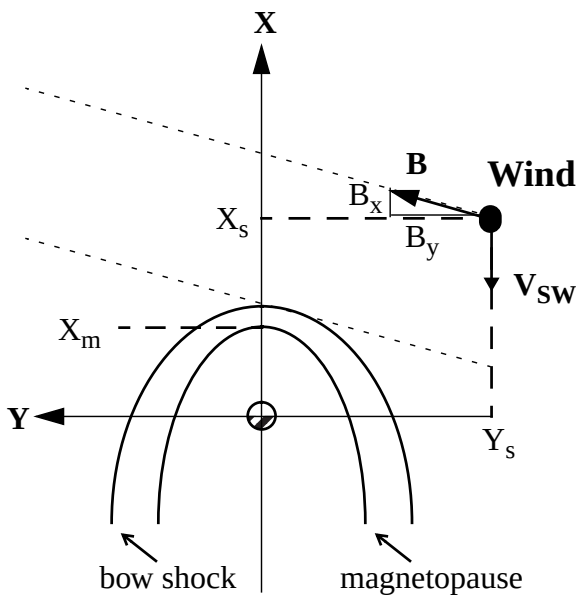

FIGURE 3.4 Sketch of the geometry used in the calculations of the time delays. Note: The figure is not to scale.

Here X_s and Y_s are the X and Y GSE coordinates of the spacecraft and X_m is the X coordinate of the subsolar magnetopause. B_X and B_Y are the IMF components from the spacecraft, and V_{SW} is the solar wind velocity (km/s), see Figure 3.4. To a good approximation the location of the magnetopause X_m is given by [Rodger, 1998]:

$$X_m = 107.4(N_{SW} \cdot V_{SW}{}^2)^{-1/6} \qquad (3.4)$$

where N_{SW} is the density (cm^{-3}) of the solar wind plasma. Collecting terms gives:

$$T_{tot} = \frac{R_e}{V_{SW}}\left[X_s + 139.6(N_{SW} \cdot V_{SW}{}^2)^{-1/6} - \left(Y_s \cdot \frac{B_X}{B_Y}\right)\right] + T_{is} + 120 \quad (s) \qquad (3.5)$$

3.2.4 Calculating the Time Delay

If the solar wind parameters from Wind January 9-12 1997 are run through Equation 3.5 Figure 3.5 is obtained. In the calculations T_{is} is set equal to 0, since it is unknown. Therefore, when comparing with observations from a groundbased station at some MLT the extra time delay T_{is} must also be added.

What is causing the very strong fluctuations in Figure 3.5? To find the answer, each of the first three terms in Figure 3.5 is examined in Figure 3.6, Figure 3.7 and Figure 3.8. It is clearly seen that the third term is responsible for the spikes. This is explained if $|B_x/B_y| \geq 1$, giving excursions to extreme values in the plus or minus directions, depending on the signs of *By* and *Bx*. Thus, the time lags in Figure 3.5 found by the method of [Lockwood et al., 1989] is probably most reliable only when $|B_x/B_y| \ll 1$.

This may be illustrated by the following example. If $|Bx| = |By|$ the third term in Equation 3.5 reduces to *-Ys* where *Ys* is -61 to -53 Re. Combined with a *Xs* of 75 to 108 Re the difference *Xs - Ys* is found to be about 135 to 160 Re, a significant increase of the time delay! If instead *Bx = -By* the same difference is found to be about 15 to 55 Re, a significant reduction of the time delay! Assuming a solar wind velocity of 450 km/s (an average of the period), this gives approximately T_{tot} = 35 to 40 min. and T_{tot} = 7 to 15 min., respectively.

This clearly demonstrates how difficult it is to calculate the exact time shift when $|X| \approx |Y|$ and the *X* and *Y* components are large; especially when $|B_x/B_y| \geq 1$ and the *Bx* or *By* components are of changing signs. Therefore, a simplified procedure must be used. Assuming the Wind spacecraft to be far upstream so that $X_S > |Y_S|$ the third term in Equation 3.5 can be omitted, giving:

$$T_{tot} = \frac{R_e}{V_{SW}}[X_s + 139.6(N_{SW} \cdot V_{SW}^{\ 2})^{-1/6}] + T_{is} + 120 \quad (s) \tag{3.6}$$

This solution is the same as assuming the problem is one dimensional (only in the X-direction), ignoring the effects of the IMF also pointing along the Y-axis. From January 9 to 12 Wind moved from $\{X_{GSE} = 75, Y_{GSE} = -61, Z_{GSE} = -2\}$ to {108, -53, -6}, and during the whole period *Xs* always stayed larger than the *Ys* coordinate!

Using Equation 3.6 instead of Equation 3.5 and again setting T_{is} equal to zero gives Figure 3.9. Figure 3.9 shows how the time shift according to Equation 3.6 varies between 22 and 30 min. January 9 to 12. The variation is mainly caused by the Wind spacecraft moving further upstream while the solar wind velocity is changing, except around the end of January 10 and the beginning of January 11 when the solar wind density reaches an extreme maximum, giving an extra rise in the time shift.

Comparing Figure 3.5 and Figure 3.9 reveals that the removal of the *Ys* dependent term introduces an extra error of maximum 10-15 min., best seen at 06-24 UT on January 10. Figure 3.5 reveals a 35-40 min. time shift, while Figure 3.9 display a 25-29 min. time shift. This is the only time when the time delay from Equation 3.5 is well-defined for a longer period, so perhaps Figure 3.5 should be used instead in this interval. However, during the rest of the period only Equation 3.6 and Figure 3.9 can be applied, so in the following discussion we therefore choose Equation 3.6 and Figure 3.9 to represent the whole period studied.

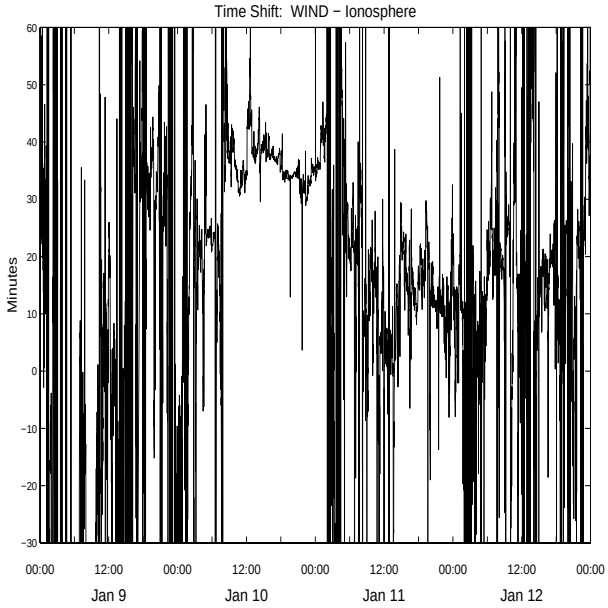

FIGURE 3.5 Calculated time delay from Wind to the noon cleft ionosphere vs. the Universal Time when the IMF was monitored at the Wind spacecraft, using Equation 3.5.

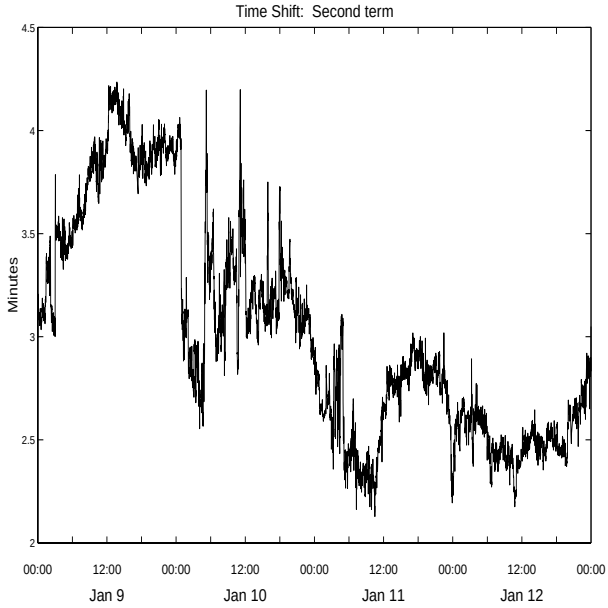

FIGURE 3.7 The time shift from the second term in Equation 3.5 vs. UT at Wind.

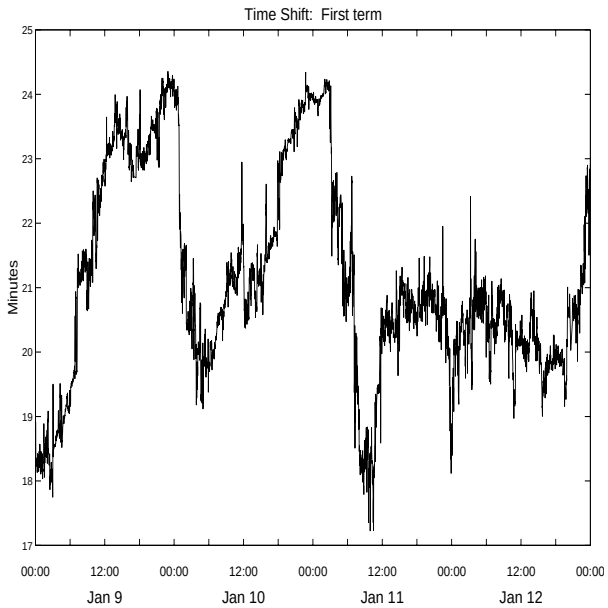

FIGURE 3.6 The time shift from the first term in Equation 3.5 vs. UT at Wind.

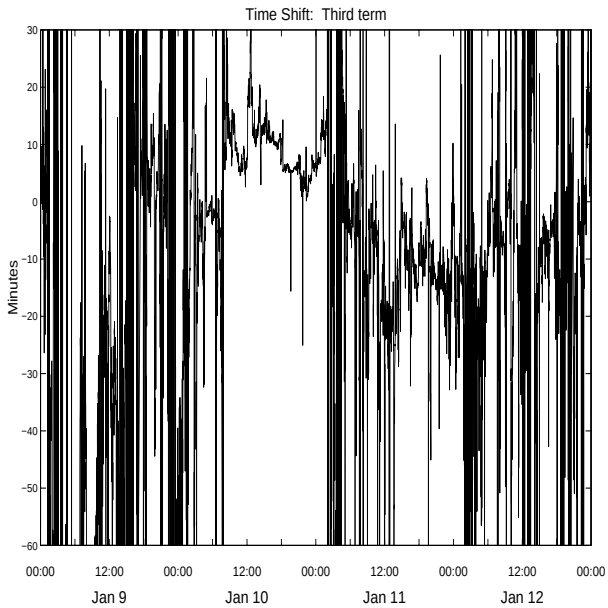

FIGURE 3.8 The time shift from the third term in Equation 3.5 vs. UT at Wind.

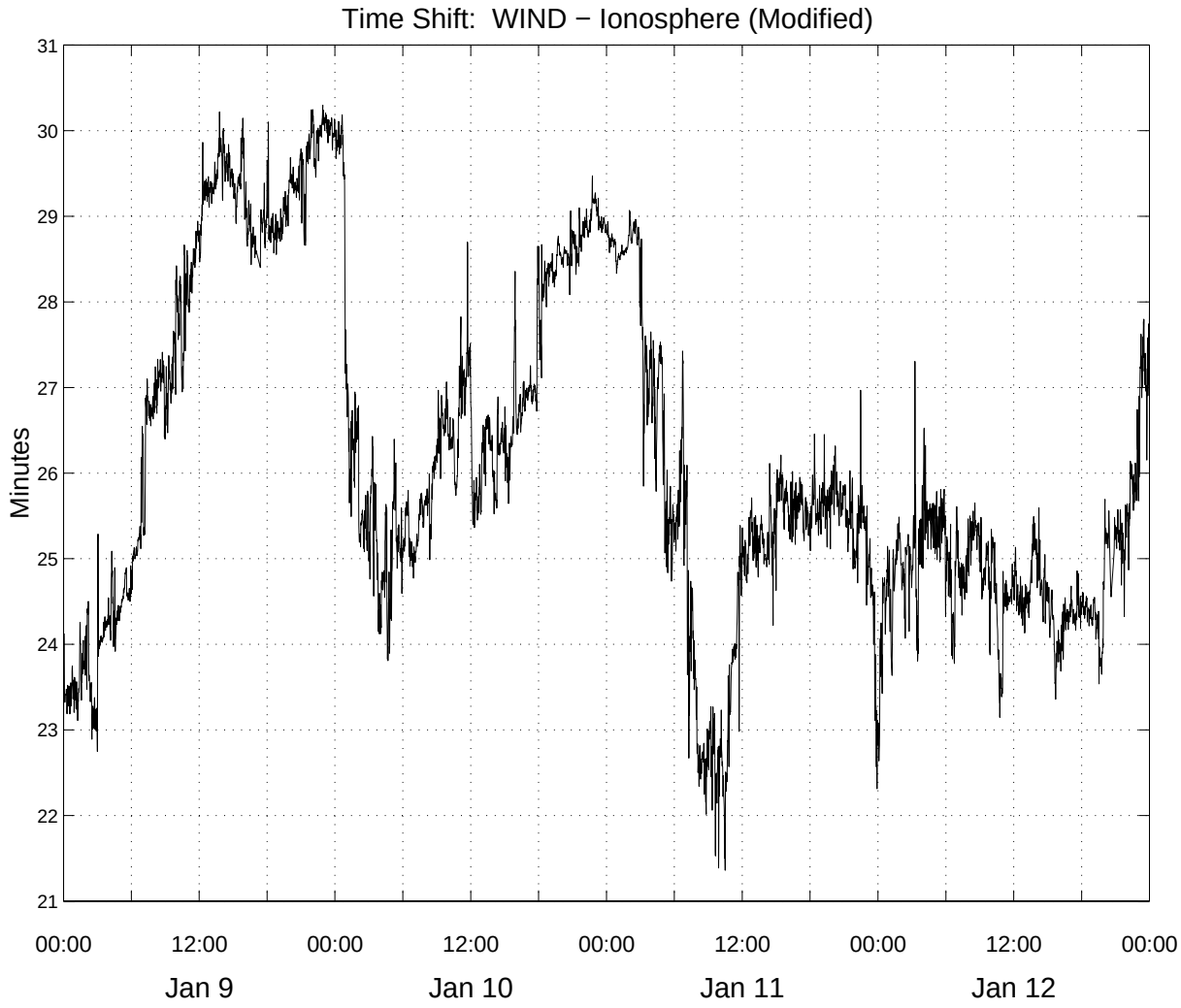

FIGURE 3.9 Calculated time shift from the Wind spacecraft to the noon cleft ionosphere January 9 to 12 1997, using the modified Equation 3.6.

This decision is, however, not critical for the conclusions to be drawn in the next sections in this chapter, since the period of the NOAA-12 orbit is 101 min. But, when comparing observations of optical events from the ground, corresponding low-altitude satellite passes and solar wind parameters from Wind, a 10-15 min. period is significant and may cause misleading conclusions. However, on January 12, the day to be studied in detail in Chapter 5, the time shifts in Figure 3.9 of 25 min. are consistent with the observed one of ~ 28 min. at 09:00-10:00 UT January 12 of [Sandholt et al., 1997]. Thus, based on Figure 3.9 and the results of Sandholt et al. a ~ 25 min. time delay on January 12 at 06:00-18:00 UT is assumed, and the rest of the period studied is also supposed to be described by Figure 3.9.

The ionospheric propagation delay T_{is} (from the noon cleft ionosphere to the station/NOAA-12) must also be added. Some estimates have been made. [Saunders et al., 1992]

found ionospheric delays T_{is} of ~5 min. 8-12 MLT and longer delays of ~10-15 min. in the regions 1-2 hours MLT outside this interval. The analysis was based on simultaneous observations using the CANOPUS magnetometer network in the 7 to 13 MLT sector during a 6-hour period of IMP 8 IMF Bz oscillations.

3.3 Summary Plots: NOAA-12 Observations

By looking at particle data from the low altitude NOAA-12 satellite, we would now like to focus on the days around this CME-event. The NOAA-12 satellite spends approximately 100 minutes on one orbit, in about 800 km altitude. The NOAA-12 satellite is also orbiting in the

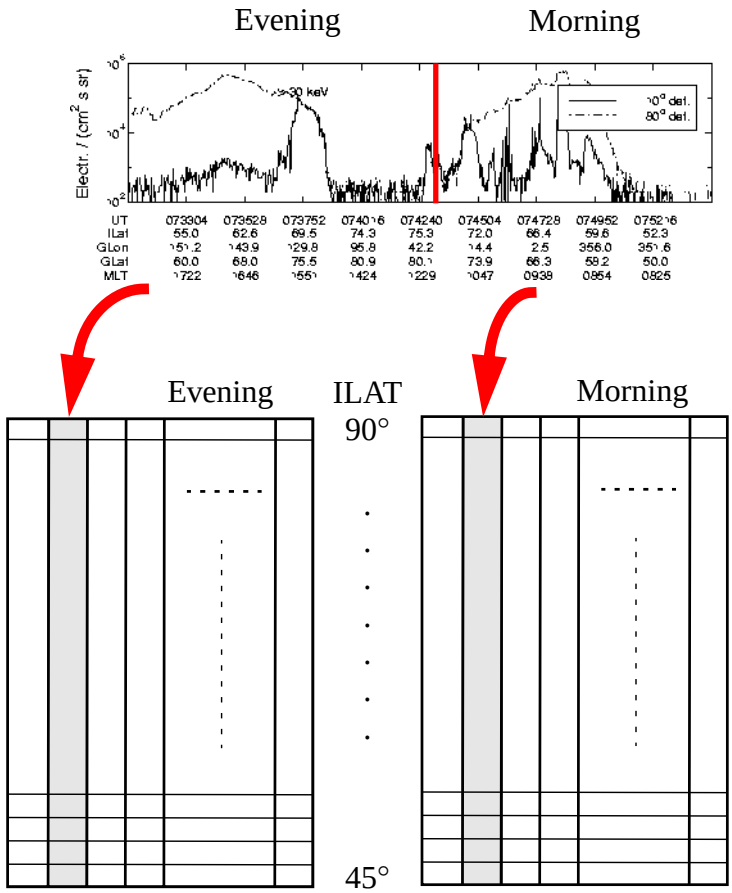

FIGURE 3.10 The sorting of NOAA satellite passes into sectors. First, each pass is divided into a morning and evening part, using the MLT. Then, each part is processed into boxes in a column from 45° to 90° ILAT. Each box is 0.25 or 1.0° ILAT wide in latitude and contains the average MEPED or TED flux detected within that invariant latitude interval, respectively.

dusk-dawn plane[‡]. Therefore, this satellite is well suited for studies of the variation in the particle fluxes in the magnetic morning and evening sectors.

Having the huge amount of particle data in mind (several MB of data), it is clear that some compact presentation technique is needed. A convenient way of summarizing this huge data

set, which has also been applied at ESRO IA, [Hauge and Søraas, 1975; Lundblad et al., 1979], and NOAA-6, [Søraas et al., 1998], particle data, is as follows:

1. All NOAA-12 passes from January 9-12, 1997 over both hemispheres are taken into account.
2. Based on magnetic coordinates (magnetic local time and invariant latitude) four regions are defined; morning sector north, morning sector south, evening sector north and evening sector south. (E.g. for the morning sector north: magnetic local time is from 00 to 12 MLT and the invariant latitude is positive from 45 to 90° invariant latitude).
3. All passes are then processed, and the fluxes are assigned to boxes within one of the regions, see Figure 3.10. (Because of NOAA-12's orbit plane, each region is visited only once every orbit). For the MEPED detector each box is 0.25° ILAT wide in latitude, while it is 1° ILAT for TED. (This is due to the different time resolution of the two instruments).

A complete listing of all the times when NOAA-12 was entering the different sectors during January 9 to 12 1997 is given in Table 3.11. NOAA-12 spends about 10-15 minutes in each of the regions; entering the northern evening sector from the equatorward edge, the northern morning from poleward, the southern morning from equatorward and the southern evening from the poleward edge.

‡ At very high latitudes in the Northern (Southern) hemisphere the NOAA-12 satellite most often is passing the noon-midnight meridian at magnetic local times on the dayside (nightside), because of the orbit's inclination, see Figure 2.2 in Chapter 2.

3.3.1 Proton Flux at the 80˚ MEPED Detector

By using the described selection method for the 80 degrees MEPED proton detector, Figure 3.12 on page 38 is obtained. According to Section 2.1.2 on page 18, in the Auroral Zone, this detector measures trapped protons, because the axis of detection points almost perpendicular to the local magnetic field direction.

The first thing one notices is the rather large rise in the fluxes of protons trapped in the Earth's magnetic field January 10. The increase is most intense and spans over the widest range (from ~60 to ~75 degrees) in invariant latitude in the southern evening sector. However, a similar intensification is also seen in the other sectors, although in a smaller scale. The increment is best seen in the two lowest energy channels (30-80 keV and 80-250 keV). During January 11-12, the fluxes decrease a bit, even though they still are larger than for the 9th.

From Table 3.11 on page 35 it is possible to more precisely decide when the huge increase took place. In the southern evening and morning sectors the very sharp enlargement, especially in the 30-80 keV channel, is first seen (in pass 19) at 07:23 UT on January 10. However, in the northern sectors an increase is observed already in (pass 18) at 04:50-05:03 UT in the evening side and 05:03-05:15 UT in the morning side. This activity starts to move equatorward in the northern evening sector during the next pass, before a maximum intensity and a clear motion of both the poleward and equatorward boundaries of trapped 30-80 keV protons towards lower latitudes occur (in pass 20) at ~08:14 UT. The region stays shifted equatorward until somewhere between 16:50 and 18:20 UT, when the region again starts to

	Northern hemisphere		Southern hemisphere	
	Dusk	Dawn	Dawn	Dusk
January 9	0004	0018	0055	0108
	0147	0200	0237	0251
	0329	0342	0418	0435
	0512	0525	0601	0619
	0655	0708	0745	0801
	0836	0850	0928	0943
	1017	1032	1110	1124
	1158	1213	1250	1304
	1339	1354	1430	1444
	1520	1534	1610	1623
	1701	1714	1750	1803
	1842	1855	1930	1943
	2021	2035	2110	2123
	2201	2215	2251	2304
	2342	2356	0033	0046
January 10	0124	0138	0214	0229
	0307	0320	0356	0412
	0450	0503	0538	0556
	0632	0645	0723	0739
	0814	0828	0906	0921
	0955	1009	1048	1102
	1136	1151	1228	1242
	1317	1331	1408	1422
	1458	1512	1548	1601
	1639	1652	1728	1741
	1820	1833	1908	1921
	2000	2013	2048	2101
	2139	2153	2229	2242
	2319	2334	0010	0023

	Northern hemisphere		Southern hemisphere	
	Dusk	Dawn	Dawn	Dusk
January 11	0102	0116	0152	0206
	0244	0258	0334	0350
	0427	0440	0516	0533
	0610	0623	0700	0717
	0752	0805	0844	0859
	0933	0947	1025	1040
	1114	1128	1206	1220
	1255	1309	1346	1400
	1436	1450	1526	1540
	1617	1630	1706	1719
	1758	1811	1846	1859
	1938	1951	2026	2039
	2117	2131	2207	2220
	2257	2312	2348	0001
January 12	0039	0053	0130	0144
	0222	0235	0312	0327
	0405	0418	0453	0511
	0547	0600	0637	0654
	0730	0743	0821	0836
	0911	0925	1003	1018
	1052	1106	1144	1158
	1233	1247	1324	1338
	1414	1428	1504	1518
	1555	1608	1644	1657
	1736	1749	1824	1837
	1916	1929	2004	2017
	2055	2109	2145	2157
	2235	2250		

FIGURE 3.11 Overview of the times of entry for all the NOAA-12 passes January 9 to 12 1997, see text. To decide the correct time of each single pass in Universal Time the table should be compared with the following figures: Figure 3.12, Figure 3.13, Figure 3.14, Figure 3.15, Figure 3.17, Figure 3.18, Figure 3.19, Figure 3.20, Figure 3.21 and Figure 3.22.

propagate polewards. This is also approximately the same time as the fluxes in the southern evening sector start to decrease.

In the beginning of January 11 an increase is seen in the morning sectors. At ~01:16 UT and ~01:52 UT (pass 30) an increment in the 30-250 keV energy range is seen in the northern and southern morning sectors, respectively. Thus, the enhancement occurred somewhere between ~00:23-00:35 (pass 29) and ~01:16 UT.

In Figure 3.12 on page 38 the Dst-index is also shown. The very good correlation between the decrease in the Dst and the increase/equatorward motion of the proton fluxes in the evening sectors is obvious. The Dst falls off very rapidly at 06-08 UT on January 10 before reaching a minimum of -84 nT 09-11 UT. Then the Dst start climbing before reaching a maximum of 49 nT at 01-02 UT on January 11.

3.3.2 Proton Flux at the 10˚ MEPED Detector

The 10 degrees detector points 10 degrees from the local vertical. By referring to Section 2.1.2 on page 18, it is seen that in or near the auroral zone, the 10 degrees detector displays the flux of precipitating particles. Therefore Figure 3.13 on page 39 shows the fluxes of precipitating protons.

The proton precipitation clearly shows a huge increase at the same times as for the trapped protons on January 10. More or less the same description may be used here, but the latitudinal extent of the precipitation is much more narrow, especially in the morning sectors. Here, the two lowest energy channels also show the most clear increase in the flux.

Using the same procedure as in Section 3.3.1 the same times are found for the enhancements on January 10, suggesting an intensification of the both the precipitating trapped proton fluxes took place somewhere between 06:10 and 07:23 UT in the southern hemisphere and gradually from ~04:50 UT (reaching maximum displacement and intensity from ~08:14 UT) and onwards in the northern hemisphere. Therefore, some process must have been operating and injecting energetic protons around this time.

The increase in the two morning sectors in the beginning of January 11 is not this easily seen in Figure 3.13. In the southern morning sector no clear rise is found. However, in the northern morning sector an enlargement is observed at ~01:16 UT.

3.3.3 Electron Flux at the 80˚ MEPED Detector

For the trapped electrons, an increase in the fluxes on January 10 is also observed, Figure 3.14 on page 40. However, the main difference from the protons is that the intensification is strongest in the morning sectors. At ~07:23 UT the southern morning sector shows a sharp rise in the trapped electron fluxes. No clear increase is detected before this time in the southern hemisphere. In the northern morning sector, however, a growth in the trapped electron fluxes is observed from ~05:03 UT. Then an equatorward displacement of the northern morning and evening regions is seen ~06:32-06:55 UT. At the same time the latitudinal widths of both northern regions become very narrow.

An other feature is the clear increase observed in the >300 keV detector, seen in all the sectors. The trapped highest-energetic electron fluxes are remarkably larger (factor ~10-100) during January 10 to 12 than on the

9th. So, some injection and acceleration process must have been initiated January 10. The process must also have been working during January 11 and 12 supplying energized plasma to maintain the trapped highest energy electron fluxes.

In the northern evening sector the motion of the trapped region towards lower latitudes is also observed, just as for the protons in Section 3.3.1 and Section 3.3.2. However, the intensities are far lower than in the morning sectors.

The good correlation with the Dst-index is obvious. The increase in electron fluxes in the morning sectors is observed to correspond very well with the negative bay in the Dst on January 10. The equatorward motion of the trapped region in the northern evening sector also appears at the same time, as for the protons.

3.3.4 Electron Flux at the 10˚ MEPED Detector

For the precipitating electrons the most intense fluxes are also observed in the morning sectors on the January 10, Figure 3.15 on page 41, and the two lowest energy channels is dominating. Some discrete events are also seen the other days, but the intensities are still largest in the morning sectors of January 10.

The dramatic increment in the southern morning sector observed ~07:23 UT on January 10 is consistent with the observations of the protons and the trapped electrons. In the southern morning sector the >30 keV detector shows a weak decrease in the electron flux in the next passes after this onset.

Later, on January 12 a sharp injection is seen in the southern evening and morning sectors at ~08:21 to ~08:50 UT. [Bjordal et al., 1997] reported the abrupt onset of a negative bay at 07:28 UT with further intensifications about 07:56 UT and 08:16 UT. Bjordal et al. also displayed POLAR PIXIE X-ray images and POLAR UV images from the opposite (northern) hemisphere between 07:15 and 09:15 UT. Their images show strong X-ray activity 08:05 to 08:35 UT. Thus, the intense electron precipitation observed by NOAA-12 in the southern hemisphere is obviously resulting from the same substorm as reported by [Bjordal et al., 1997]. (Some X-ray images from this event is displayed in Figure 5.28 and discussed in Section 5.7.)

In the northern evening sector an intensification is observed at ~01:02 UT on January 11. This is also consistent with the observations in Section 3.3.2 of the precipitating proton fluxes in the morning sector and the positive peak in the Dst. For all the days a good consistency between the Dst and the maximum in the electron fluxes is found.

3.3.5 The High-Energy Particle Drifts

By looking at Figure 3.12 to Figure 3.15 one thing is very clear. The high-energy protons show larger fluxes in the evening sectors and the high-energy electrons in the morning sectors. [Meng et al., 1981] studied the spatial distribution of energetic particles in the distant magnetotail ($X_{SM} < 0$) using the IMP 7 and IMP 8 spacecrafts. Superposing about 10 years of observations onto the dawn-dusk meridian cross-section, they found a dawn-dusk asymmetry for electrons and protons in the plasma sheet. Electrons gathered to the morning side and protons to the dusk side. Their statistical pattern is in good agreement with the January 9-12 1997 observations from the NOAA-12 satellite.

This pattern is expected, since e. g. the high-energy electrons in the ring current are drifting from near midnight, where the ejection

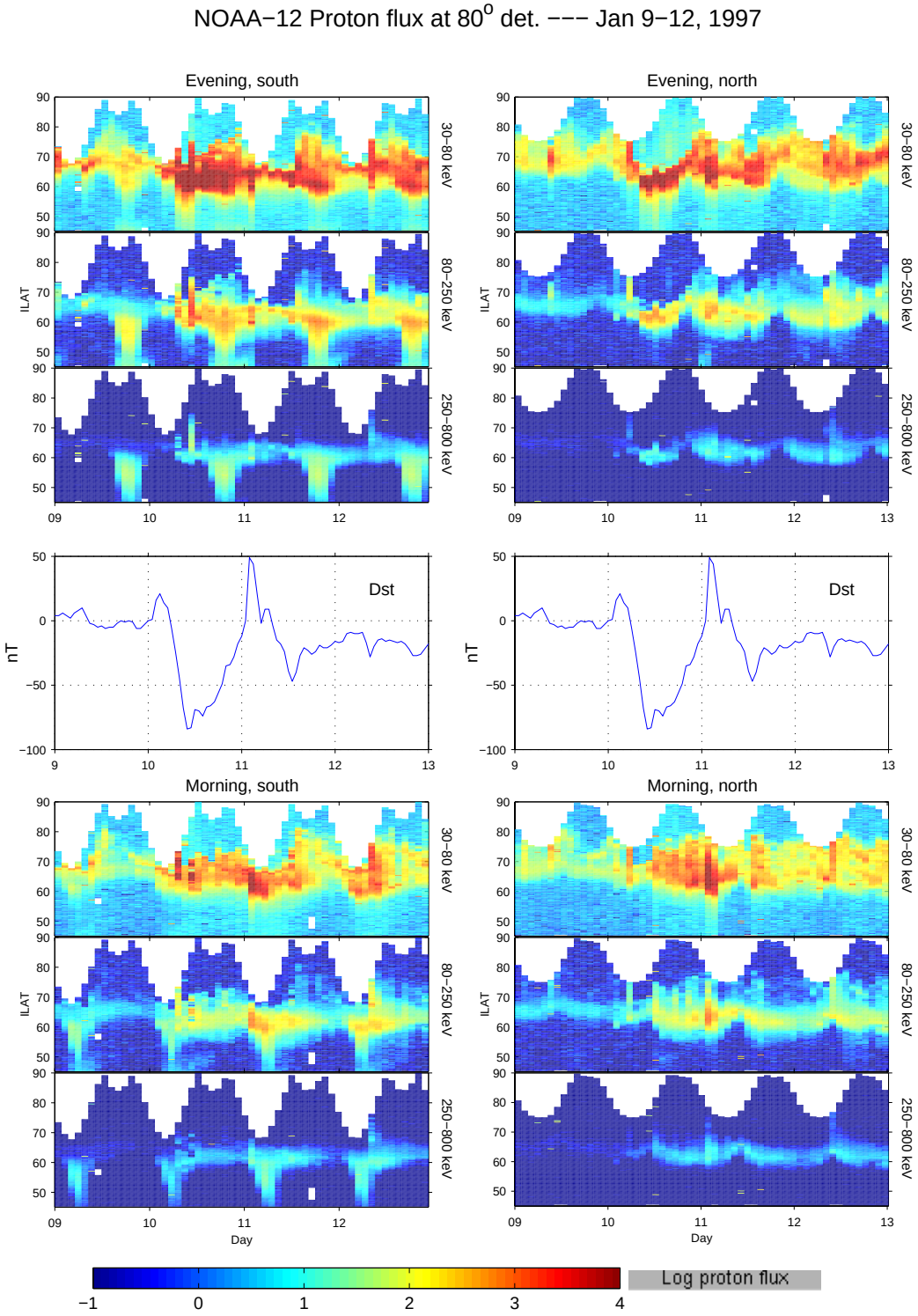

FIGURE 3.12 NOAA-12 80° MEPED Proton Fluxes from three energy channels (30-80 keV, 80-250 keV & 250-800 keV) vs. Invariant Latitude and Time, January 9-12 1997. The Magnetic Evening (Morning) Sectors are at the top (bottom). The Southern (Northern) Hemisphere is to the left (right). In the middle the Dst-index is shown.

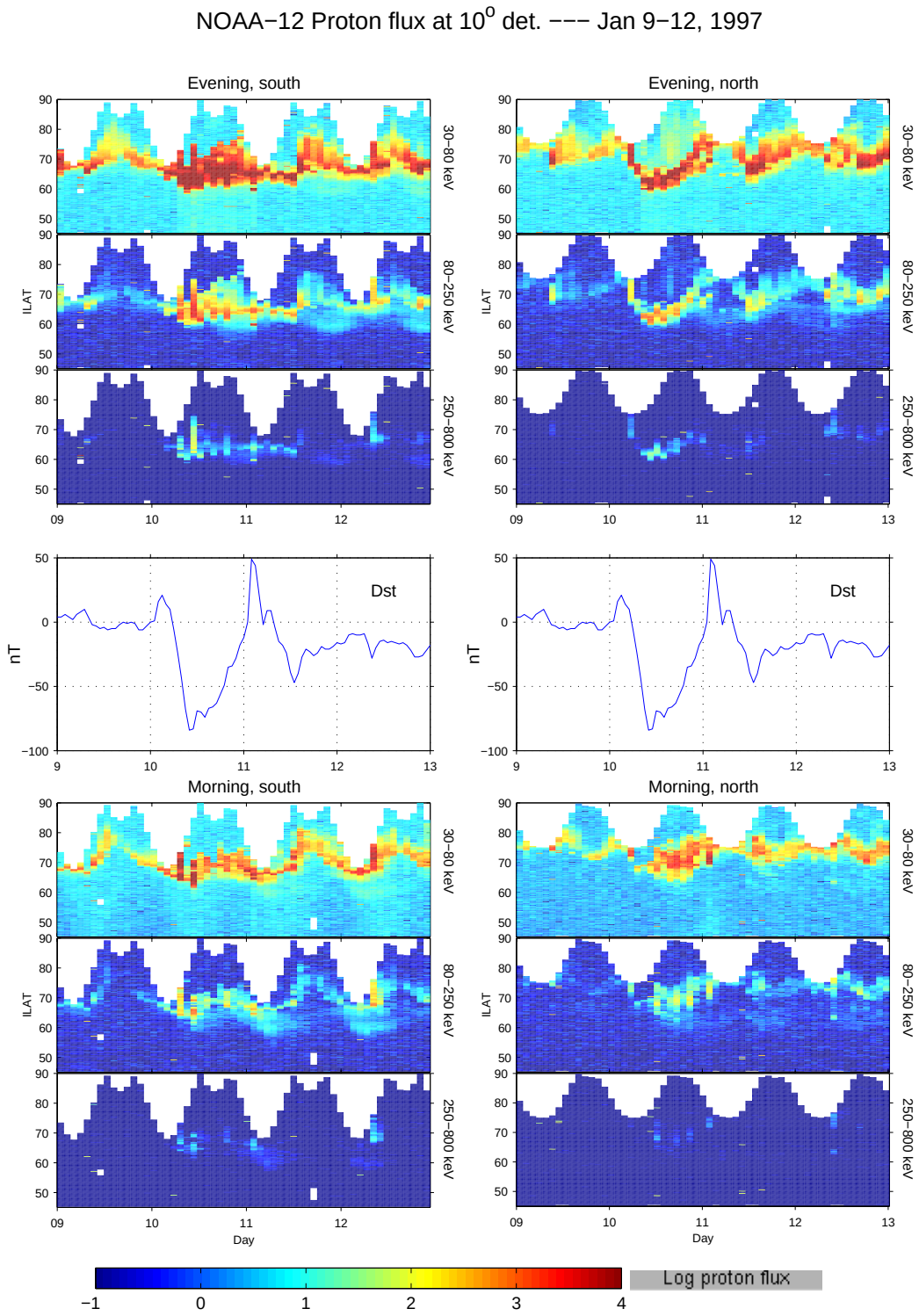

FIGURE 3.13 NOAA-12 10° MEPED Proton Fluxes from three energy channels (30-80 keV, 80-250 keV & 250-800 keV) vs. Invariant Latitude and Time, January 9-12 1997. The Magnetic Evening (Morning) Sectors are at the top (bottom). The Southern (Northern) Hemisphere is to the left (right). In the middle the Dst-index is shown.

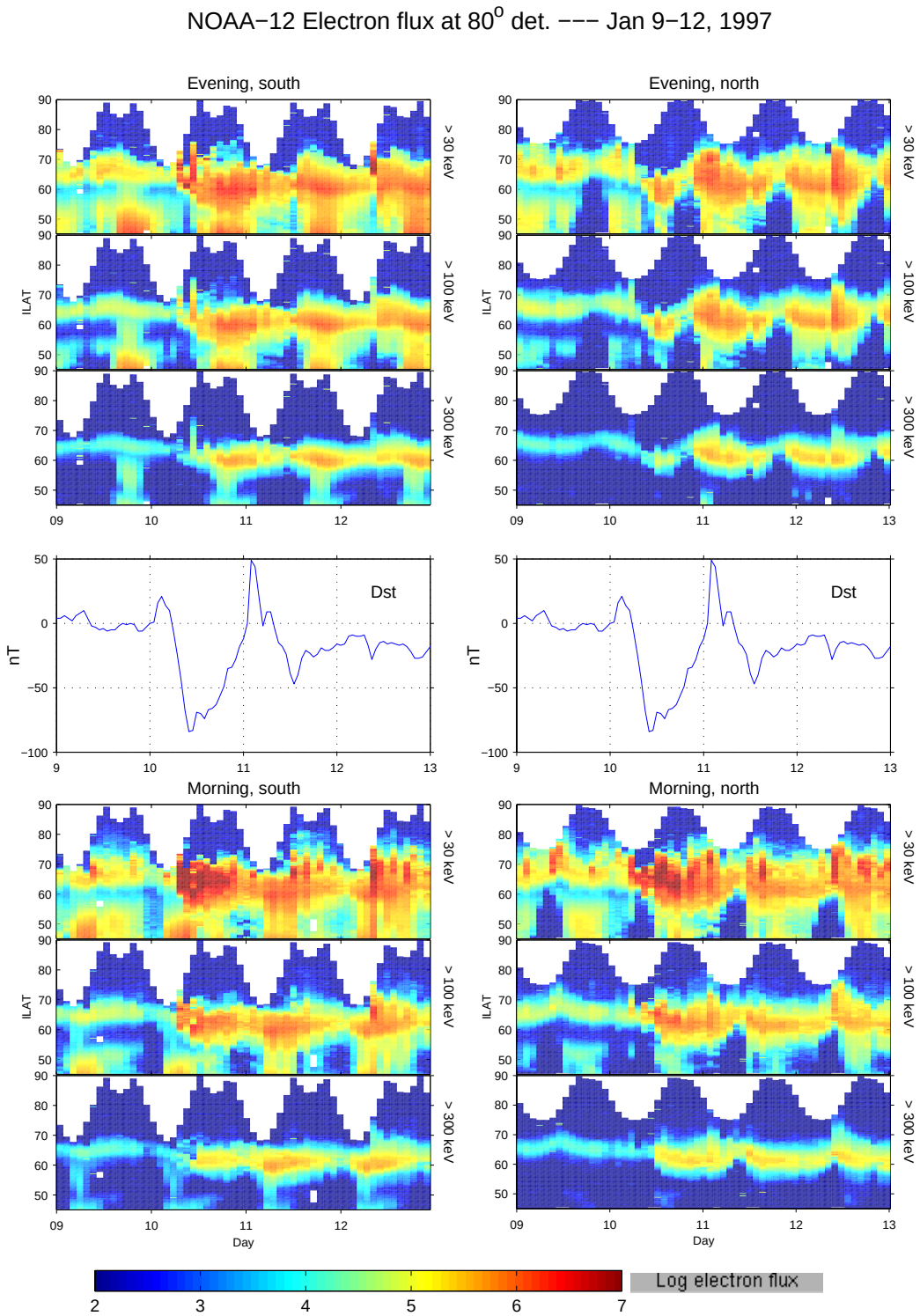

FIGURE 3.14 NOAA-12 80° MEPED Electron Fluxes from three energy channels (>30 keV, >100 keV & >300 keV) vs. Invariant Latitude and Time, January 9-12 1997. The Magnetic Evening (Morning) Sectors are at the top (bottom). The Southern (Northern) Hemisphere is to the left (right). In the middle the Dst-index is shown.

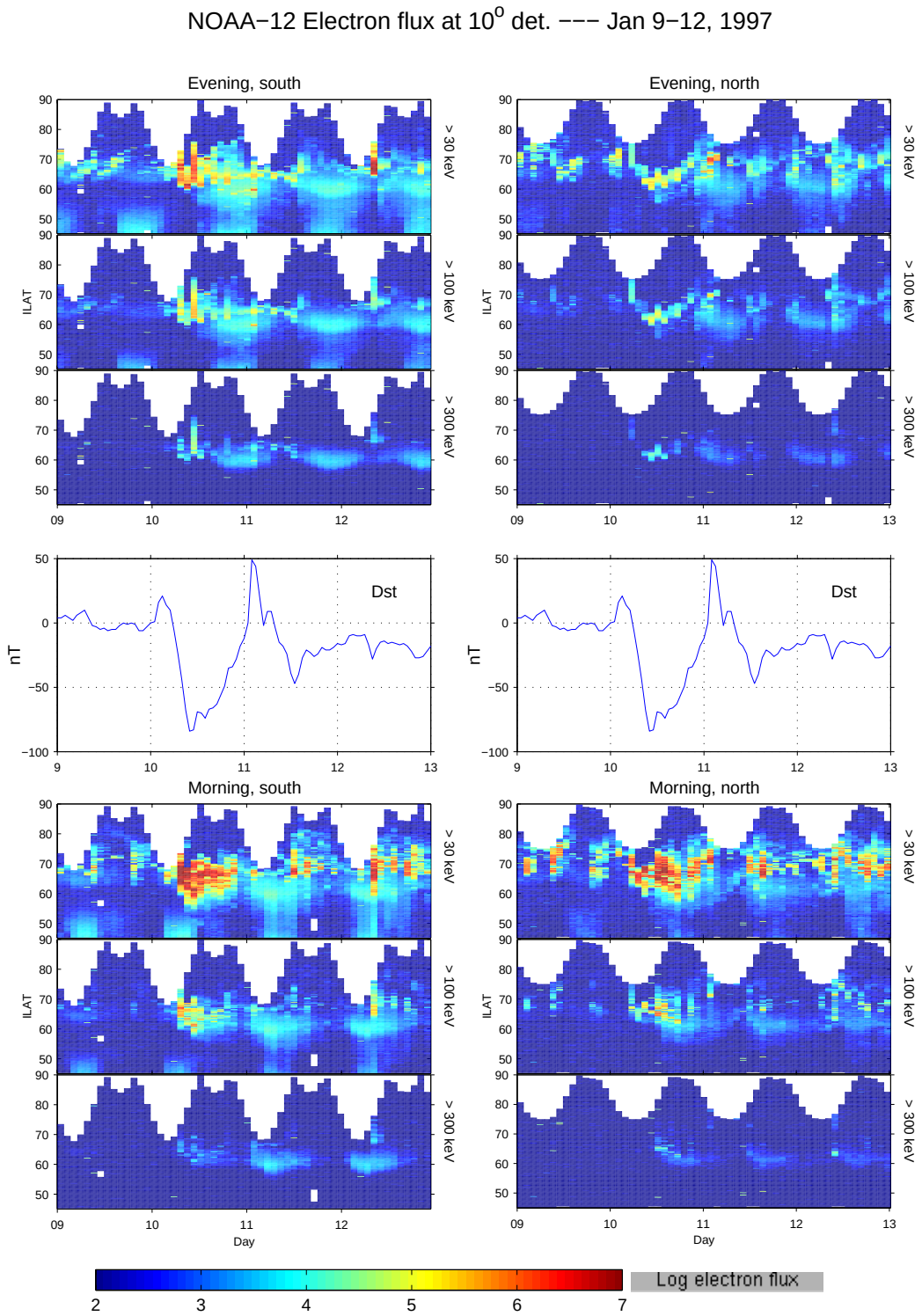

FIGURE 3.15 NOAA-12 10° MEPED Electron Fluxes from three energy channels (>30 keV, >100 keV & >300 keV) vs. Invariant Latitude and Time, January 9-12 1997. The Magnetic Evening (Morning) Sectors are at the top (bottom). The Southern (Northern) Hemisphere is to the left (right). In the middle the Dst-index is shown.

of ring current particles is expected to be, and towards the morning side where the largest fluxes of electrons should be. When the electrons have drifted almost around the Earth and passes the evening sector, it is expected that the electron fluxes should be much smaller because of no sources and significant losses in the morning and noon sectors. The high-energy protons, drifting in the other direction from midnight via the evening side past noon to the morning side, show a similar feature. This results from the charge dependence in the magnetic gradient drifts:

- The E×B-drift velocity v_{DE} given by

$$\overrightarrow{v_{DE}} = \frac{\vec{E} \times \vec{B}}{B^2} \qquad (3.7)$$

  where E and B's are the electric and magnetic fields, respectively, does not explain the effect. This E×B-drift is charge independent, causing both electrons and protons to drift in the same direction. Therefore the E×B-drift is not responsible for the observed morning/evening asymmetry in the high-energy electron and proton fluxes.

- However, the magnetic gradient and curvature drifts do. The magnetic drift velocity v_{DB} is given by:

$$\overrightarrow{v_{DB}} = \frac{K}{qB^3}(1 + \cos^2\alpha)\vec{B} \times \nabla B \qquad (3.8)$$

  where K the energy of the particle, q the charge, B the magnetic field and α the particle's pitch angle. Assuming the injection of particles to take place at midnight, the positively charged high-energy protons experience a westward drift from midnight towards the evening side. On the other hand, the negatively charged high-energy electrons are drifting eastward from midnight towards the morning side, see Figure 3.16.

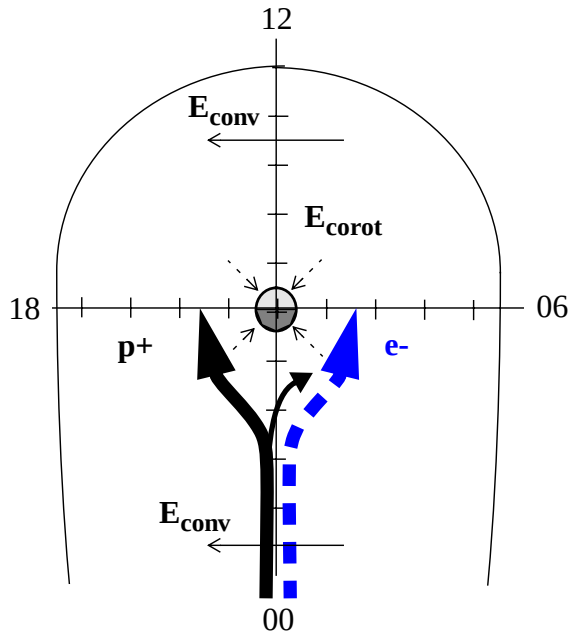

FIGURE 3.16 A sketch of the drift of energetic electrons and protons assuming an injection of particles at midnight and only the magnetic drift (thick solid and thick dashed arrows). The corotation electric field $\boldsymbol{E_{corot}}$ and a uniform convection electric field $\boldsymbol{E_{conv}}$ are indicated. (A drift of low-energy protons towards the morning sector has also been included for reference. This drift will be discussed when the low-energy TED data is presented in Section 3.6.2.)

During the drift period around the earth, trapped protons and electrons are continuously lost. Important loss processes may be wave generation causing scattering of particles into the atmospheric loss cone (e.g. electron precipitation on the morning side due to wave-particle interaction), particles passing through the magnetopause (quasi-trapped) and violation of the adiabatic invariants. The sunlit ionosphere also changes the background plasma. Thus, passing noon and reaching the opposite dusk/dawn side of Earth, the trapped and precipitating high-energy electron and

proton fluxes have become smaller. Further details on magnetospheric drifts, is given by e.g. [Roederer, 1970; Fälthammar, 1973; Lyons and Williams, 1984].

3.3.6 The Time of Year Effect

In most of the panels presented the southern sectors show the largest fluxes. This may be due to a 'time of year' effect. In January it is winter in the northern hemisphere and summer in the southern. The Earth's axis of rotation is pointing more towards the Sun in the south than north. Therefore, in average the Earth's dipole axis also is pointing more towards the Sun in south, giving a matching tilt of the magnetosphere and the best direct coupling between the solar wind and the ionosphere in the southern hemisphere. In this way, any direct entry of solar wind plasma should perhaps be best seen in the southern hemisphere.

This proposal is in good agreement with our observations, although we have only studied one time of the year here, January 9-12 1997. A further future study, also including observations from other times of the year, is needed to test whether such a relationship is always present.

3.4 The Ratio: Precipitating to Trapped Flux

In order to better see the differences between the trapped and the precipitating fluxes, the ratio precipitating to trapped flux f_{ratio} can be plotted:

$$f_{ratio} = \frac{f_{10}}{f_{80}} \quad \textbf{(3.9)}$$

where f_{10} is the precipitating flux, and f_{80} the trapped flux. Since some of the data points may be zero, zero-containing elements must be excluded before doing the division**.

3.4.1 The MEPED Proton Flux Ratio

By running the proton flux data through Equation 3.9 as described above, Figure 3.17 on page 44 is encountered. Here the red colours indicate that the precipitating flux is dominating, while the blue ones show where the trapped flux is dominating (anisotropic zone). The yellow colours imply that the fluxes are of equal size and isotropic.

Just as for the 10 and 80 degrees fluxes (Figure 3.13 and Figure 3.12), the flux ratio plot in Figure 3.17 more or less shows the same pattern. The interesting and very clear move in the northern evening sector of the boundaries towards lower latitudes on January 10 is clearly seen. However, the largest advantage by plotting the ratio in this way, is that the isotropic boundaries and the anisotropic zone are more clearly obtained.

Of interest is also the very strong anisotropy seen in the 30-250 keV energy range from ~60° to ~70° ILAT in the northern evening and morning sectors and the southern morning sector in the beginning of January 11. This anisotropy corresponds with the event described in Section 3.3.1 to Section 3.3.4.

3.4.2 The MEPED Electron Flux Ratio

Using the same procedure on the electron flux data gives Figure 3.18 on page 45. Here the anisotropic zone is very much wider. In the highest energy channel (>300 keV) a sharp increase in the latitudinal width of the anisotropic (blue) region is observed from the end of January 10 or beginning of January 11. This pattern persist the rest of the period. In the northern evening sector this expansion is

** In fact, the zeros both in the numerator and the denominator makes trouble since the plotting routine makes use of the logarithmic function, which is undefined for an argument equal to zero.

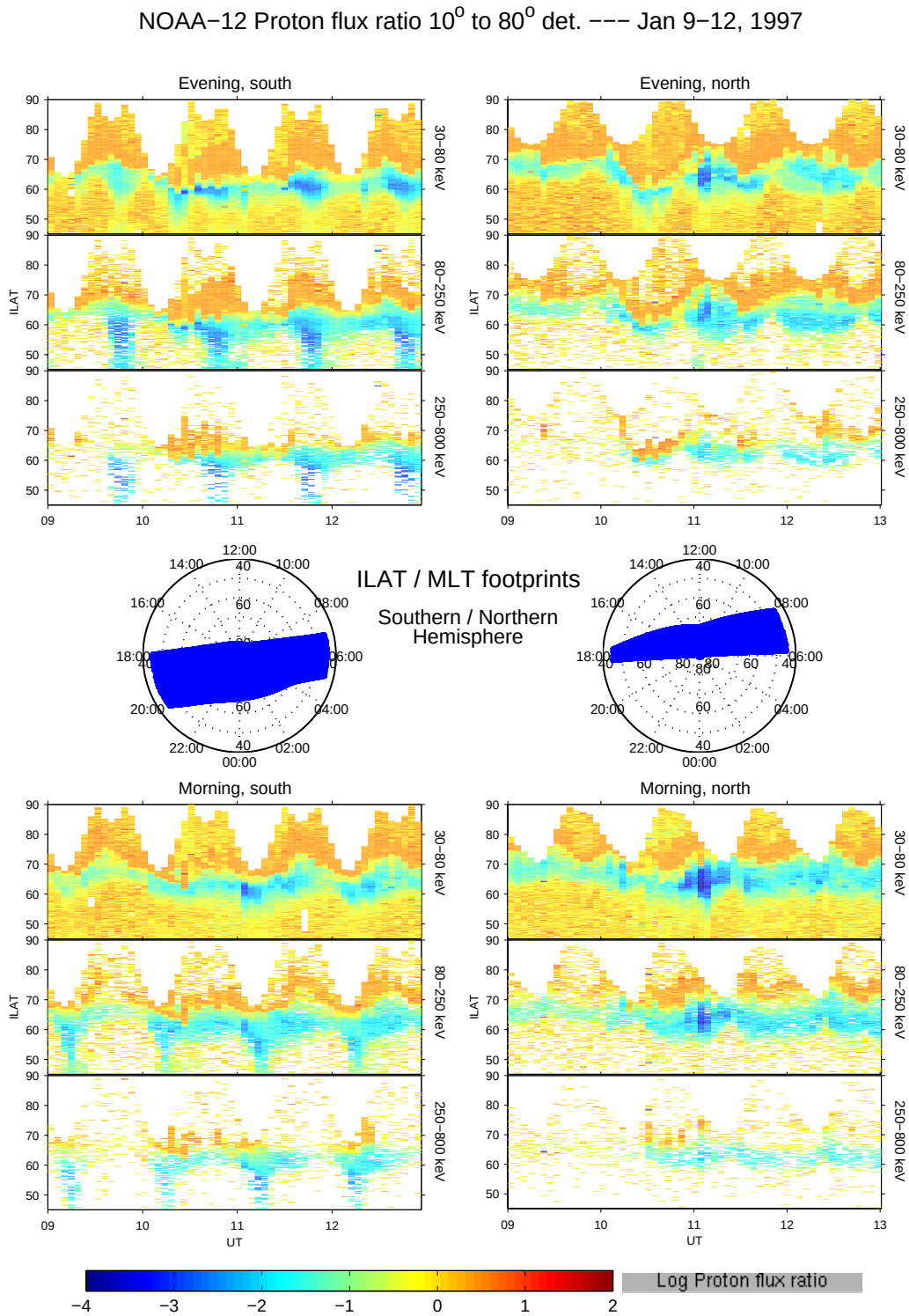

FIGURE 3.17 NOAA-12 MEPED Proton Flux Ratio for three energy channels (30-80 keV, 80-250 keV & 250-800 keV) vs. Invariant Latitude and Time January 9-12, 1997. Red colours where the precipitating flux is dominating, blue where the flux is trapped and yellow colour for the isotropic flux.

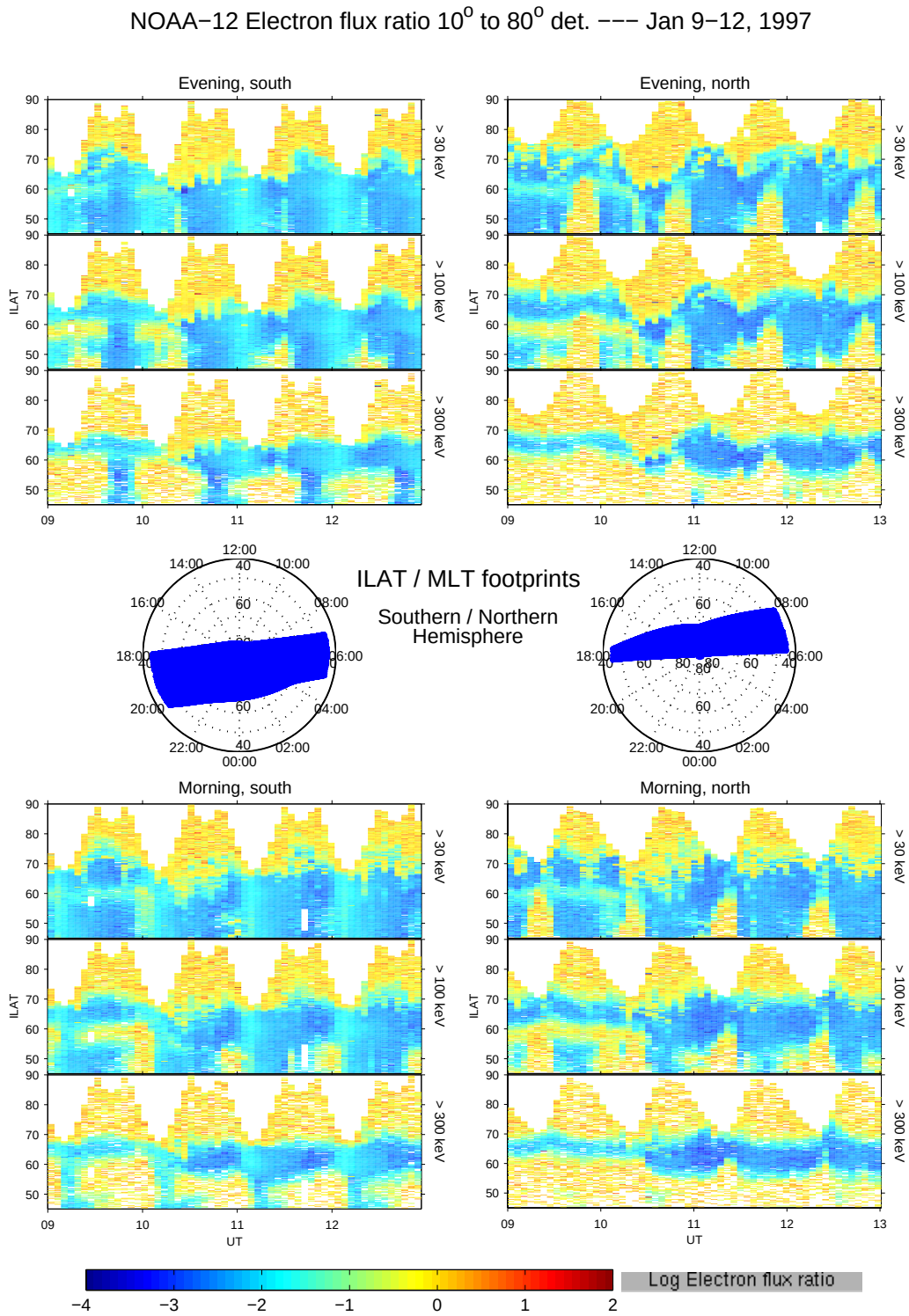

FIGURE 3.18 NOAA-12 MEPED Electron Flux Ratio for three energy channels (>30 keV, >100 keV & >300 keV) vs. Invariant Latitude and Time January 9-12, 1997. Red colours where the precipitating flux is dominating, blue where the flux is trapped and yellow colour for the isotropic flux.

observed from ~21:39 UT January 10 and onwards. In the northern morning sector, however, this enlargement was seen already at ~11:51 UT. In the southern morning sector the increment is discovered from ~12:28 UT.

The equatorward motion of the trapping boundary in the northern evening sector (discussed in Section 3.3.1 to Section 3.3.4) i also seen in the electron flux ratio in Figure 3.18 on January 10. The displacement of course both starts and ends at the same times as in Figure 3.14 and Figure 3.15.

3.5 The Difference: Precipitating Minus Trapped Flux

Looking through the whole NOAA-12 MEPED data set for January 9-12, 1997, one tendency is clear. In the intervals where Figure 3.17 shows isotropic proton fluxes, all the single passes indicates that the 10 degree fluxes are slightly larger than the 80 degree fluxes. For the electrons though, this is not seen. One way to illustrate this feature is by taking the difference f_{diff}

$$f_{diff} = f_{10} - f_{80} \tag{3.10}$$

where f_{10} is the precipitating flux and f_{80} is the trapped flux. But, when the logarithm of f_{diff} is to be taken, one has to redefine[††] the logarithmic function

$$\log_{redefined}(x) = \begin{cases} -\log_{10}(x) & \text{for} \quad x < -1 \\ 0 & \text{for} \quad -1 \le x \le 1 \\ \log_{10}(x) & \text{for} \quad x > 1 \end{cases} \tag{3.11}$$

since the logarithmic function is not defined for negative arguments.

3.5.1 The Proton Flux Difference

When the described method is used, Figure 3.19 on page 47 is obtained. The red areas indicate that the precipitating 10 degree fluxes are larger than the trapped 80 degree fluxes by the difference given. The blue areas shows the opposite case where the trapped flux is largest. The green areas show where the fluxes are of equal size.

The first thing one notices in Figure 3.19, is the very clear interval, poleward of the anisotropic zone (in Figure 3.17), where the precipitating fluxes seem to be larger than the trapped ones (red areas on the figure). This occurs for the invariant latitudes corresponding to the isotropic zone in Figure 3.17. However, this effect is most likely artificial, as notified by [Dave Evans, personal communication]. Due to radiation damage the effective dead-layer on the 80 detector increases vs. time, thus blocking off the lower energy protons and reducing the flux detected.

3.5.2 The Electron Flux Difference

The same effect is though not seen by the MEPED electron detectors, since the electrons is not so much effected by the dead-layer. Figure 3.20 on page 48 does not show any sign of a wider region where the electron precipitation dominates. Only smaller discrete areas are seen, and those are mainly on the equatorward side of the isotropic region.

In the isotropic zone another feature is seen, the continuous flipping pattern from precipitating dominating, via identical to trapped dominating fluxes. This indicates that the electron precipitation is much more discrete and strongly localized than the proton precipitation.

[††] The way the logarithmic function $log_{redefined}$ is defined for -1≤x≤1 in Equation 3.11, is equal to saying the 10° and 80° fluxes are identical whenever the absolute flux difference $|f_{diff}|$ is less than 1 particle/(cm^2 s ster keV).

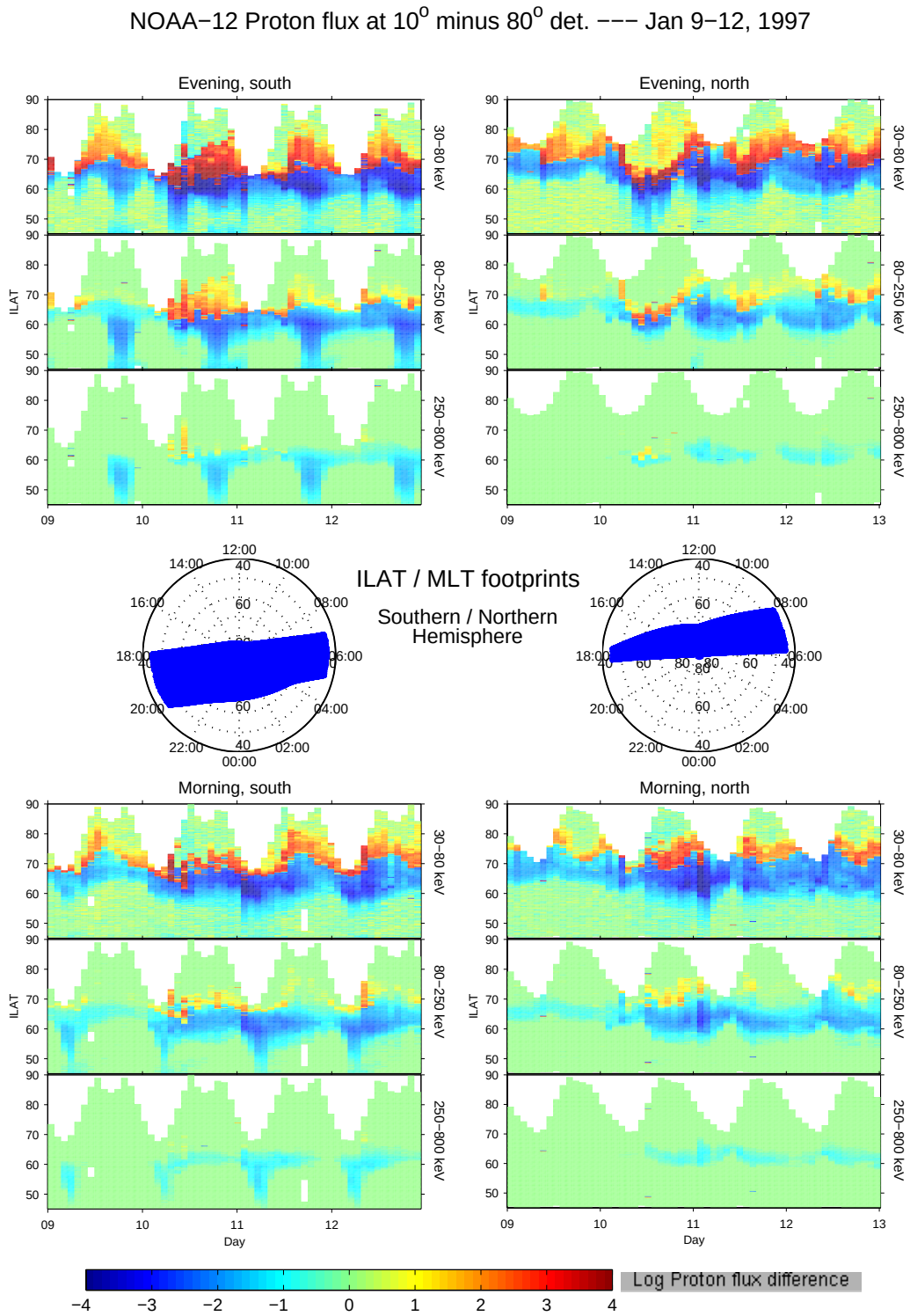

FIGURE 3.19 NOAA-12 MEPED Proton Flux Difference for three energy channels (30-80 keV, 80-250 keV & 250-800 keV) vs. Invariant Latitude and Time January 9-12, 1997. Red colours where the precipitating flux is larger, blue where the trapped flux is larger and green where the fluxes are equal.

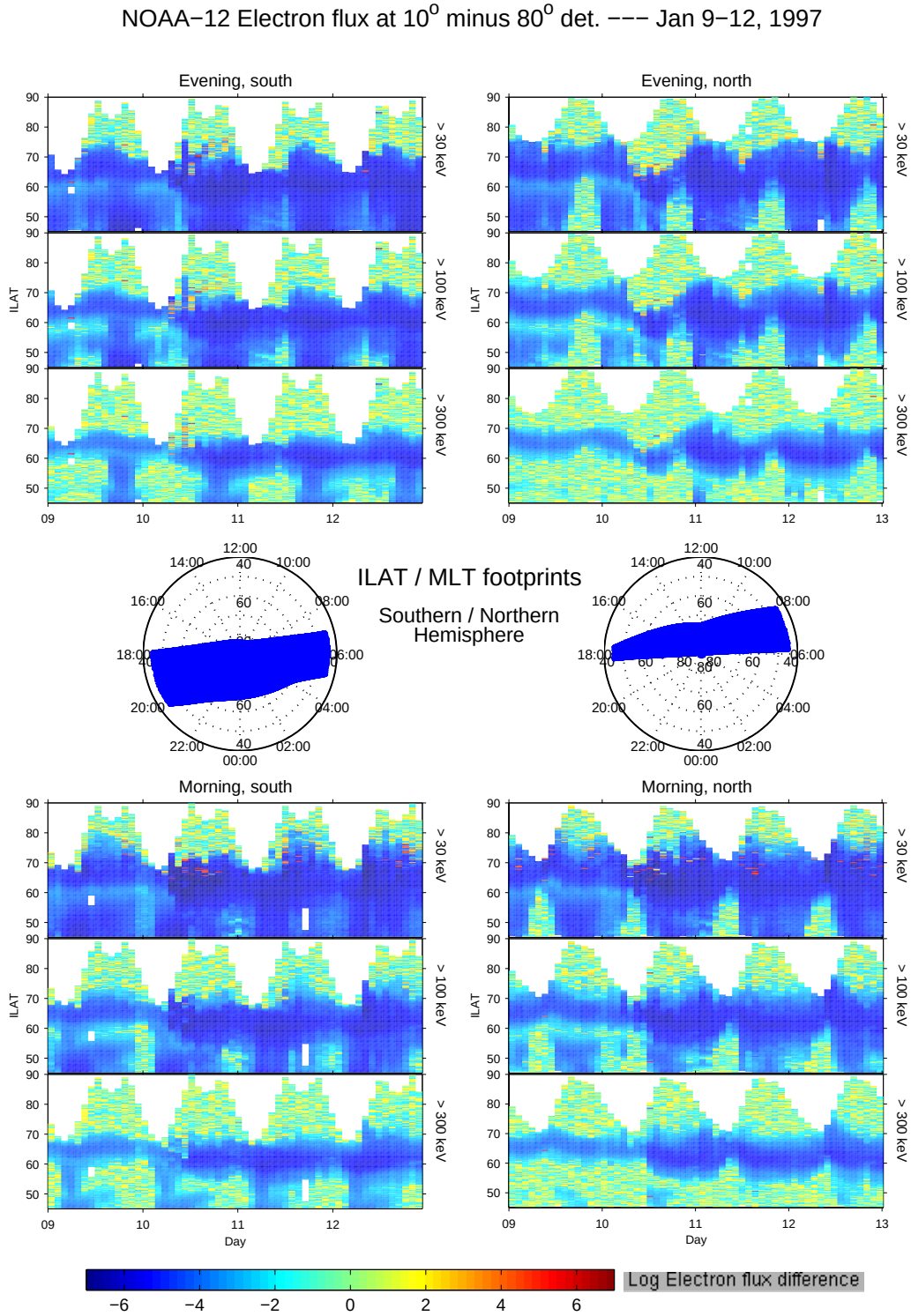

FIGURE 3.20 NOAA-12 MEPED Electron Flux Difference for three energy channels (>30 keV, >100 keV & >300 keV) vs. Invariant Latitude and Time January 9-12, 1997. Red colours where the precipitating flux is larger, blue where the trapped flux is larger and green where the fluxes are equal.

3.6 NOAA-12 TED Data

The TED detector provide measurements of the low energetic protons and electrons in the 300 to 20000 eV energy range. Four channels are transmitted to ground for both the electron and proton sensor, Section 2.1.1. If the TED data sets are run through the same routine as the MEPED data sets and ordered in sectors, four energy panels in each sector are obtained. However, since the time resolution is 8 and 16 seconds for the TED data sets in contrast to 2 seconds for the MEPED data sets, one has to increase the width of each box from 0.25 to 1.0 degrees in magnetic latitudinal extent, thereby reducing the latitudinal resolution.

3.6.1 The TED 0˚ Electron Sensor

In Figure 3.21 the NOAA-12 TED low-energy precipitating 0 degree electron fluxes from January 9-12, 1997, are displayed. The first thing to notice is how all the fluxes tend to have their maximum intensity at the higher-latitude border of the precipitation area and how the low-energy electron flux is usually never found equatorward of the high-energy electron flux in Figure 3.15. In fact, a energy vs. latitude dispersion is seen in the electron data. In Figure 3.11 and Figure 3.5 the lower-energy channels show the peak intensity further poleward than the higher-energy ones. This is in good consistency with the general theory of the magnetosphere, where low energetic particles are believed to enter the magnetosphere only at open magnetic field lines or in the open/closed magnetic field line region. Low-energy particles can not persist for longer time periods in the inner magnetosphere, because through acceleration processes the energy of a trapped particle is increased as it moves inwards from the open/closed boundary.

Of interest is also the strong intensification on January 10. In the southern hemisphere the low-energetic precipitating areas get very intense and wide in latitudinal extent, especially in the evening sector. In the northern evening sector a clear equatorward motion is also observed on January 10. Both occurrences appear at the same time as examined in Section 3.3.1 to Section 3.3.4.

In the end of January 10 and beginning of January 11 a very strong intensification is observed in the northern hemisphere in only the lowest (300-458 eV) energy channel. The rise in the flux is observed in three successive NOAA-12 passes from ~21:39 UT to ~01:16 UT (perhaps until ~02:58 UT) in both the morning and evening sectors. This is at the time when the plasma filament hit the magnetosphere.

3.6.2 The TED 0˚ Proton Sensor

In Figure 3.22 the NOAA-12 TED low-energy 0 degree precipitating proton fluxes are shown. Of great interest is the very strong spot in the beginning of January 11 in the northern morning sector. The spot is first weakly observed in the January 10 ~21:53 UT pass, growing at ~23:34 UT, before it disappear after ~03:10 UT on January 11. This disappearance may be artificial, because the spot is observed at the edge of the field-of-view. Nevertheless, the spot is observed about the same time as in the electrons. Within this interval the low-energy precipitating proton flux reaches the maximum of the whole four-days period. The peak is strongest in the 300-458 eV proton channel and is decreasing in intensity with increasing energy. An increase in the fluxes is also observed at the same time in the southern morning sector, but far from as intense as in the northern hemisphere.

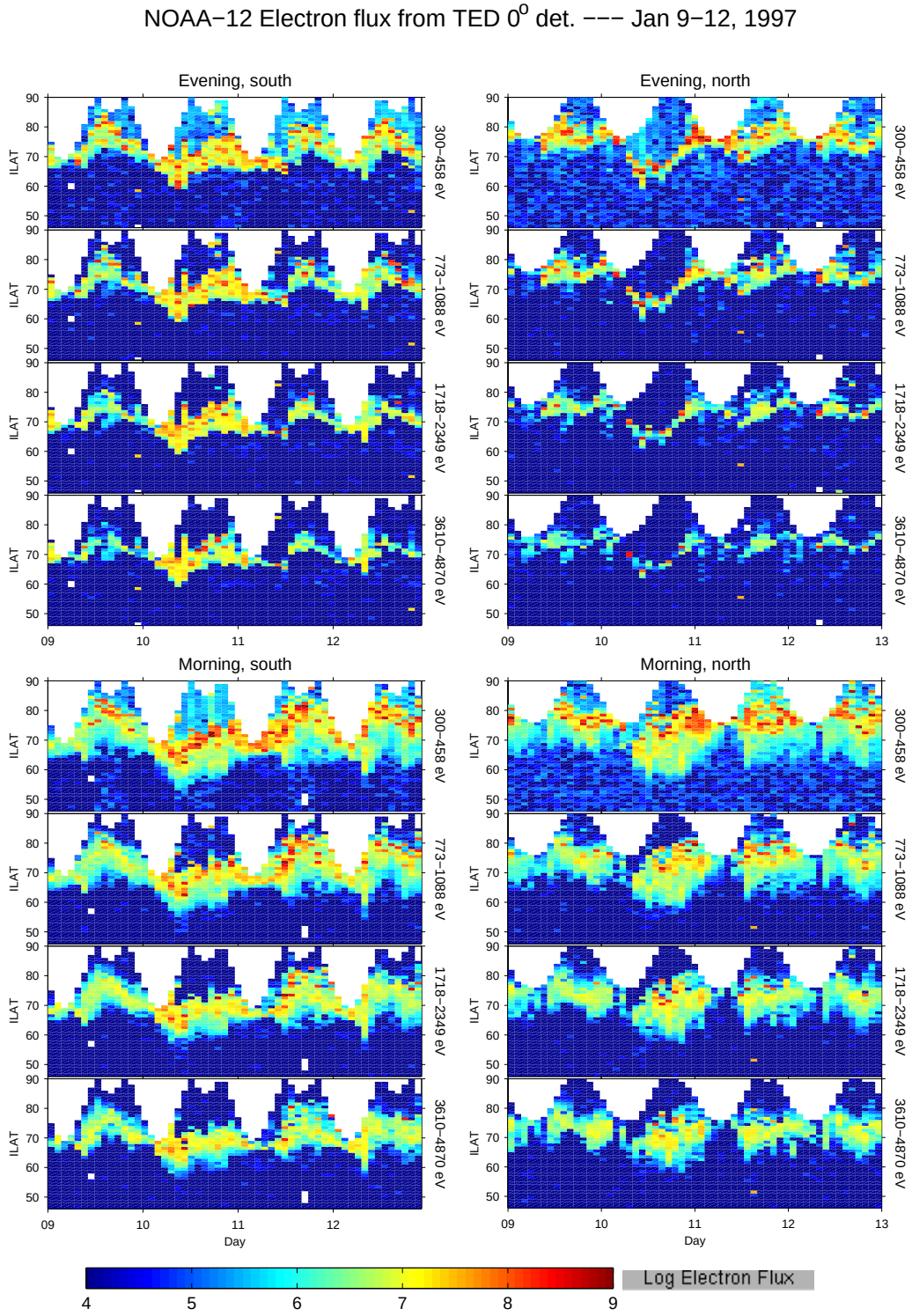

FIGURE 3.21 NOAA-12 0° TED Electron Fluxes from four energy channels (300-458 eV, 773-1088 eV, 1718-2349 eV & 3610-4870 eV) vs. Invariant Latitude and Time, January 9-12 1997. The Magnetic Evening (Morning) Sectors are at the top (bottom). The Southern (Northern) Hemisphere is to the left (right).

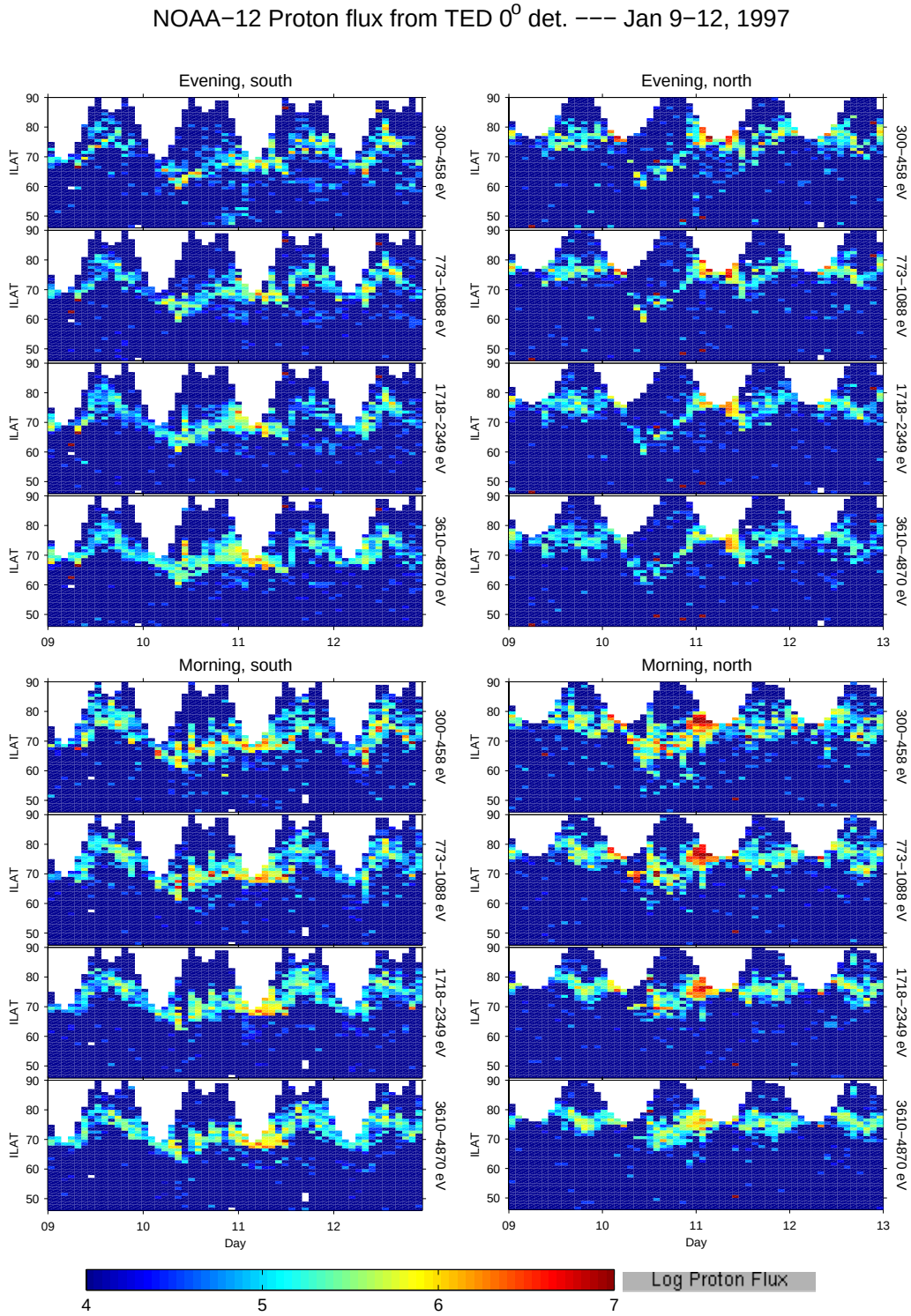

FIGURE 3.22 NOAA-12 0° TED Proton Fluxes from four energy channels (300-458 eV, 773-1088 eV, 1718-2349 eV & 3610-4870 eV) vs. Invariant Latitude and Time, January 9-12 1997. The Magnetic Evening (Morning) Sectors are at the top (bottom). The Southern (Northern) Hemisphere is to the left (right).

The observations of soft precipitating protons in the morning sector can be explained. For the soft particles the magnetic drift may be ignored (*K* is small in Equation 3.8). Thus, the E×B-drift, Equation 3.7, is dominating, and combined with the corotation electric field $\boldsymbol{E_{corot}}$ transports the low-energy protons from the nightside to morning side, instead of towards the evening side as for the energetic protons. This is indicated with the medium solid arrow, which emanates from the thick solid high-energy proton drift in Figure 3.16. [Lyons and Williams, 1984, Figure 4.27] also displays this effect.

[Newell and Meng, 1992] also mention observations of soft ions in their CPS morning side band, extending from 06 MLT towards noon. *"This band is primary due to keV electron precipitation, with some associated ion precipitation (sometime the ions are at much lower energies)."* However, due to our selection procedure (morning equals 00-12 MLT) and NOAA-12's orbit, the most poleward precipitation in the summary plots is rather closer to noon. So, the intense spot in the proton precipitation may possibly correspond to [Newell and Meng, 1992]'s CPS map near noon, extending in average up to 75^{o} ILAT, but may also be of LLBL or cusp origin. This is however not of any importance here and will not be stressed any further.

Of great interest is also the equatorward motion of the low-energy proton precipitation seen on January 10 in the northern evening sector. But the fluxes here are small (factor 10 to 100 less) compared with the morning sectors. This displacement is also simultaneous with that discussed in Section 3.3.1 to Section 3.3.4.

3.7 Discussion

Let us first focus on the intensification followed by an equatorward motion of the oval seen in Figures 3.12 to 3.15 on January 10. From Section 3.3.1 to Section 3.3.4 an enhancement was observed at 04:50 to 05:15 UT in the northern hemisphere reaching the maximum from ~08:14 UT. About this interval Figure 3.9 shows a stable time shift of 24-26 minutes. From Section 3.2.2 the IMF clock angle was observed continuously in regime CAR 3 from 04:41 UT, which corresponds to just after ~05:05 UT in the ionosphere when the time delay is taken into account. However, the clock angle had been switching between CAR 2 and 3 some time before the NOAA-12 pass. So, the enhanced fluxes in the NOAA-12 observations is probably a combination of this switching rather than a direct result of the turning to CAR 3. The precipitation/trapped region, yet not shifted equatorwards, is also supporting this. However, the next pass in the northern hemisphere at 06:32-07:00 UT, corresponding to around 06:07-06:35 UT at Wind, is well within the period of CAR 3, and the region in the northern evening sector is observed to have shifted some equatorwards.

In the subsequent NOAA-12 pass in the southern hemisphere ~07:23-07:50 UT (~06:58-07:25 UT at Wind) the first sharp increase in the particle fluxes was observed. In the following northern hemisphere pass about ~08:14 UT (~07:50 UT at Wind) the particle fluxes showed the first strong intensification and equatorward displacement in evening sector. In both passes the clock angle was very large (>165°) for a longer period. At the same time the IMF Bz component was very strong southward, about -15 nT. The Dst-index was also falling off very rapidly. The other solar wind parameters (density, temperature, thermal velocity and flow velocity) did not show

any remarkable change at this time. So, the event must be caused by the changes in the IMF.

The equatorward motion of the energetic particle precipitation during disturbed conditions has also been studied by others. From ESRO IA and IB observations of >100 keV protons, [Søraas, 1972] found an equatorward motion of the low latitude boundary of the proton precipitation in the nightside in connection with geomagnetic storms: *"It can be seen that the equatorward boundary moves to lower latitudes with increasing geomagnetic activity. Its location depends significantly on Dst and to a lesser extent on the Kp index. The location of the equatorward boundary does not depend significantly on the AE index, … . The poleward boundary on the other hand seems to depend solely on the AE index."* Søraas also studied the poleward boundary: *"There is a general tendency for the poleward boundary to move to higher latitudes with decreasing Dst, but as the statistical analysis has shown, this boundary depends mostly on the AE index. There is an indication in the data that the poleward boundary starts to move equatorward when the Dst decreases below -60 γ."*

The other event in the beginning of January 11 was observed in the northern hemisphere ~ 01:02-01:30 UT (a 29 min. time delay gives ~ 00:33-01:01 UT at Wind) in the northern morning sector. In that period the clock angle was well within CAR 1, the IMF {~ -3, ~ -6, ~ 13} nT. At the same time the electron density, the electron temperature, the ion density and the ion temperature were stable at ~ 4 cm^{-3}, ~ 3 eV, ~ 25 cm^{-3} and ~ 4 eV, respectively. The rather high ion density is probably an important source of the enhanced particle fluxes observed by NOAA-12 in the beginning of January 11. The fact that NOAA-12 observed increased fluxes in several passes both before and after this interval may be combined with the ion density. The ion density was increasing from about 21-22 UT on January 10, reaching a maximum from about 01:00-03:10 UT at Wind on January 11, before the return towards lower densities. At the same time the enhanced particle fluxes was detected especially in the 0° TED proton detector in the northern morning sector, but also to some degree in the other sectors.

The fact that the IMF was quite intense northward (~ 13 nT) and turning even more northward after 01 UT suggests a poleward retreat of the polar cap. However, since NOAA-12's orbit does not cross the magnetic pole in every pass, any activity poleward of its orbit is not monitored. Consequently, the very strong northward IMF after the 01 UT pass January 11 suggests a poleward motion of the activity out of NOAA-12's field-of-view. This may also explain why the fluxes in the southern hemisphere is slightly less than in the northern about this pass and why the fluxes seem to decrease in latitudinal width after the 02-03 UT passes on January 11.

The very good agreement between the positive spike in the Dst-index and the introduction of protons in the morning sector and electron in the evening sector at 01-02 UT January 11 must also be commented. The energetic protons show enlarged both trapped and precipitating fluxes in both the morning sectors about this interval, and the low-energetic precipitating protons also show the same pattern. The energetic electrons show enlarged fluxes in the evening sectors, especially for the precipitating ones in the northern evening sector.

The energetic particle data (especially the trapped fluxes in Figure 3.12 and Figure 3.14) reveal a diurnal pattern below about 60° ILAT. This is due to particle loss effects near the South Atlantic magnetic field anomaly. [Berg and Søraas, 1972] studied the longitude varia-

tion of locally mirroring >100 keV protons in low altitude. They found reduced number fluxes near 0˚ and 360˚ geographic longitude, caused by an increased atmospheric loss cone as the effect of the protons mirroring in a lower altitude in the southern hemisphere. However, during disturbed conditions the longitudinal dependence of the flux levels were less clear, as a result of the loss cone being continuously filled with particles.

3.8 Summary

An overview of the trapped and precipitating electron and proton fluxes as observed from NOAA-12's MEPED and TED detectors January 9-12 1997 has been given, dividing each hemisphere crossing into morning and evening sectors. The particle data have been compared with the Dst-index, and the good agreement is striking. Solar wind parameters from the same time have been presented and the associated time delay calculated.

Then the solar wind parameters was briefly compared with the NOAA-12 observations. A good consistency between the IMF clock angle in CAR 3 regime, the equatorward motion in the northern hemisphere and the intensifications in the morning of January 10 was found. At the same time the other solar wind parameters remained almost unchanged, suggesting the IMF to be the most important factor in the solar wind in creating this event. A huge increase in the ion density was also connected to the enhancements in the NOAA-12 particle fluxes at ~ 01-02 UT January 11. The simultaneously positive spike in the Dst-index was found to match observations of increased fluxes of protons in the morning sector and electrons in the evening sector.

This data set of January 9-12 1997 contains many more interesting features and other aspects that could also be mentioned. But, because of time and space limitations these must be left to future work. However, now a brief overview of the Wind and NOAA-12 observations has been presented and will serve as a reference for the events to be discussed later.

In the next Chapter some basic terms and principles of the dayside aurora are discussed, before further studies of some single NOAA-12 passes above Svalbard in Chapter 5.

Chapter 4

The Dayside Aurora

A brief introduction to the dayside magnetospheric configuration, different source regions of particle precipitation, models and dayside optical emissions

4.1 The Magnetosphere

The continuous interaction process between the solar wind and the geomagnetic field gives a magnetopause, the instant surface of pressure balance. The dominant terms in this "equilibrium" are, [Mead and Beard, 1964]:

$$p = \frac{B_t^2}{2\mu_0} \qquad (4.1)$$

where p, B_t and μ_0 are the solar wind ion pressure, the magnetic field intensity just within the magnetopause and the permeability of vacuum, respectively. This magnetopause is constantly moving due to the changing solar wind parameters. So, this "equilibrium" is not stable in time. Inside this border, where the Earth's magnetic field is dominating, is the magnetosphere.

In front of the magnetopause a bow shock is formed by a fast magnetosonic wave. This bow shock marks an outer border towards the undisturbed solar wind. Passing through the bow shock, the supersonic solar wind is slowed down to a subsonic speed. This gives a region of shocked turbulent solar wind plasma, the magnetosheath, between the bow shock and the magnetopause. A schematic overview of the bow shock, the magnetosheath, the magnetosphere and some particle source regions within the magnetosphere (to be discussed in the next sections) is given in Figure 4.1.

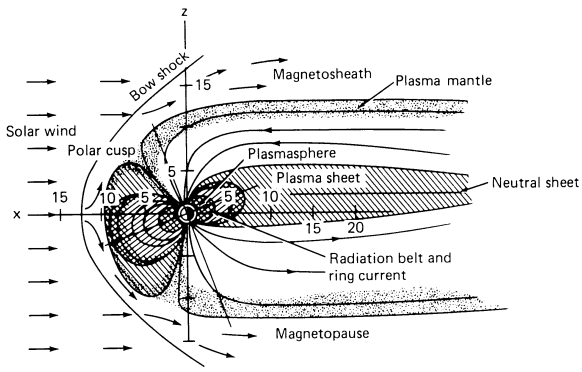

FIGURE 4.1 The magnetosphere, from [Lyons and Williams, 1984].

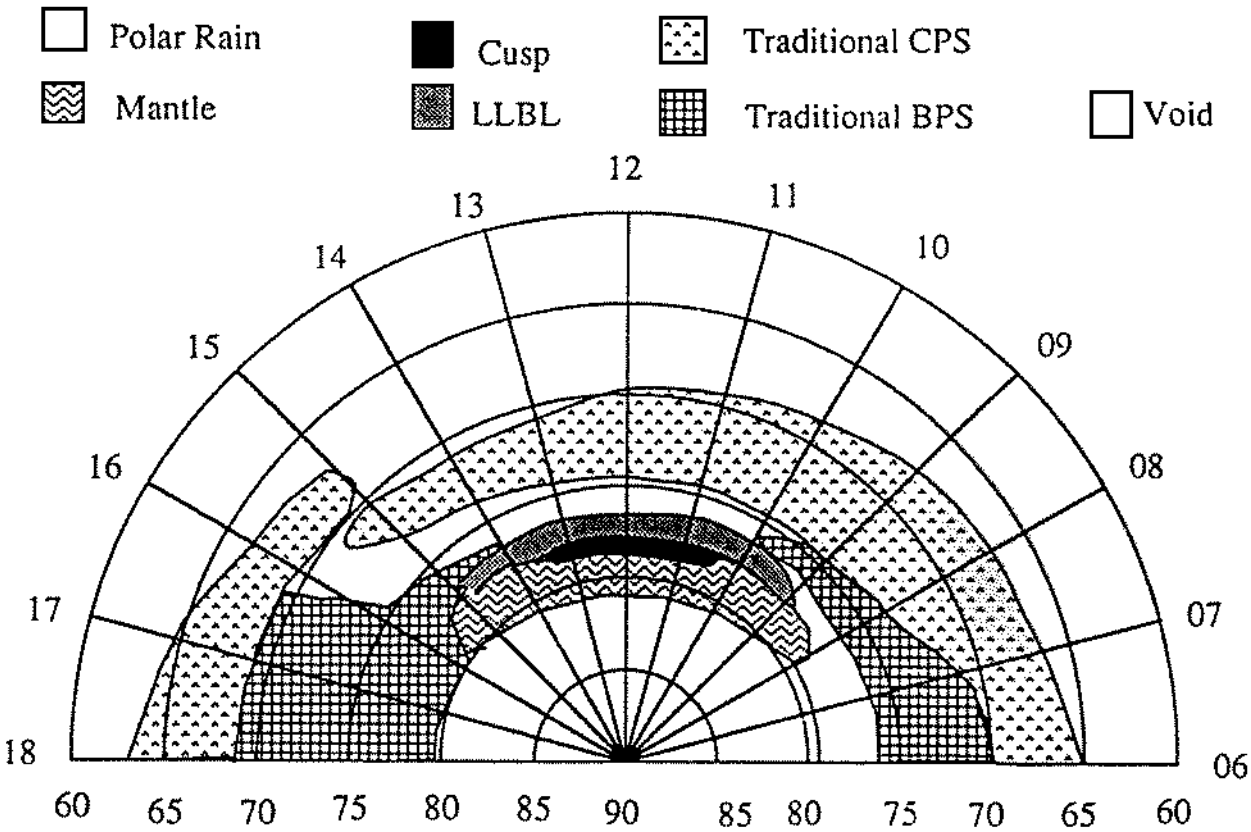

FIGURE 4.2 A map of the ionosphere to the magnetosphere based on plasma characteristics. 60,000 DMSP passes was automatically processed during different IMF conditions, from [Newell and Meng, 1992].

4.2 Particle Source Regions

Several statistical studies of the particle precipitation using particle observations from low-altitude satellites has been done during the years, [e.g. Wedde et al., 1973; Marøy, 1977; Gussenhoven et al., 1985]. Wedde et al. presented measurements of >40 keV electron and 115-180 keV proton precipitation from the ESRO IA satellite. For different levels of geomagnetic activity (the Kp index) they divided the data set into sectors; midnight, morning, dawn-noon, noon-dusk and evening, from which Wedde et al. presented average particle fluxes vs. invariant latitude.

However, [Newell and Meng, 1992] were the first to present probability maps (Figure 4.2) of observing precipitation from specified magnetospheric regions in the ionosphere from an automatic source region identification. Using a neural network, [Newell et al., 1991c], to automatic identify 60,000 low-altitude polar orbiting DMSP passes through the dayside auroral oval, [Newell and Meng, 1992] were able to create the first probability maps for observing precipitation of plasma from the cusp, the LLBL, the mantle, the BPS or the CPS into the ionosphere vs. magnetic latitude and local time. Newell and Meng's first results suggested a cusp 2.5 hours

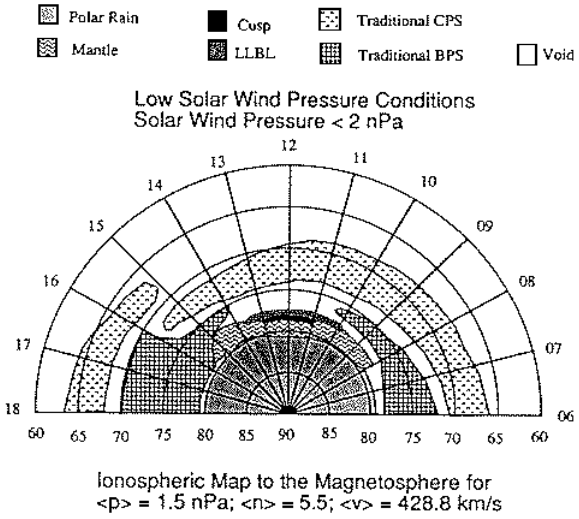

FIGURE 4.3 The projection of magnetospheric regions into the ionosphere based on precipitation characteristics observed at low altitudes during low solar wind pressure, from [Newell and Meng, 1994].

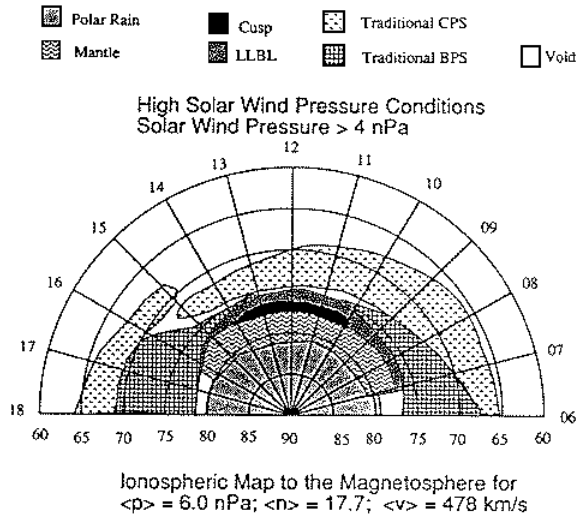

FIGURE 4.4 The projection of magnetospheric regions into the ionosphere based on precipitation characteristics observed at low altitudes during high solar wind pressure, from [Newell and Meng, 1994].

wide in MLT, a LLBL out to about 0900 MLT and a mantle 0800 to 1600 MLT. They also found the discrete nightside aurora extending further towards dusk than dawn. Based on these different probability maps (not shown here), they made the summarizing map of all the regions, shown in Figure 4.2.

During this first processing, Newell and Meng did not take the IMF orientation into account. Figure 4.2 is therefore an average of different IMF orientations and diurnal and annual effects. So, deviations from the map are rather the rule than the exception. E.g. using a unique DMSP F11 pass longitudinally cutting the cusp and mantle and simultaneous optical measurements from Svalbard on January 12 1993 [Maynard et al., 1997] found the cusp to be at least 3.7 hours wide in MLT.

Later, [Newell and Meng, 1994] made new probability maps also taking different solar wind conditions into account. They found the mapping of regions to be strongly correlated with the solar wind pressure and developed therefore the new probability distributions for the mantle, the cusp, the LLBL, the BPS and the CPS vs. low and high solar wind pressure shown in [Newell and Meng, 1994, Plates 2 to 6]. From these 2×5 distributions and four rules for selecting the dominating region at a given position, Newell and Meng also created the two new summarizing maps shown in Figure 4.3 and Figure 4.4. Here it is seen how the cusp and LLBL is much wider during a high solar wind pressure. In fact, Newell and Meng found a cusp area of 4.83 degree-hours (MLAT $\times$ MLT) and 1.01 degree-hours (MLAT $\times$ MLT) in the ionosphere during high ($p \geq 4$ nPa) and low ($p \leq 2$ nPa) solar wind kinetic pressure, respectively. Looking at these maps it is important to keep in mind, as noted by Newell and Meng, that the statistics below

70° MLAT at 15 to 18 MLT is bad and must be treated with caution, since the DMSP F7 and F9 satellites were infrequent sampling that region.

Having briefly introduced a framework, including the yet undefined terminologies cusp, LLBL, mantle, BPS and CPS of Newell and Meng, it is clear that these terms need to be specified. This will be done in the following subsections.

4.2.1 The Cusp

Several definitions may be applied to specify what is the 'cusp', using either the cusp in the magnetic field and/or the cusp observed in particle spectra. [Heikkila, 1985] presented the following definition of the cusp and cleft: *"The cleft is the low altitude region around noon of about 100 eV electron precipitation associated with 6300 Å emission, but containing also structured features of higher energy. The cusp is a more localized region near noon within the cleft characterized by low energy precipitation only, having no discrete auroral arcs, but often displaying irregular behaviour, presumably associated with the magnetic cusp.*" However, it is not always guaranteed that the magnetic and particle cusps are identical, and modelling the magnetic field, especially in the cusp region, is not directly easy. Thus, another definition making directly use of the observed particle characteristics is preferred here, as proposed by [Newell and Meng, 1988]: *"The low-altitude cusp is the dayside region in which the entry of magnetosheath plasma is most direct. Entry into a region is considered more direct if such particles maintain more of their original energy spectral characteristics.*"

How may the cusp be identified in practice? [Newell et al., 1991b] has presented a brief guide how to identify the source regions of precipitation observed on the dayside. Their cusp or "cusp proper" is characterized by very high fluxes of particularly ions. These ions typically have a spectral peak of 10^8 eV/cm^2 s sr eV or more, which is higher than elsewhere in the auroral oval. The probably most clear characteristic of the cusp, is the ion energy being dominated by the bulk flow velocity, and not the thermal energy. The electron temperature is below 100 eV, typically 30 to 100 eV, [Newell and Meng, 1992], giving an average energy below 200 eV, [Newell et al., 1991b]. Usually, although not always, a dropout of the ions above a few keV is seen as a poleward moving satellite enters into the cusp, and an energy vs. latitude dispersion also observed, see e.g. [Newell et al., 1991a, Plate 1].

Some statistical works have also been done, investigating the ionospheric mapping of the cusp. [Newell and Meng, 1988] used 1 year (5609 passes) of DMSP F7 precipitating electron and ion data in the 32 eV to 30 keV energy range. They defined several criteria, suitable for their DMSP data sets, before processing all the passes through the cusp and LLBL regions:

- If the energy flux in the 2 or 5 keV electron channel was less than 10^7 eV/cm^2 s sr eV, $j_e > 6\times 10^{10}$ eV/cm^2 s sr, $j_i > 10^{10}$ eV/cm^2 s sr, $E_e < 200$ eV and $E_i < 2700$ eV, the region was cusp.
- If the energy flux in the 2 or 5 keV electron channel was less than 10^7 eV/cm^2 s sr eV, $j_e > 6\times 10^{10}$ eV/cm^2 s sr, $j_i > 10^{10}$ eV/cm^2 s sr, and 3000 eV $< E_i <$ 6000 eV or 220 eV $< E_e <$ 600 eV, the region was LLBL.
- Else the region was neither cusp or LLBL.

j_e , j_i , E_e and E_i are the electron and ion energy fluxes and the average electron and ion energies, respectively.

From these simple algorithms, [Newell and Meng, 1988] found the probability of observing the cusp peaked near noon, dropping off rapidly away from noon. Their cusp showed a latitudinal width of 0.8-1.1^{o} MLAT at noon, the width being rather independent of local time. Newell and Meng also found the precipitating ion number flux 3.6 times larger in the cusp than the LLBL. The spectral characteristics varied little with local time, and a peak in the energy flux was observed near 1400-1430 MLT, although the probability of observing the cusp here is lower than at noon. Individual cusp passes showed the peak ion flux near the equatorward boundary (associated with southward IMF Bz) or no peak ion flux at all. A statistical average also showed the peak energy flux closer to the equatorward than the poleward boundary.

How is the pitch angle distribution within the cusp? Particle observations from the Viking satellite showed the cusp plasma to be dominated by isotropic magnetosheath electrons and structured fluxes of ions, [Lundin, 1988]. This is also confirmed by e.g. the cusp particle spectra of [Reiff et al., 1977]. From DE-2 plasma observations in the mid-altitude cusp (~ 4 Re) [Burch et al., 1982] also reported the ions to have a pitch angle "V"-shape (*log E* vs. α_o). The peak energy flux occurred at a higher energy for a larger pitch angle. Sometimes the electron observations displayed this pattern too. Burch et al. also noted from their model that in low-altitude (~ 900 km) the "V"-signatures become weaker and disappear.

The cusp is also a region of intense wave activity. E.g. combining the Halley coherent scatter HF-radar and the DMSP F9 satellite [Baker et al., 1990] observed 10-m scale irregularities and severe electron field turbulence generated in the cusp. [Marklund et al., 1990] have also presented observations of irregular and burst-like electric fields. Using the Viking satellite in high-altitude Marklund et al. found a persistent wave activity in the cusp with broad-band spectra in the 0.1 to 0.4 Hz frequency range, in contrast to the more sharply peaked spectra in the rest of the dayside oval and cleft.

4.2.2 The LLBL

In older publications, e.g. [McDiarmid et al., 1976], the Low-Latitude Boundary Layer (LLBL) region is called the 'cleft', and the term 'LLBL' is not mentioned at all. Later works, e.g. [Newell et al., 1991b], widely use the name 'LLBL' instead, while the 'cleft' term is completely omitted. This may perhaps be the result of an evolving idea where the LLBL is thought to be the closed low-latitude border of the open cusp field lines.

The LLBL is very much similar to the cusp, however, the plasma is more thermalized with hotter ions and lower ion bulk flow velocities. The electrons are also a bit hotter in the LLBL, see e.g. the ISEE 1 low-latitude magnetopause crossings in [Eastman et al., 1985]. [Newell et al., 1991b] found their inferred ion densities a factor ~ 5 smaller, and the spectral peak in the ion flux a factor ~ 10 smaller (~ 10^7 eV/ cm^2 s sr eV) than in the cusp. The total electron number fluxes are less than in the cusp, but the high-energy portion of the particle population lift the electron energy flux up to almost the same level as in the cusp. Usually, a higher percentage of magnetospheric high-energy particles is observed, with the electrons tending to be more beam-like, rather than isotropic, [Lundin, 1988]. E.g. from electron distribution functions from the ISEE 1 satellite in the high-altitude LLBL, [Ogilvie et al., 1984] found several cases of bidirectional field-aligned streaming distributions or a net flow of electrons along the magnetic field.

The LLBL electron temperatures are higher than in the cusp, about 70 to 200 eV [Newell and Meng, 1992], giving an average electron energy less than 400 eV [Newell et al., 1991b]. The density varies from 0.5/cm^3 to about 10/cm^3, the flow velocities from 100 km/s to magnetosheath values (or even higher, up to more than 800 km/s) and the temperatures from 100 to 1000-2000 eV [Newell et al., 1991b].

From the criteria in Section 4.2.1 on page 58 [Newell and Meng, 1988] found the probability of observing the LLBL near unity away from noon, with a minimum at noon. [Newell and Meng, 1992] also found good chances for observing the LLBL out to about 0930 MLT, and some identifications were done before 0830 MLT, however, not "classic" examples. Newell and Meng suggested the asymmetry seen in the postnoon sector might be explained by the Region 1 current pointing out of the ionosphere (associated with electron acceleration events). This field aligned potential drop experienced by a precipitating electron, modify the energy spectrum and the straightforward LLBL identifications based on the known typical high-altitude observations brake down. Another study by [Newell et al., 1991b] also found the LLBL to correspond to the Region 1 current, and they got a potential drop of 5 keV across the LLBL in their limited sample.

Based on 9 DMSP passes, where the LLBL was wide (~ 1.85^o MLAT in average) and easily identified, [Newell et al., 1991b] found the convection reversal boundaries (CRB) closest to the equatorward boundary of the LLBL. In average the CRBs were occurring at typically ~ 30% of the LLBL width, poleward of the equatorward boundary. The most equatorward portion of the LLBL was convecting very erratic or slow, while the rest of the LLBL was dominated by antisunward convection. Later, [Sandholt et al., 1993] also found the CRB within the LLBL during a DMSP F9 pass January 12 1991.

Using 2-dimensional particle velocity distributions obtained from the Fast Plasma Experiment on board the ISEE 2 spacecraft [Gosling et al., 1990] found the inner edge of magnetosheath electrons earthward of the inner edge of magnetosheath ions (i.e. at a lower latitude in the ionosphere) in the LLBL during accelerated flow events. This is a consequence of the magnetosheath electrons having higher parallel velocity than the ions, while the transverse drifts are the same.

Is the LLBL on open or closed field lines? This is an important question to solve out. The LLBL is probably one of the most important magnetospheric borders towards the magnetosheath solar wind plasma. So, to better understand the solar wind vs. ionosphere energy transfer, the degree of this coupling in the LLBL is of great importance. Is this connection direct (i.e. an open LLBL) or indirect (i.e. closed LLBL)? The rest of this subsection is devoted to this subject.

Closed LLBL

Using many observations during magnetic quiet conditions (Kp < 3) in the 1000 to 1200 MLT and 1400 to 1600 MLT sectors of soft electrons and protons and energetic electrons from the Isis 2 satellite (circular polar orbit at 1400 km altitude) in 1971 and 1972, [McDiarmid et al., 1976] found the average electron spectrum harder (more often > 1 keV electrons) postnoon than prenoon MLT. They also discovered protons more frequently prenoon than postnoon. Together with observations of anisotropic pitch angle distributions in the cleft (today: LLBL), McDiarmid et al. suggested the cleft was on closed field lines during average conditions.

Later, [Eastman and Frank, 1982] used ISEE plasma observations of 1 eV to 45 keV electrons and positive ions from a magnetopause crossing September 8, 1978, and was able to find the velocity distributions near the magnetopause. An observed high-speed ion flow in the boundary layer was consistent with the acceleration from reconnection. However, observations of low-energetic plasma inconsistent with the tangential stress balance, the lack of any normal flow component v_n and pancake-shaped pitch angle distributions seen in the > 45 keV electrons led Eastman and Frank to suggest the entire LLBL is on closed field lines.

Open LLBL

Afterwards, [Curran and Goertz, 1989] studied particle orbits in a two-dimensional steady state reconnection field geometry model. Curran and Goertz showed how a trapped ion distribution (which have a peak near 90° pitch angle) can exist on topologically open magnetic field lines in the magnetosphere. At the magnetopause the magnetic moment is not conserved, since the scale length of the magnetic field is of same order as the gyroradius of the particles. Therefore, an adiabatic assumption is not valid here, and non-adiabatic reflections and energetizations may occur. The conclusion from [Eastman and Frank, 1982] implicitly took for granted that particles move adiabatic all the time. From their calculations [Curran and Goertz, 1989] thus concluded that the observations of [Eastman and Frank, 1982] can best be explained in a open magnetopause model with a tangential electric field, hence a open LLBL.

Thereafter, [Moen et al., 1996] combined groundbased optics from Ny Ålesund with particle measurements from NOAA-12 during an event of dayside moving transients in the magnetic postnoon region. Their particle observations revealed that the auroral forms were associated with a population of injected magnetosheath plasma mixed with a secondary component for magnetospheric ions of energies > 30 keV and well poleward of the CPS. Therefore, Moen et al. classified the region as LLBL and on open field lines at least along the track of NOAA-12. The auroral transients were consistent with footprints of reconnection, both patchy and sporadic in time, at the dayside magnetopause.* The same NOAA-12 particle observations were also studied by [Lockwood and Moen, 1996], who were able to describe the data with an open magnetopause model allowing for transmission of magnetosheath ions across one or both of the two Alfvén waves emanating from the magnetopause reconnection site. Their model was based on the work of [Lockwood et al., 1996]. The very good agreement between model results and observations, led [Lockwood and Moen, 1996] to propose the events and the LLBL precipitation were both on open field lines.

Both Open and Closed LLBL

[Newell and Meng, 1998] have presented two DMSP passes through the LLBL; one pass near noon and one in the prenoon sector. In their noon pass [Newell and Meng, 1998, Figure display 1†] the LLBL was classified as being on open field lines immediately equatorward of the cusp. The open LLBL is a narrow region of electrons at approximately the same energy as in the cusp, but with a lower density, which was explained by Newell and Meng as

* In a most recent paper, [Moen et al., 1998] reported these dayside auroral forms also to be correlated with a bursty H_β proton auroral activity. The simultaneous occurrence of both proton (486.1 nm) and electron (630.0 nm) aurora further supports a magnetopause reconnection mechanism injecting magnetosheath plasma on the dayside.

† In [Newell and Meng, 1998] an error has occurred probably during typesetting.
The titles of Figures 1 and 2 are interchanged, so Figure Display 1 is described in Figure Title 2.

the result of charge quasi-neutrality (the more slowly moving ions have not had the time to reach the ionosphere, giving a retarding potential which keeps the majority of the electrons away). Within and equatorward of the open LLBL they found a population of high energy (i.e. > 10 keV) ions, but the low energy magnetosheath electrons showed a cutoff by the equatorward border of the LLBL. Therefore, Newell an Meng classified the region equatorward of the LLBL as CPS.

In Newell and Meng's prenoon pass around 10 MLT [Newell and Meng, 1998, Figure display 2‡] the LLBL was classified as being on closed magnetic field lines. Although observation of no significant fluxes of high energy electrons would indicate an open LLBL, lower ion densities typical 1/5 of the density in the magnetosheath, slightly higher electron temperatures and spectrally complete ions with no low energy ion cutoff are indicating that the LLBL was on closed field lines during this DMSP pass. The LLBL was also observed on antisunward convecting field lines. Equatorward of the LLBL a region of magnetosheath plasma overlapping several keV electrons on sunward convecting field lines was classified as BPS.

Other low-altitude observations also confirm this picture; a closed LLBL only away from noon and an open LLBL only immediately equatorward of the cusp [Newell and Meng, 1998]. This led Newell and Meng to suggest that the merging rate is depending on magnetic local time (peaked near 12 MLT and declining away from noon) while the diffusion rate is constant. Consequently, near noon the stripping away of magnetosheath plasma on closed field lines is too rapid, and any population of magnetosheath origin cannot persist on closed field lines there. However, away from noon the merging rate is lower, and the dominating diffusion rate is able to maintain a closed boundary layer.

4.2.3 The Mantle

Compared with the cusp, the mantle particles are de-energized magnetosheath plasma. The mantle is therefore the region containing the lowest average ion energy at higher latitudes [Newell et al., 1991b]. Usually, the average ion energies (flow + thermal) are only a few hundred eV. The flow and thermal velocities generally decline poleward, and the densities are also much lower than in the cusp and LLBL. The temperatures range from a few tens of eV up to ~ 100 eV, the densities typically 10^{-2} to 10^{-1} cm^{-3} and the flow velocities 100-200 km/s [Newell et al., 1991a; Newell et al., 1991b].

An example of the most intense mantle precipitation is the "cusp plume", a poleward low-energetic ion extension of the cusp seen during particular IMF Bz southward and strong poleward convection and a latitudinal narrow cusp, e.g. [Shelley et al., 1976; Reiff et al., 1977]. The "cusp plume" is characterized by the highest number fluxes of the mantle, typically ~ 10^7 ions/cm^2 s sr, [Newell et al., 1991a]. Examples of "cusp plumes" are presented by e.g [Reiff et al., 1977, Figure 4 & Figure 5b; Newell and Meng, 1988, Plate 1; Newell et al., 1991a, Plate 1]. Away from noon (and the cusp) the mantle is also found. [Newell et al., 1991a] shows several examples of this, e.g. in their Plate 2. This mantle at the dayside flanks is characterized by lower fluxes (a little less than 10^6 ions/cm^2 s sr).

‡ Same reason as in Footnote †.
Figure Display 2 is described in Figure Title 1 of [Newell and Meng, 1998].

[Newell et al., 1991a] mention several criteria of identification they used for the mantle:

- Location, poleward of the cusp and dayside auroral oval.
- General tendency of the density and average ion energy to decline with increasing latitude.
- Drift meter measurements showing antisunward convecting field lines in the mantle.
- Fitted convecting Maxwellian distributions having ion temperatures from a few tens of eV up to about 100 eV and ion densities from a few times 10^{-2} to a few times 10^{-1} cm^{-3}.

In a statistical study, combining particle and magnetic field data from 48 Viking orbits, [Erlandson et al., 1988] discovered the traditional cusp current (now: mantle current) to map to the plasma mantle instead of the cusp. Their mantle current was observed near noon and poleward of the Region 1 current, which was found to be associated with the most intense flux of magnetosheath like electrons. Erlandson et al. also encountered a IMF By dependency in the MLT location and extent of both the prenoon and postnoon parts of the Region 1 and mantle currents. Later, [Newell et al., 1991a] also found their mantle in agreement with mantle current system of Erlandson et al.

The mantle is observed over a much wider area than the cusp poleward of the auroral oval. [Newell and Meng, 1992] indicated a mantle some few degrees wide in MLAT (from single passes). Their probability of observing the mantle spans over a much wider interval in magnetic local time than the cusp, consistent with a wide (in local time) mantle current system.

[Newell et al., 1991a] sometimes also observed electron acceleration events within the mantle, which is associated with discrete aurora poleward of the oval and field aligned currents. [Murphree et al., 1990] presented Viking UV images of this mantle aurora poleward of the noon sector continuation of the normal diffuse auroral distribution from the afternoon sector (the traditional auroral oval). This mantle aurora was observed during northward IMF and appeared to be limited to negative IMF Bx and positive IMF By conditions. These auroral forms were often also found to exist in combination with polar arcs, and they expanded with typical speeds of 1 km/s east- or westwards and 0.3 km/s poleward. Furthermore, [Øieroset et al., 1997] found an inverse energy vs. latitude ion dispersion in the mantle from DMSP F11 particle observations during a period of northward IMF, consistent with sunward convection, see [Øieroset et al., 1997, Plate 1].

4.2.4 The CPS

The Central Plasma Sheet (CPS) is the region of hard precipitation (spectrally smooth clouds of > 1 keV electrons and ions) [Newell and Meng, 1992]. The CPS show two bands:

- The more intense band is extending from the morning side towards noon, primary due to keV electron precipitation, with some associated ion precipitation (sometimes at much lower energies).
- The other and less sharply defined band is extending from the dusk side towards noon. This mainly consists of energetic ion precipitation.

4.2.5 The BPS

The Boundary Plasma Sheet (BPS) is the region of diffuse and discrete aurora, as defined on the night-side of the Earth. The BPS lies poleward of the CPS and is characterized by more spatially and spectrally structured electron precipitation, [Newell et al., 1991b]. The electron and proton precipitation in the BPS is softer than in the CPS, but most discrete auroral arcs and electron acceleration events occur within this soft background dayside BPS electron precipitation. The ion precipitation shows no clear magnetosheath origin, and the electron temperatures are a few hundred eV. It is also possible that this region later will prove to have more than one source, [Newell et al., 1991b]. Newell et al. also found the BPS to correspond with the Region 2 current. Furthermore, from [Newell and Meng, 1992] the probability of observing BPS is much higher on the dusk side than the dawn side and is greatly reduced at noon.

4.2.6 Polar Rain

Polar rain occurs at the highest latitudes and was first identified by [Winningham and Heikkila, 1974] from particle observations from the Isis 1 satellite. They found *"a broad and structureless but rather weak flux of low-energy electrons"* with the maximum counting rate near 100 eV, which they called polar rain. The flux was isotropic, except within the up-going loss cone. The peak in the electron energy spectrum was detected at the same energy as within the cleft, suggesting the polar rain is of magnetosheath origin. The proton flux was generally too weak to be detected. This led Winningham and Heikkila to conclude *"although there may be an accompanying proton flux, it is even more attenuated than the electron flux from the values observed in the cleft"*.

Later, [Newell et al., 1991c] found polar rain to consist of fairly Maxwellian electrons with typical temperatures 60-110 eV (sometimes much higher) and with little or no ion accompaniment. Newell et al. identified the polar rain as comparatively unstructured, although large-scale polar cap gradients exists. According to [Newell and Meng, 1992] polar rain is observed 50% of the time above 80° MLAT and almost never below 75^{o} MLAT.

4.2.7 Void

Some cases are not easily fitted into any of the categories of [Newell and Meng, 1992; Newell and Meng, 1994]. This happens both at low and high latitudes. Several regions may be identified at the same local time/latitude at the same pass, or there may be void of significant particle fluxes (~ 0.01 ergs/cm^2 s). Therefore, Newell and Meng also had to establish a class containing these regions.

4.2.8 An Alternative Classification Scheme 1

[Kremser and Lundin, 1990] have presented an alternative way of classifying the dayside particle distribution. Their classification was based on observations of energetic particles in mid-altitude by the swedish Viking satellite during 146 crossings of the cusp/cleft. Visual inspection of all the spectrograms led Kremser and Lundin to divide the high-latitude dayside into the cleft, the "cusp", the "cusp proper" and the plasma mantle, see Figure 4.5 and Figure 4.6:

- The "cleft" is equatorward of the cusp. Here the magnetosheath ions are absent, while strong electron acceleration is dominating. This region is connected to the high-altitude LLBL.

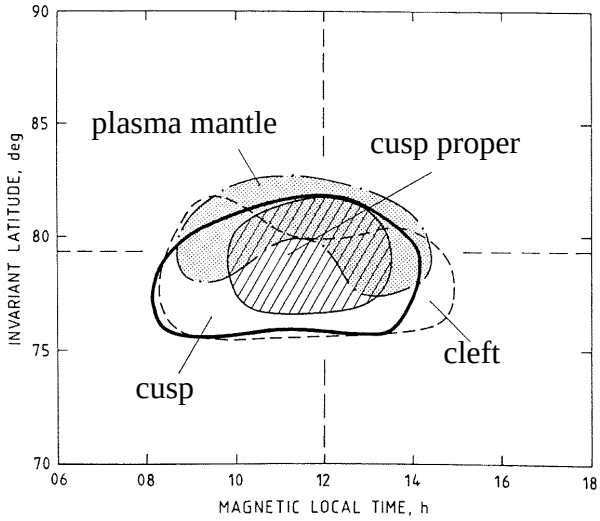

FIGURE 4.5 Schematic representation of the event distributions in the regions "cusp", "cusp proper", "cleft" and "plasma mantle", modified after [Kremser and Lundin, 1990].

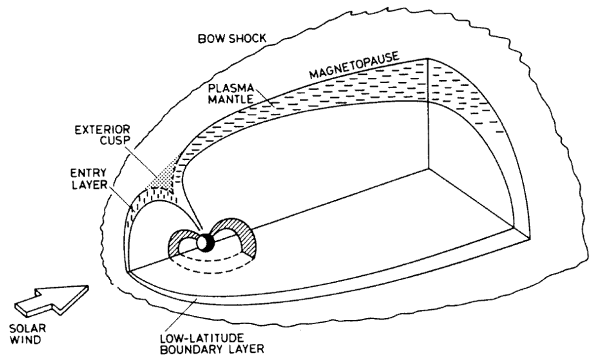

FIGURE 4.6 Schematic presentation of the magnetosphere and its boundary layers, [Lundin, 1987].

- The "cusp" (76-82˚ ILAT, 08-14 MLT) is characterized by magnetosheath particles and important electron acceleration signatures. The magnetosheath particles are thought to enter via the entry layer.
- The "cusp proper" (77-82˚ ILAT, 1000-1330 MLT) is a small region, within the cusp, containing of magnetosheath ions without electron acceleration. The cusp proper is connected to the exterior cusp.
- The plasma mantle is poleward of the cusp. Here the magnetosheath ions present, but the magnetosheath electrons are absent.

[Kremser and Lundin, 1990]'s "cusp proper" corresponds to the cusp of [Newell and Meng, 1992; Newell and Meng, 1994], while the "cusp" and "cleft" are matching Newell and Meng's LLBL.

4.2.9 An Alternative Classification Scheme 2

[Lockwood et al., 1996] have also presented an alternative classification scheme to the one used by [e.g. Newell and Meng, 1988]. Lockwood et al. used the time elapsed since reconnection $(t_s - t_0)$ to separate the regions, where t_s is the observation time at a satellite and t_o the time of reconnection. By assuming the length of a field line from the reconnection site to the ionosphere of $d=20R_e$ [Lockwood et al., 1996] classed the DMSP pass presented by [Newell et al., 1991a]:

- CPS when $(t_s - t_0) < 0$
- BPS or void when $0 < (t_s - t_0) < 120(s)$
- LLBL when $120 < (t_s - t_0) < 150(s)$
- cusp when $(t_s - t_0) > 150(s)$

[Lockwood et al., 1996] placed the open-closed field line boundary at $(t_s - t_0) \approx 50(s)$, giving the LLBL on open field lines.

4.2.10 Further Details

For further details on the dayside ionosphere, magnetosphere and the cusp/cleft region [Crooker and Burke, 1991; Smith and Lockwood, 1996; and references therein] are recommended.

4.3 The Optical Aurora

4.3.1 The Dayside Auroral Transients

One of the most discussed phenomena in the high-latitude dayside aurora, the last 10 years or so, is the moving auroral forms, the dayside auroral transients. [Sandholt et al., 1986] presented several examples, which they interpreted as the ionospheric signatures of FTE (Flux Transfer Events), transient and small-scale reconnection processes due to an increase in the merging rate. Later, [Newell and Sibeck, 1993] questioned this coupling of azimuthal flow bursts with an increased merging rate, showing how an abrupt not-transient increase in the IMF By component can introduce a faster flow east/west, or an abrupt decrease in IMF By can lead to an auroral transient moving poleward. Newell and Sibeck's model also predicts a larger class of transients, not just azimuthal flow bursts.

The auroral transients, also called midday auroral break-up, are frequently observed 09-15 MLT during periods of IMF Bz < 0, [Sandholt et al., 1989; Sandholt, 1990]. These transient optical arcs and channels of enhanced flow typically brighten near the equatorward boundary of the persistent 630 nm aurora and then move poleward. In the most intense cases, the 557 nm emissions may reach 10 to 20 kR. Other times the 630 nm is dominating at intensities of 5 to 10 kR, with the 557 nm less then 1 kR. A characteristic motion pattern with respect to the background arc is always observed [e.g. Sandholt et al., 1993; Moen et al., 1995]. Sandholt et al. also observed a northwestward motion into the polar cap of the auroral forms within 73^o to 78^o MLAT in the 08 to 10 MLT sector, near the zero-potential line separating the morning and postnoon convection cells, and approximately along the statistical plasma flow lines for that IMF orientation. An observed energy vs. latitude dispersion in the ions indicated that this region was within the plasma mantle. At the same time westward (tailward) moving auroral bright spots were observed at 71^o to 72^o MLAT (LLBL/BPS). These 557 nm luminosities were much more varying in intensity, frequently reaching 10 to 15 kR.

[Moen et al., 1995] studied eastward moving auroral forms in the postnoon sector and found good agreement with enhanced convection on both sides of noon. Moen et al. also found the background aurora (LLBL and/or BPS) located on predominately sunward convecting field lines. 557.7 nm aurora was indicating that the Region 1 current is distributed within the background aurora. The moving auroral forms were found to coincide with magnetosheath-like particle precipitation (from DMSP F10 particle observations and 630.0 nm emissions), as they moved eastward with approximately the local convection velocity. A secondary population of energetic ions introduced uncertainty whether the moving auroral forms were associated with open flux tubes, magnetopause reconnection and bursty ionospheric ion flow events.

4.3.2 Auroral Classification

These first investigations of the moving auroral forms were the initial step in a process of classifying the dayside aurora. Later, [Sandholt et al., 1996b; Sandholt et al., 1996a; Øieroset et al., 1997] have divided the cusp aurora into two main types; Type 1 (south) and Type 2 (north), and recently [Sandholt et al., 1998] have presented a brief review of the classification of the dayside aurora. A summary is given in Figure 4.7:

1. Type 1 aurora is rayed bands, dominated by the red line emission and is typically much stronger than the Type 2 aurora. Furthermore, Type 1 aurora is located at much

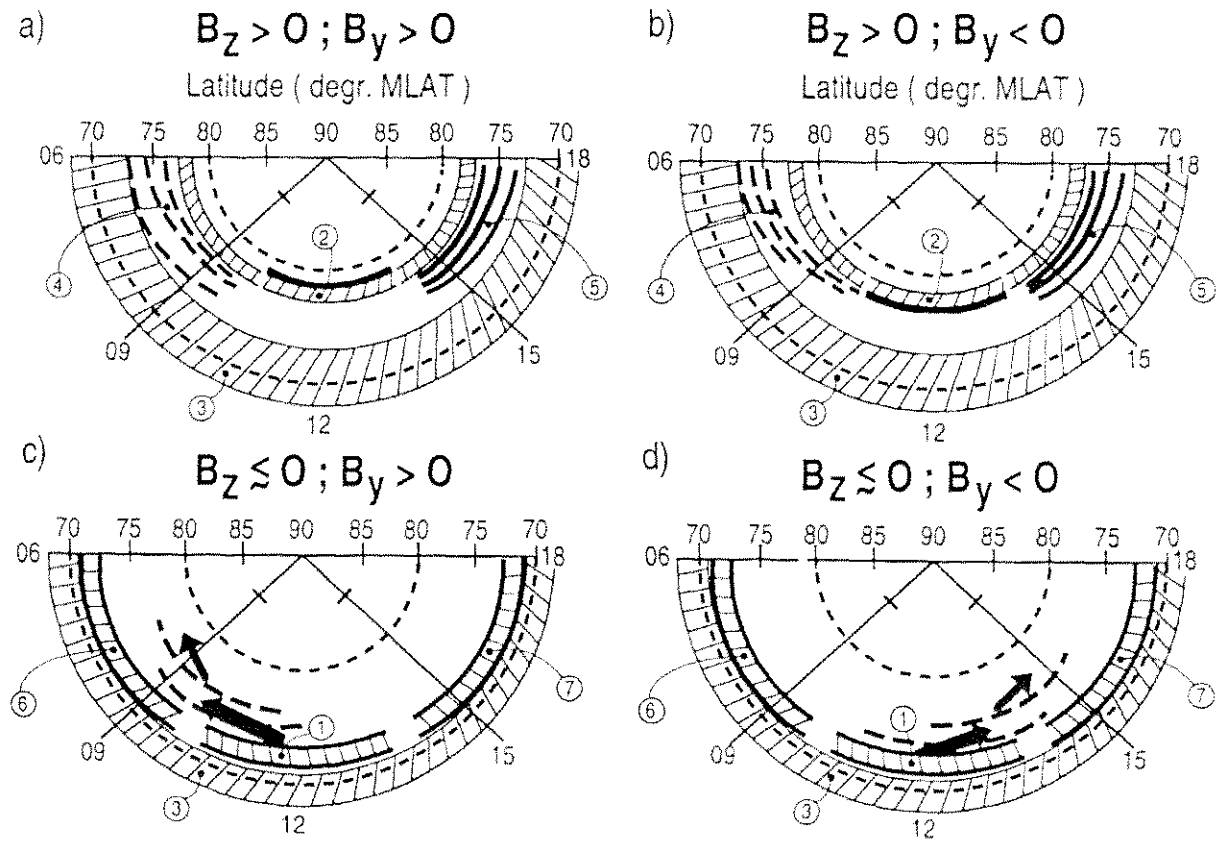

FIGURE 4.7 Schematic overview of dayside auroral forms for different IMF orientations, from [Sandholt et al., 1998].

lower latitudes (~ 72-74° MLAT). This group is also associated with the appearance of quasi-periodic (T~5min.) sequences of auroral forms which brighten at the equatorward boundary of the pre-existing Type 1 and subsequently propagate poleward. During IMF By > 0 (By < 0) these forms typically brighten close to or slightly postnoon (prenoon) and propagate northwest (northeast) and fade out in the prenoon (postnoon) sector at ~ 75-77° MLAT, respectively.

2. Type 2 is a rather homogeneous aurora generally consisting of higher red line intensities. This group only exists during IMF Bz > 0. The longitudinal extensions in the pre- and postnoon sectors are called Type 2. Type 2 is the midday gap aurora.
3. Type 3 is diffuse green line aurora caused by the precipitation of electrons from the dayside extension of the plasma sheet. This most equatorward form can in principle stretch all around noon from dawn to dusk, but the local time extent varies from case to case.
4. Type 4 is situated at ~ 73-78° MLAT (poleward of Type 3) in the prenoon (06-09 MLT) sector only during IMF Bz > 0. This aurora consists of multiple, discrete forms and is inhomogenous in the east-west direction.
5. Type 5 is situated at ~ 73-78 MLAT (poleward of Type 3) in the postnoon (06-09 MLT) sector only during IMF

Bz > 0. This aurora consists of multiple, discrete arcs of relatively strong emissions (~ 1-10 kR) in both the green and red lines.

6. Type 6 is located in the prenoon sector and often appear as a longitudinal extension of the Type 1 aurora, but the green line intensities are higher away from noon.
7. Type 7 is located i the postnoon sector and often also appear as a longitudinal extension of the Type 1 aurora, but the green line intensities are higher here too.

- An extra discrete form is observed in the midday sector (09-15 MLT). This form of enhanced green line intensity (~ 1kR stronger than Type 2) is observed at the poleward (equatorward) boundary of Type 2 when IMF By > 0 (By < 0).

The Type 1 aurora occurs during southward IMF, and the Type 2 when IMF is strongly northward. A third case combining these two exists when the IMF is weakly northward, when there may be both Type 1 in south and Type 2 in north. [Sandholt et al., 1997] encountered all these three combinations January 12 1997 during IMF By < 0 conditions.

Type 1 aurora is believed to be related to reconnection at low magnetopause latitudes. The Type 2 aurora is instead thought to be associated with "lobe reconnection" between geomagnetic and interplanetary magnetic field lines at high magnetopause latitudes (tailward of the cusp) during periods of northward IMF, [Øieroset et al., 1997; Sandholt et al., 1996a; and references therein]. From groundbased magnetometers, optics and interplanetary data from IMP-8 Sandholt et al. found a low magnetic shear at the frontside magnetopause to correspond with the Type 2 aurora including a sunward convection in the dayside polar cap. Conversely, during periods of larger magnetic shear the Type 1 aurora and an antisunward flow was observed instead.

[Sandholt et al., 1996a] also reported two examples of sharp transitions in the dayside 630.0 nm aurora between Type 1 and Type 2 aurora in response to a switch between large negative and large positive IMF Bz components, respectively. The Type 2 aurora was found to last for several tens of minutes indicating "lobe reconnection" to be a quasi-steady process. A statistical study by [Øieroset et al., 1997] has also revealed the existence of Type 2 aurora in the northern hemisphere for both IMF Bx polarities, where the 557 nm line showed an enhanced intensity mainly during Bx < 0.

4.4 Models

A process is not completely known before all its aspects can be described by a model, and this model should also describe and explain new data. To better understand the processes taking place good models are crucial, and now some useful models will be presented.

4.4.1 Plasma Transport on Open Magnetic Field Lines

[Onsager et al., 1993] modelled the plasma transport in the open magnetic field region of the dayside magnetosphere to investigate the source regions and the distribution of solar wind plasma in the cusp and mantle. They included a variation in the magnetosheath properties as the plasma accelerates away from the subsolar point, a variation in the transport of magnetosheath plasma across the magnetopause as the orientation of a field line changes after reconnection, and the transport of the magnetosheath plasma within the magnetosphere. A comparison of the results for a set of given solar wind parameters showed good

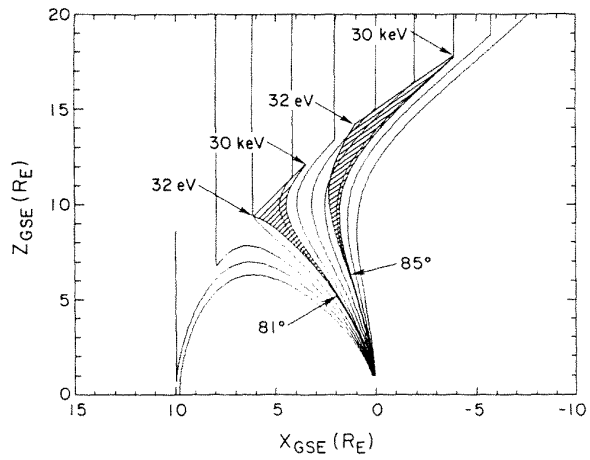

FIGURE 4.8 Noon-midnight meridian magnetic field. The shaded regions indicate where 32 eV to 30 keV protons detected by a satellite at 81° and 85° latitude cross the magneto- pause, from [Onsager et al., 1993].

agreement with DMSP low-altitude particle data from [Newell et al., 1991a]. However the model did not return the fine structure in the data.

[Onsager et al., 1993]'s model also very well displayed the velocity filter (ExB-drift) effect and how particles at different energies, observed in low-altitude by a satellite at a given latitude, originate from completely different source regions in the magnetosheath, see Figure 4.8. Here it is seen how (at a given latitude) the lowest energy particles originate closer to the reconnection point than the higher energy ones.

4.4.2 Open Field Line Model of the LLBL Near Noon

[Lyons et al., 1994] investigated whether several characteristics observed in the LLBL and cusp region could be accounted for in an open field line model. Using a magnetic field model including a penetrating uniform 1 nT IMF Lyons et al. defined the LLBL to be the open portion of the magnetosphere equatorward or sunward of the cusp bifurcation line. In their model the open-closed field line boundary was simply the inner or equatorward boundary of the LLBL. Their cusp was poleward (antisunward) of the cusp bifurcation line.

Several of their results was in good agreement with published observations:

- *Magnetosheath particles*
  1. abruptly decrease in intensity at the inner (equatorward) LLBL boundary at high (low) altitudes
  2. appear as one continuous region across the LLBL/cusp boundary.
- *Energetic magnetospheric electrons*
  1. abruptly decrease in intensity at equatorward boundary of LLBL
  2. show trapped pitch angle distributions within LLBL
  3. abruptly decrease to background intensity across the LLBL/cusp boundary.
- *Energetic magnetospheric protons*
  1. often have fluxes continuous across equatorward boundary of LLBL
  2. have isotropic pitch angle distributions within and equatorward of LLBL
  3. abruptly decrease to background intensity across LLBL/cusp boundary.
- *Poleward boundary of LLBL/equatorward boundary of cusp*
  1. has no significant interhemispherical difference dependent upon IMF Bx
  2. shifts equatorward with increasingly negative IMF Bz
  3. has variations and interhemispherical differences dependent upon dipole tilt.

Some results was not currently testable with published observations:

- *Width of LLBL at low altitudes* varies with IMF direction and has interhemispherical differences dependent upon IMF Bx.
- *LLBL region at high altitudes*
  1. has width dependent upon IMF direction
  2. contains narrow region of detached field lines for strongly northward IMF.

Based on these results [Lyons et al., 1994] proposed the LLBL could be explained in an open field line model near noon.

Now, some of the basic characteristics of the dayside aurora have been presented. In the next chapter several examples will be presented and put into this context using this established framework.

Chapter 5

January 12 1997
- Event Studies

First, a short overview of the solar wind parameters and groundbased optical data, before further discussion of five NOAA-12 passes over Svalbard

5.1 Selecting the Events

Having presented an overview of the NOAA-12 particle data and the solar wind conditions from January 9 to 12, 1997, it is appropriate to look for corresponding groundbased optical measurements to compare with. At the Auroral Station in Longyearbyen the instruments were running most of the actual period. However, cloudy weather conditions the first three days and the fact that the aurora moved far equatorward, out of the field-of-view on January 10, leaves only January 12 as the appropriate day for such comparative studies.

First, a comprehensive overview of the interplanetary data and the groundbased data will be given. Then a detailed comparison between these data and some NOAA-12 passes will be presented. Finally, some images of the X-ray aurora from the PIXIE camera on board the Polar satellite will be shown to illustrate the lack of severe fluxes of energetic electrons in the cusp/cleft region.

5.2 Solar Wind Conditions

Proved to be important magnetospheric input parameters is the solar wind conditions. Therefore, when discussing ionospheric particle data and groundbased optical data, the corresponding solar wind parameters should be taken into account. The Wind spacecraft, presented in Section 2.3 on page 23, carries suitable instrumentation for such measurements.

5.2.1 January 12, 1997

In Figure 5.1 the January 12 1997, 06:00 to 16:00 UT segment of the solar wind parameters, previously presented in Figure 3.3 on page 27, is shown. The interplanetary magnetic field (IMF), the IMF clock angle, the electron & ion densities, ion & electron temperature, thermal velocity and the flow velocity is displayed. The IMF clock angle was defined in Equation 3.1 in Section 3.2.2 on page 28. In the actual period Wind moved from $\{X_{GSE} = 102, Y_{GSE} = -54, Z_{GSE} = -5\}$ to {105, -53, -6}.

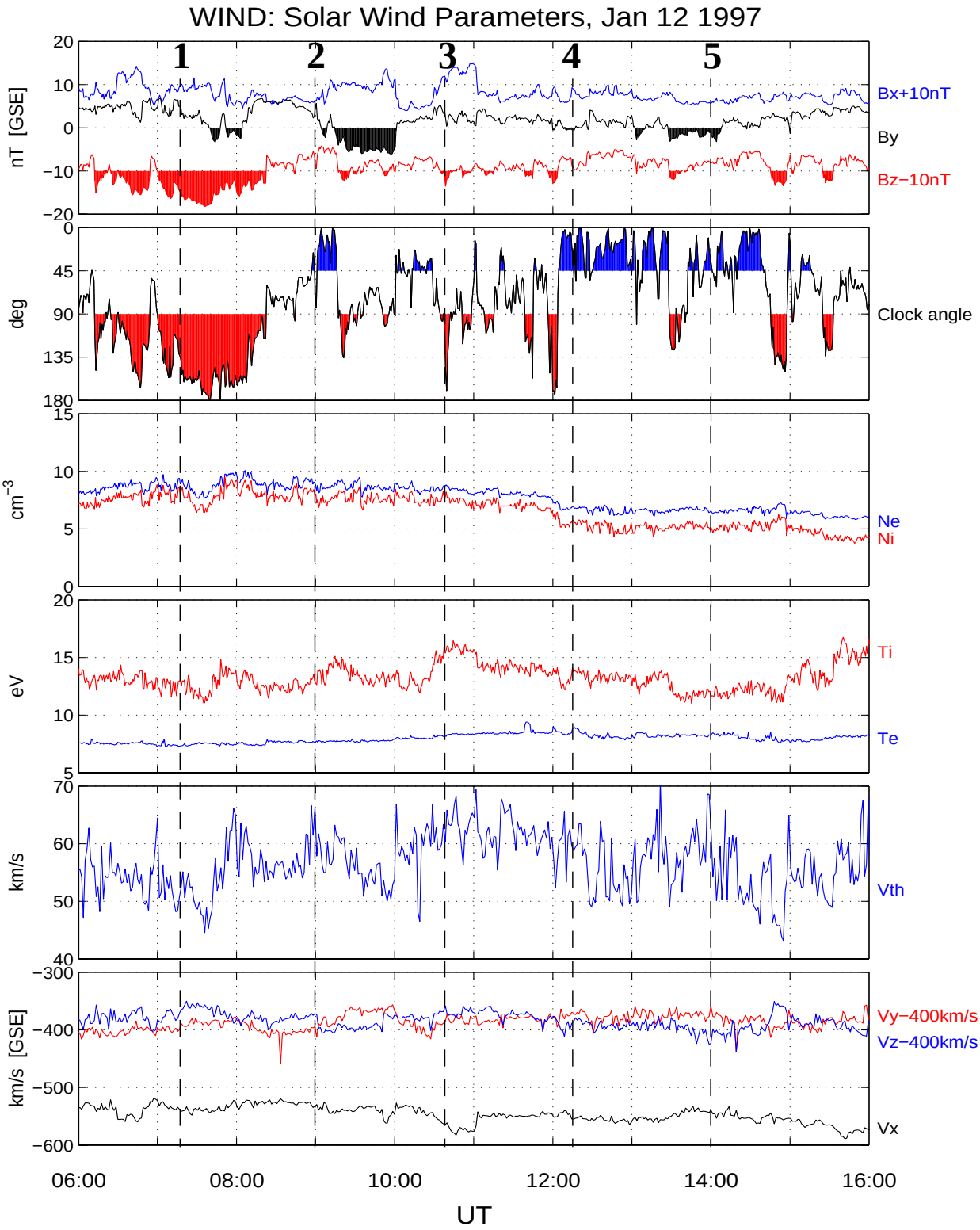

FIGURE 5.1 Solar wind parameters from the Wind spacecraft 06:00-16:00 UT on January 12 1997. This figure is an expanded part of Figure 3.3 on page 27. The guide lines **1**, **2**, **3**, **4** and **5** correspond to the five NOAA-12 passes discussed in Section 5.6, for a 25 min. time delay.

The first aspect to notice is how the solar wind conditions have stabilized on January 12, from the more disturbed conditions the previous days, cf. Chapter 3. The IMF has returned to pre-storm values, and the densities are back to normal values. However, the temperatures and the thermal and flow velocities are still larger than typical. This is best seen in the flow velocity X_{GSE} -component, which is between -600 km/s and -500 km/s GSE.

After a brief northward interval, the IMF turned southward at 07:00 UT and stayed negative until 08:22 UT. Then, the IMF returned northward and stayed so until 09:18 UT. During the rest of the period, the IMF was mostly northward with only shorter (~5-10 min.) southward turning events. The IMF By component was mostly positive, but had three major negative sequences. The strongest one was from 09:15 to 10:01 UT.

5.2.2 The Wind-Ionosphere Time Delay

The ionospheric response of an abrupt change in the IMF conditions observed at the Wind spacecraft is not seen at once at the Earth. The solar wind needs some time to travel from Wind to the polar ionosphere, and the ionosphere also needs some time to react, as discussed in Section 3.2.3 and Section 3.2.4. The time delay was estimated to be ~ 25 min. plus the ionospheric response time, using a modified version of a formula presented by [Lockwood et al., 1989]. The results of this calculation using Equation 3.6 on page 30 and the solar wind parameters January 12 1997 at 06:00-16:00 UT were shown in Figure 3.9 on page 32. This time delay was in good agreement with that reported by [Sandholt et al., 1997]. Their estimate gave a 25 min. propagation delay, while their observations (09:30-1030 UT on January 12) occurred ~ 28 min. after a strong southward rotation of the IMF at Wind.

In the following discussion a 25 min. time delay is used to find the matching solar wind - ionospheric conditions. In fact, in Figure 5.1 this time delay has been applied to find the matching Wind observations to five NOAA-12 passes discussed later in Section 5.6.

5.3 The AE Index

Groundbased magnetic indices are very useful as indicators of the geomagnetic activity, the auroral substorm activity. Figure 5.2 shows the Auroral Electrojet (AE) index on January 12 1997, based on mostly 8 stations* in the auroral zone. The corresponding AU, AL, and AO indices are also displayed. The events **1**, **2**, **3**, **4** and **5**, related to the five NOAA-12 passes to be studied in Section 5.6, are also indicated.

From these Kyoto Quick Look AE and AL indices a geomagnetic substorm started around 07:30 UT. This activity later had three major intensifications and reached its maximum around 08:20 UT. Afterwards the activity slowly decreased. Later, from 16:00 to around 21:00 UT, some activity is also seen.

The first NOAA-12 event takes place some 15 min. after the first activation, while the second one is late in the recovery phase of the substorm. The three other events occurred during low activity.

* Except a couple very short intervals where only 7 stations were used.

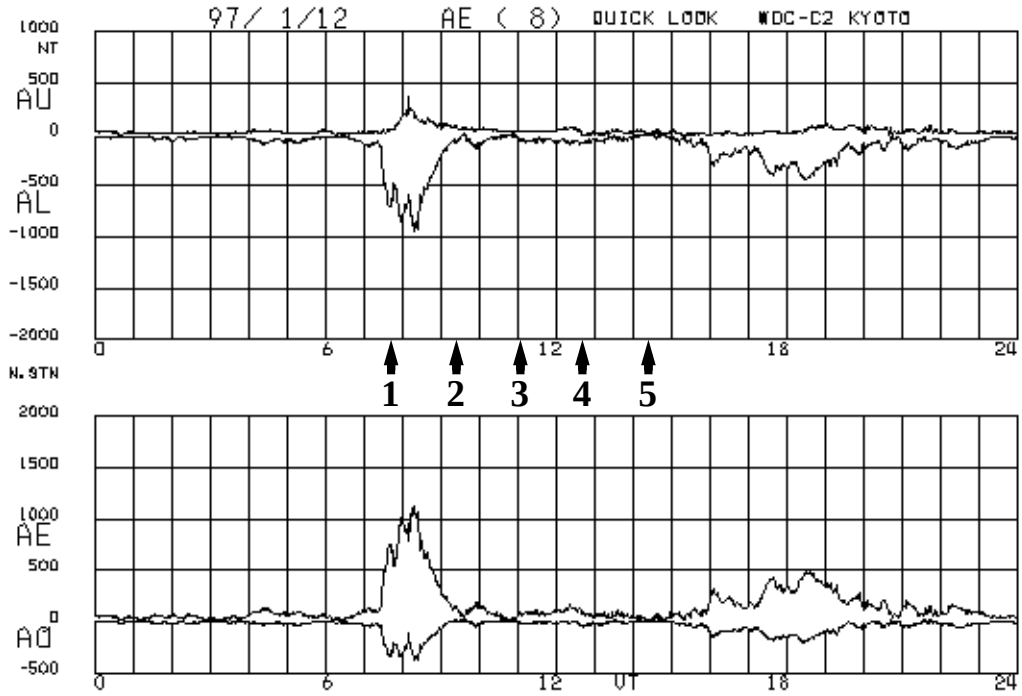

FIGURE 5.2 The Auroral Electrojet indices (8) on January 12 1997. The events **1**, **2**, **3**, **4** and **5** correspond to the five NOAA-12 passes discussed in Section 5.6.

5.4 The Meridian Scanning Photometer

The Meridian Scanning Photometer (MSP), scanning the sky from north to south, gives a lot of useful information. The north/south positioning of the aurora along the local magnetic meridian is viewed in several narrow wavelength intervals. This makes it easy to compare the intensities between the different wavelengths, and the north/south motion of auroral borders at the meridian are clearly obtained. An advantage of the MSP is also its way of summarizing the auroral activity during a day. By plotting each scan using either a colour table or stack plots, the time development of the aurora along the line-of-sight is easily seen. Each method have both its advantages and disadvantages; colour plots summarize the observations best, while stack plots display the absolute intensity of each MSP scan better.

On January 12 two MSPs were running at Svalbard. In Longyearbyen at the Auroral Station (78˚ 12’ 09’’ N, 15˚ 49’ 45’’ E)† a MSP was observing at four wavelengths: 630.0 nm (O_I), 427.8 nm (N_2^+), 557.7 nm (O_I) and 486.1 nm (H_β). In Ny Ålesund (78.9˚ N, 11.9˚ E)‡ another MSP was operating at 630.0 nm and 557.7 nm.

First, an overview of the MSP data from the Auroral Station at 00:00 to 15:00 UT on January 12 1997 is shown in Figure 5.3. A very

† Measured with a portable GPS January 29 1998.

‡ From [Moen et al., 1996].

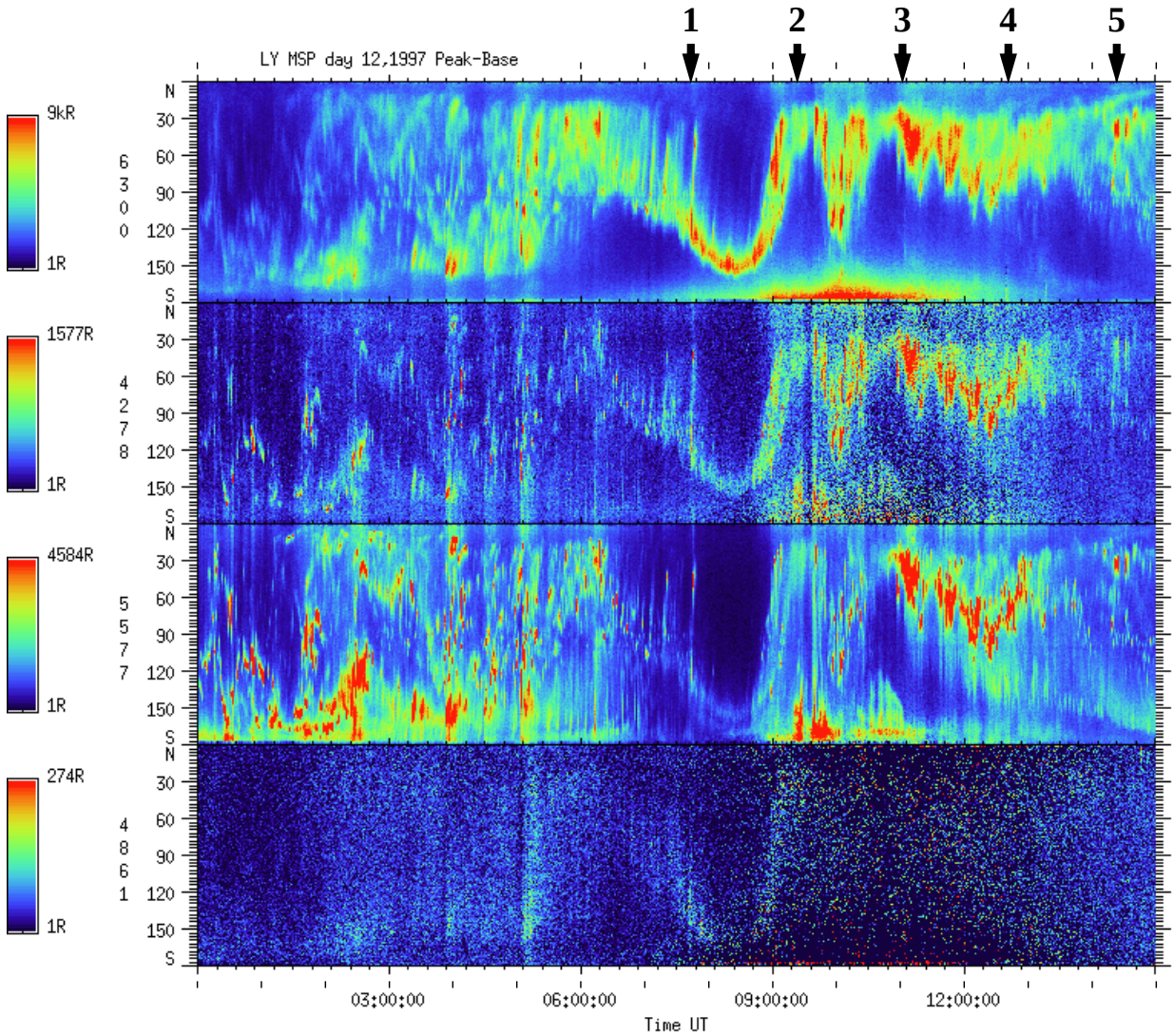

FIGURE 5.3 Meridian Scanning Photometer intensities (630.0 nm, 427.8 nm, 557.7 nm & 486.1 nm) from the Auroral Station in Longyearbyen, 00:00 to 15:00 UT on January 12 1997. The events **1**, **2**, **3**, **4** & **5** correspond to the five NOAA-12 passes discussed in Section 5.6.

clear zenith, via south to north motion of the aurora is seen in all wavelengths from 07:30 to 09:00 UT. The ASC images from Longyearbyen (to be presented in Figure 5.12 and Figure 5.13) reveal that this is a real north/south motion of the whole auroral arc, and not any artificial effects caused by an east-west propagation of forms of latitudinal structure through the MSP field-of-view.

5.4.1 Finding the Altitude of the Auroral Emissions

When comparing groundbased optical observations from several stations, it is in some cases possible to find the altitude of the emissions. A precise altitude assumption is also necessary when transforming an auroral picture from elevation and azimuth angles to equivalent latitudes and longitudes.

The first studies to determine the altitudes of the auroral emissions were carried out using photos of the aurora. Strong auroral structures and their relative location on the background sky were visually identified in simultaneous exposed images from several points on the ground, and the auroral heights could be calculated, see e.g. [Störmer, 1955]. Figure 5.4 presents the variation in intensity vs. altitude of some of the most typical auroral emission lines, from [Carlson Jr. and Egeland, 1995]. The 630.0 nm emission line shows a wide maximum in intensity at about 250 km altitude. The 557.7 nm line displays the maximum at about 170 km altitude on the dayside and about 120 km on the nightside. The 427.8 nm line more or less follows the 557.7 nm line.

The 557 nm and 630 nm MSP channels from Longyearbyen and Ny Ålesund may also be used in a fast check of the altitude of the emissions. The Ny Ålesund data set is processed as it is (for elevations from 10-165˚ above the northern horizon), while in the Longyearbyen MSP data set only the elevations > 15˚ above the horizon are used. For each wavelength and station the elevation with the maximum intensity (in kR) of each scan is recorded[**]. Assuming the emissions to come from a very thin layer at a given height, the corresponding magnetic latitude may be calculated. The transformation is described in Appendix B. The height is stepped from 50-200 km (557.7 nm) and 100-500 km (630.0 nm) in 10 km steps[††]. The magnetic latitude (where the elevation crosses the emission layer) of each altitude is calculated for each station and altitude. Figure B.1 on page 121 may be used as an illustration of the procedure. The elevation θ is kept constant while the height *h* is varied and the magnetic latitude Λ_{eq} from Equation B.13 is calculated for each *h*. Based on the two stations, the altitude which gives the smallest difference in magnetic latitude, is chosen as the 'correct' height of the emissions. This procedure is then repeated for the next scan.

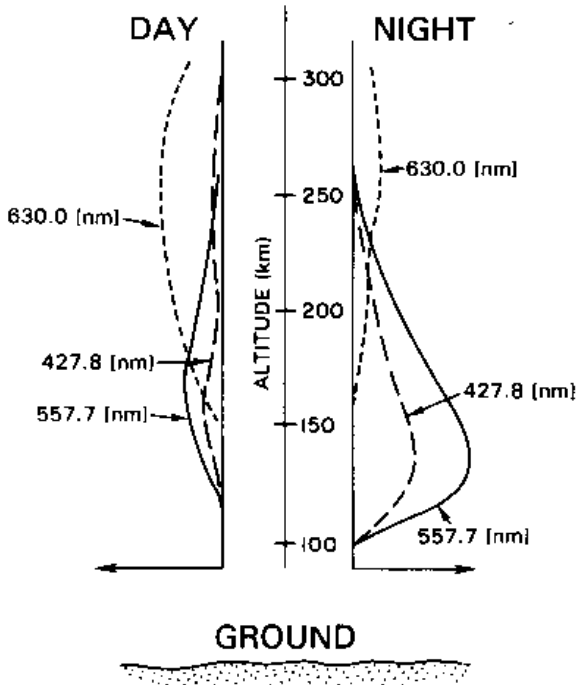

FIGURE 5.4 The relationship between the intensities of the most typical auroral emission lines vs. altitude, from [Carlson Jr. and Egeland, 1995]

The resulting altitudes change rather much from scan to scan (especially the 557.7 nm band), so to better see the overall picture these values are run though a low-pass filter. In this way the noise is eliminated, while the overall shape is reproduced. Figure 5.5 shows the

[**] In fact, the Ny Ålesund intensities have to be interpolated to get the same time as in the Longyearbyen recordings.

[††] The altitude ranges were by purpose chosen this wide to include both realistic and unrealistic altitudes. If an unrealistic altitude of the emissions is found, some of the assumptions in our method have broken down.

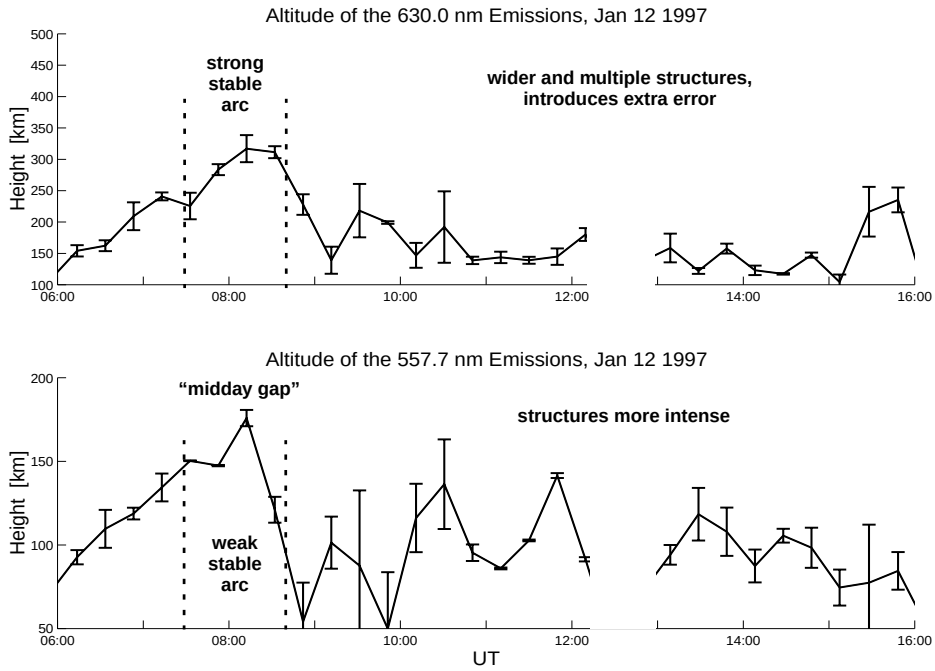

FIGURE 5.5 The calculated altitude of the 557.7 nm and 630.0 nm emissions, based on the elevations of maximum intensity from the Longyearbyen and Ny Ålesund MSPs on January 12 1997. In order to remove the noise in the single scans, each data point is a ~ 15 min. average. The error bars indicate the interval to the second largest maximum in the intensity, an estimate of the uncertainty of this method.
Some of these altitudes are not realistic. E.g. for the 557.7 nm line an altitude <100 km seems improbable. Inspection of the MSP stack plots (Figure 5.9 and Figure 5.10) reveals that these low altitudes are found to correspond with the times when multiple or wide arcs are within the field-of-view; e.g. around 09:00 and 10:00 UT where both Type 1 & Type 2 aurora is present. (This demonstrates a weakness of the method, where the assumptions break down.)

height vs. time when the data set is run through a ~ 15 min. low-pass filter, when all the scans from 06:00 to 16:00 UT on January 12 1997 have been used.

The error bars in Figure 5.5 are established in the following way. While the 'correct' height was found from the elevation of the maximum intensity, the elevation of the second largest intensity may be used as an estimate of the uncertainty in the method. This elevation is then run through the same procedure, and the difference 'correct' minus 'second best' gives an estimate of the width of the error interval.

This fast and automatic method also implicitly assumes the maximum intensity observed at each station is the same auroral structure. This assumption quickly breaks down if the intensities are very low, if several bright structures (e.g. double arcs) are within the field-of-view, or if a structure looks brighter from the side than from straight below.

In Figure 5.5 the 630.0 nm emissions indicate the maximum intensity in about ~ 200-350 km altitude at 07-09 UT. The 557.7 nm emissions display the maximum intensity in about ~ 100-180 km height, mostly below 150 km, in the same interval. During this

time the magnetic local time of Longyearbyen and Ny Ålesund went from 10:15 to 12:15 MLT. Simultaneous, the 630.0 nm line was very bright and shifted equatorward. Therefore, double arcs are no trouble here and the obtained altitude is reliable for the 630.0 nm. In the 557.7 nm the intensity is generally much weaker and the structures more discrete, with shorter periods of strong intensifications. The maximum altitude just after 08:00 UT occurred during an interval when the 557.7 nm emissions almost moved out of the field-of-view (equatorward). Consequently, some extra uncertainty is associated with this event.

Later, from 09:00-12:00 UT the 630.0 nm is very disturbed by the sun-glow in the southern horizon. (The sun was below the horizon.) The 557.7 nm however was less disturbed, but partly absent 557.7 nm emissions in this interval introduce an extra error. Any altitude determination of the 557.7 nm emissions to be below 100 km is clearly unrealistic, indicating the assumptions for our method not to be satisfied. In the period ~ 12:00-13:00 UT the Ny Ålesund MSP was turned off, therefore the data gap.

Thus, an assumed 120 km altitude for the 557.7 nm does not seem too unreasonable as an average of the whole period 06:00-16:00 UT. This is in acceptable agreement with the results of [Carlson Jr. and Egeland, 1995] in Figure 5.4. Keeping in mind the uncertainties of the method, assuming a 250 km altitude of the 630.0 nm emissions is also in tolerable correspondence with Figure 5.4 and Figure 5.5, although at 08:00 UT ~ 300 km seems more correct, and after about 09:00 UT the altitude of the 630.0 nm line is observed to fall below 200 km. The latter is partly caused by the existence of wider and multiple structures within the field-of-view. In this way the maximum intensity recorded at the two stations may not correspond to the same point in the ionosphere, which introduces an extra error.

Nevertheless, if the two guessed altitudes were very wrong, the two pictures obtained later (Figure 5.6 and Figure 5.7) from Ny Ålesund and Longyearbyen should diverge. This is not the case.

This method presents an alternative and more automatic way to decide the altitude of auroral emissions, when the maximum intensity of a MSP scan is easily obtained from two stations. However, the uncertainties in the assumptions needs to be investigated further, especially when multiple or wide arcs are within the field-of-view. And, a direct comparison with the traditional method of first identifying a structure manually from the two sites and then calculate the height is important. But, that is well without the scope of this thesis and is left for future work.

5.4.2 A New Way of Using MSP Data

Previously the MSP data has frequently been displayed using waterfalls, stack or colour plots as a function of time and elevation angle only. In this way the magnetic local time and magnetic latitude variations is lost (or at least not straight forward to see for the less experienced reader).

One day of Meridian Scanning Photometer data represents a scan through all magnetic local times in the ionosphere, as the Earth is continuously rotating. Therefore, by assuming a constant altitude of the optical emissions (for simplicity) and by plotting the MSP intensities vs. magnetic local time and magnetic latitude, a global map of the aurora, where the period of scanning is 24 hours, is obtained.

Our choice to use a constant emission altitude needs to be commented on. From Figure 5.4 this altitude is obviously different at day and night, especially for the 557.7 nm and 427.8 nm lines. This discrepancy is partly due to a different ionospheric configuration (in the F-layer) and the much more energetic particle precipitation in the nightside. These energized particles thus precipitate to a lower altitudes. However, since we here focus on the dayside aurora, by choosing typical dayside altitudes this point is not critical for the conclusions. The projection in the night side must nevertheless be treated with more caution.

In order to perform a transformation from MSP elevation angles to the magnetic latitudes, one must make two assumptions:

1. The altitude of the emissions
2. The emissions must be a thin layer

If these two assumptions are fulfilled the transformation is straight forward. However, two questions must be answered; which altitude should be used, and how goes the transformation?

The first question was partly answered in the last section, Section 5.4.1; 630.0 nm at 250 km altitude and 557.7 nm at 120 km. According to Figure 5.4 the 427.8 nm display a similar pattern to 557.7 nm, so 120 km is assumed here too. The 486.1 nm emissions are worse; no curve is presented. Thus, we just assume a 120 km altitude. However, the 486.1 nm intensities are very low, and this assumption is therefore not causing any difficulties.

The second question is solved by using the technique developed in Appendix B. The geometry is shown in Figure B.1 on page 121. Through several trigonometric transformations an expression for the equivalent magnetic latitude Λ_{eq} of an elevation angle θ is achieved, given the magnetic latitude of the station, the Earth's radius and the assumed altitude of the optical emissions.

Now, the two questions are solved and Figure 5.6, Figure 5.7 and Figure 5.8 are obtained. The MSP intensities is plotted in the centre of the plot using a colour scale, surrounded by the IMF clock angle in red, blue and black. The IMF clock angle was defined in Equation 3.1 on page 28 and is computed from the Wind IMF By and Bz components. Red colour indicates IMF clock angles 90 to 180˚, CAR 3, (southward IMF) associated with strongly reconnection at the magnetopause at lower latitudes giving an expansion of the polar cap and equatorward motion of the auroral oval. Blue colour shows IMF clock angles from 0 to 45˚, CAR 1, (strongly northward IMF clock angle) related to compression of the polar cap and poleward motion of the auroral oval. The outer red dotted circle denotes a clock angle of 180˚ and the inner blue dotted circle is 0˚. The 25 min. time delay for the IMF to propagate from Wind to the noon cleft ionosphere is taken into account. Thereby, the clock angle and the UT scale are rotated 6˚ in the counterclockwise direction. However, the extra ionospheric response time has not been included.

The MSP intensities is displayed, as a function of the calculated CGMLAT, onto a double grid. The outer one is the MLT and the inner one is the UT. Assuming the time distance between the local MLT of a station and the UT is constant during a day, the MLT grid is found using both the UT and the magnetic midnight of Longyearbyen (20:44 UT) and Ny Ålesund (20:48 UT). The UT grid shows when the MSP was scanning in that MLT region, and is also used to plot the IMF clock angle, which is of course independent of the MLT grid.

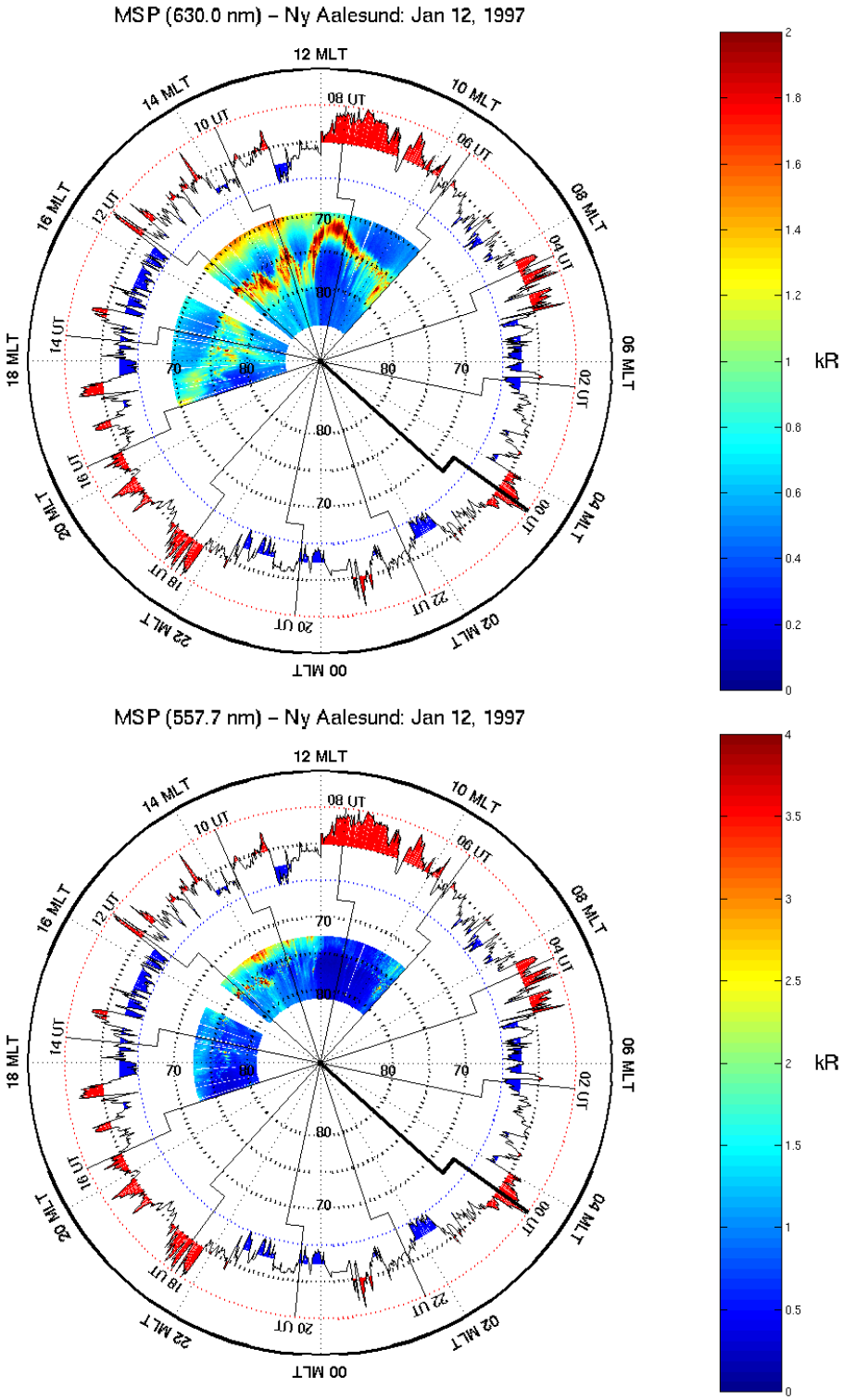

FIGURE 5.6 Meridian Scanning Photometer (630 nm & 557 nm) from Ny Ålesund and IMF clock angle from Wind, January 12 1997 plotted onto a MLT/CGMLAT grid. The outer UT scale and clock angle is rotated 6˚ counterclockwise (i.e. a 25 min. time delay), the inner MSP plot is not rotated. E.g. the thick solid line show 00 UT in the ionosphere and 00 UT at Wind.

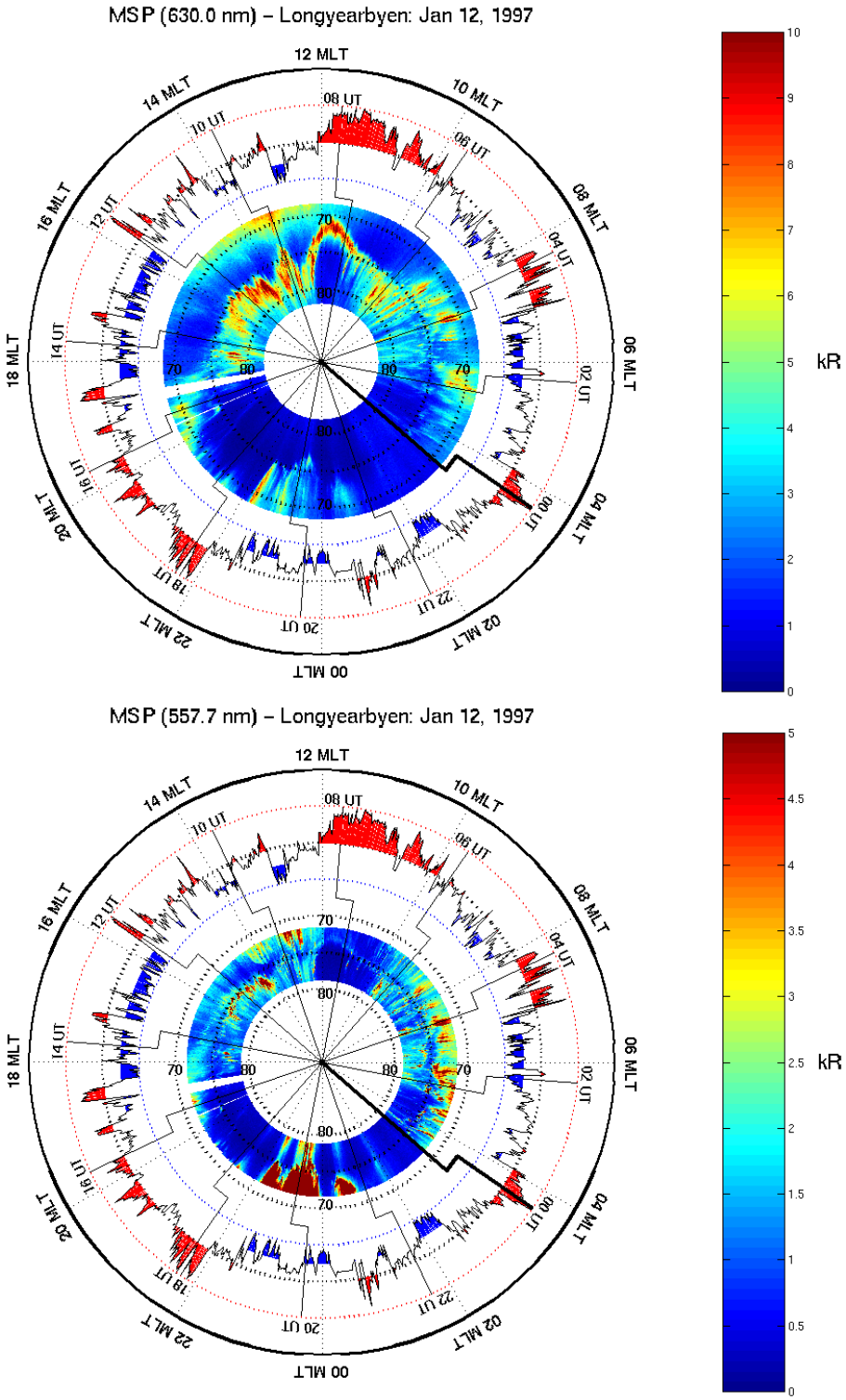

FIGURE 5.7 Meridian Scanning Photometer (630 nm & 557 nm) from Longyearbyen and IMF clock angle from Wind, January 12 1997 plotted onto a MLT/CGMLAT grid, the same grid as in Figure 5.6.

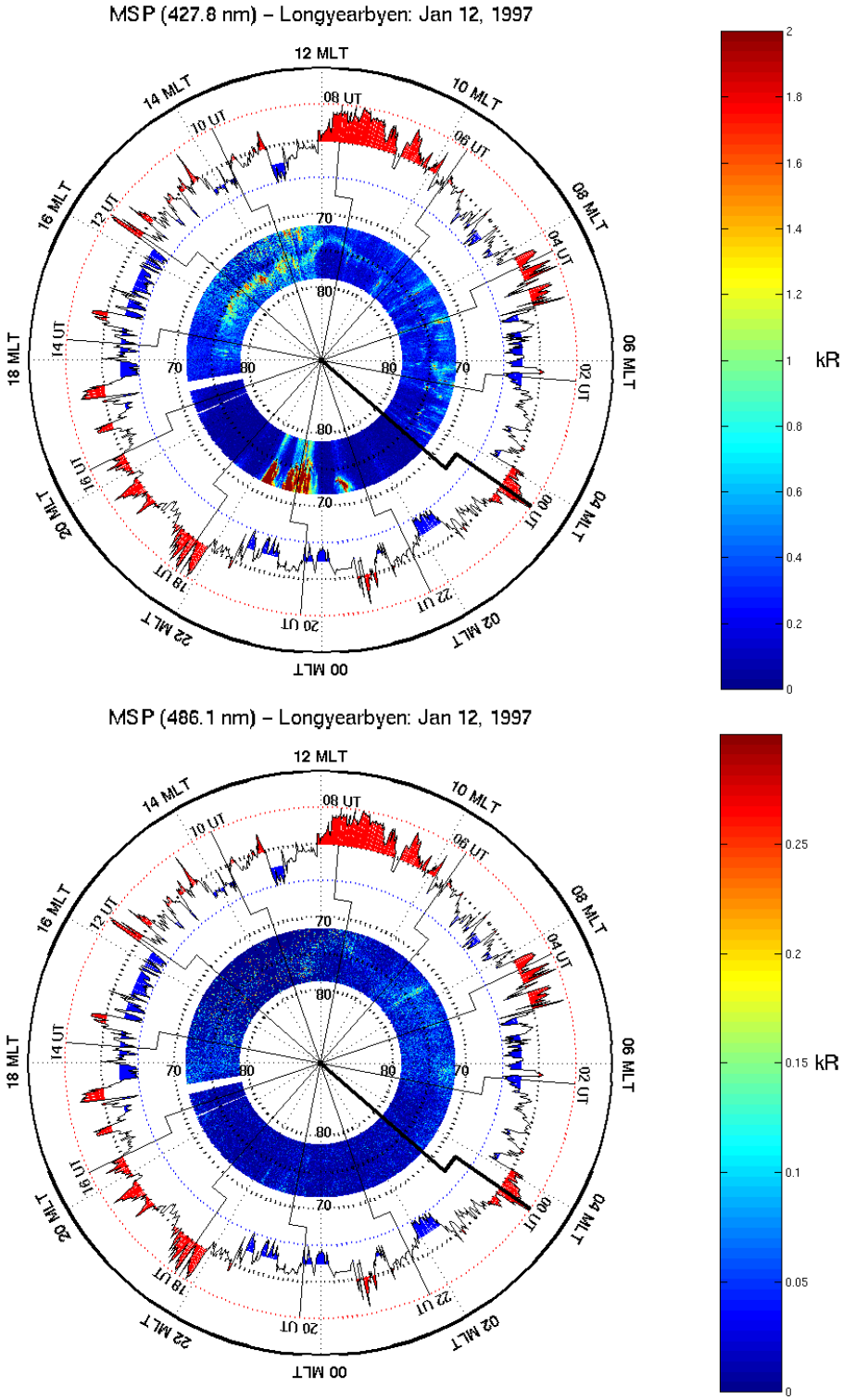

FIGURE 5.8 Meridian Scanning Photometer (427 nm & 486 nm) from Longyearbyen and IMF clock angle from Wind, January 12 1997 plotted onto a MLT/CGMLAT grid, the same grid as in Figure 5.6.

Figure 5.6 shows the 630.0 nm and 557.7 nm MSP intensities from Ny Ålesund, 06-16 UT January 12 1997, the time interval of NOAA-12 passes near Svalbard. The reason for not plotting the rest of the day is not that the data do not exist, but rather that we concentrate on data from this period. Both the 630 nm and 557 nm emissions shown here is for all elevations between 10˚ to 165˚ from the northern horizon.

Just before 07:30 UT (~1045 MLT) a very clear equatorward motion of the 630.0 nm arc is seen as a response of the clock angle being strongly southward for some time. The poleward turning just after 12 MLT agrees very well with a northward rotation of the IMF. No 557 nm in this area suggest the region shown is only consisting of high fluxes of soft particle precipitation, the cusp. It is seen that the cusp/cleft "walks" from 74-75˚ MLAT via 71-72˚ MLAT and back to 75-78˚ MLAT just after magnetic noon.

The MSP in Longyearbyen confirms this picture, see Figure 5.7. Here the 630 nm and 557 nm intensities is shown only for elevations > 15˚. The same equatorward motion of the 630 nm oval from 74-75˚ MLAT via 71-72˚ MLAT and back to 75-78˚ MLAT around magnetic noon is seen here. In fact the very good agreement is suggesting that our assumption of 250 km altitude for the 630 nm emissions is not too bad.

It must also be noted that the auroral arc just before magnetic noon looks wider in magnetic latitude as seen from Ny Ålesund than from Longyearbyen. This can be explained by a difference between Ny Ålesund and Longyearbyen in the elevation angles where the auroral structure is observed. Ny Ålesund is further poleward than Longyearbyen and is therefore looking at the same auroral pattern at a lower elevation angle. If the aurora has some extent in altitude, which is reasonable especially for 630 nm, the Ny Ålesund MSP, looking more from the side, will observe the same auroral signature at several elevations. Thereby, the Ny Ålesund arc becomes a bit wider at low equatorward elevations.

Figure 5.8 presents the two other MSP channels in Longyearbyen; 427.8 nm and 486.1 nm. Here also the intensities are shown only at elevations above 15˚. For both channels the assumed altitude is 120 km. The intensities are very low in the 486.1 nm channel, but the 427.8 nm intensities show a similar equatorward motion near noon, though not as far equatorward as the 630 nm.

From Figure 5.7 and Figure 5.8 (upper panel) a strong auroral activity was observed in the nightside from 19 to 22 UT (22-01 MLT). The AE-index (Figure 5.2) suggests that this optical activity was associated with intensification of the electrojet and substorm activity, probably poleward expansions. However, further discussion of this nightside event is without the scope of this thesis.

Looking at the 557.7 nm intensities in Figure 5.6 and Figure 5.7, the region of almost no emissions from 10-12 MLT and the following region of relatively strong discrete structures from 13-16 MLT is interesting. [Cogger et al., 1977] have reported a gap or a discontinuity in the 557.7 nm aurora to be usually present (although not always) in the 10.5-12.5 MLT sector, consistent with Figure 5.6 and Figure 5.7. Cogger et al. also found a maximum intensity enhancement between 14 and 16 MLT, comparable with our 557.7 nm spot in the 13-16 MLT sector. This strong postnoon optical intensification also coincides with the maximum in the upward Region 1 field-aligned current (FAC), reported by [e.g. Iijima and Potemra, 1978] in the 12 to 16 MLT sector, and the observations of a local

maximum in the precipitating particle energy flux around 77˚ ILAT and 14 MLT, see [Evans, 1985].

Later, [e.g. Liou et al., 1997b] have presented several series of Polar UVI images displaying postnoon bright spots in the neighbourhood of the 14 to 16 MLT sector. The spots were found to be on average 2 hours of MLT in longitudinal extent. Monthly averaged maps of the Polar UVI observations published by [Liou et al., 1997a] also support this pattern. Their maps indicate the maximum dayside UV intensity at about 1500 MLT and 75-76˚ MLAT. [Newell et al., 1996] have presented probability maps of observing electron acceleration events vs. MLT and MLAT based on 9-years of DMSP particle data. Their maps also confirm the 14-16 MLT 'hot spot' of Liou et al., with the maximum centred at 15 MLT. This maximum in probability is present both during southward and northward IMF, but during the latter the spot is more easily distinguished from the evening and nightside electron precipitation. From the maps of Newell et al. the least possible place to observe electron acceleration is at noon; the 'midday gap'.

It must however be noted that the studies of Newell et al. and Liou et al. are an average of different conditions, while our study only is a case study during given conditions. However, the agreement seems apparent. The strong intensity enhancements in the 557.7 nm line observed from both Longyearbyen and Ny Ålesund in the postnoon/afternoon sector may therefore be associated with the region 1 current (upward FAC) and electron acceleration events.

An overall good agreement is found between the IMF clock angle and the latitudinal position of the aurora. The similarity is of course best near noon, since the ionospheric response time has not been included. Away from noon an extra time delay of ~ 10-15 min. (equivalent to an extra 3-4˚ counterclockwise rotation and dependent of the relative location away from noon) must be added to compensate for the ionospheric convection. If this is done, the correspondence becomes better there. The abrupt and very short-lived changes in the IMF on time scales << 5 min. are not clearly reproduced in the auroral position, indicating some inertia in the process.

5.4.3 Traditional Stack Plots

In the last subsection the overview of the optical activity as observed from the Longyearbyen and Ny Ålesund MSPs was presented. This new way of displaying and summarizing MSP data also have some disadvantages. The largest one is the loss of rapid dynamics at time scales of about 1 min. or less. Traditional stack plots are very fruitful here. Therefore, the MSP activity in the 630.0 nm, 557.7 nm and 427.8 nm channels are presented in Figure 5.9, Figure 5.10 and Figure 5.11. Each single scan has been run through a low-pass filter to remove the very small-scale fluctuations.

These stack plots are created in the following way:

$$Y(T, E) = T - C \times I(E) \quad \textbf{(5.1)}$$

where T is the UT time of the scan in seconds, C is a wisely chosen scaling constant and I is the observed intensity at the elevation E. Y is the position along the ordinate or time axis of the curve at a given time and elevation.

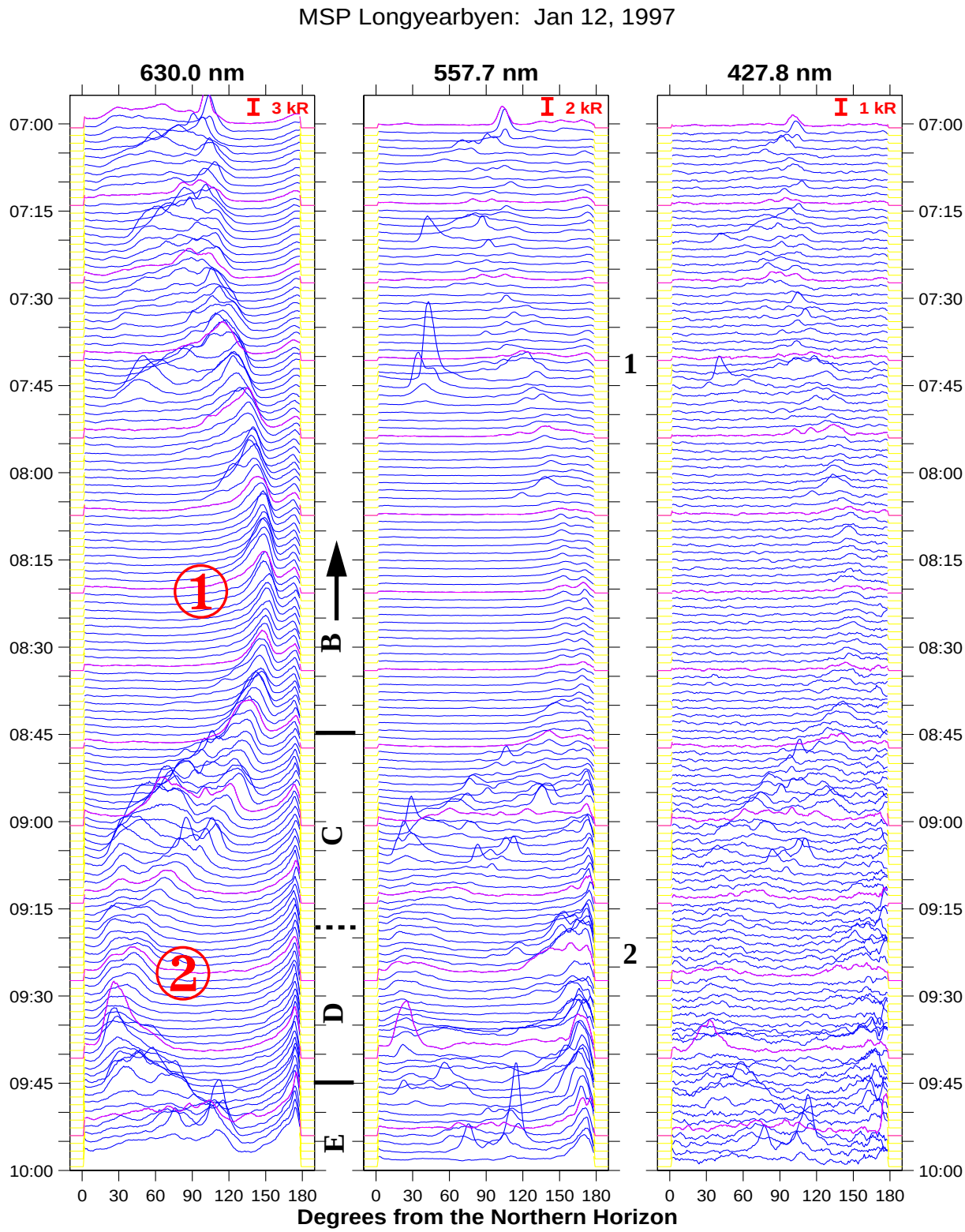

FIGURE 5.9 MSP from Longyearbyen January 12 1997, 07:00 to 10:00 UT. The Type ① and ② auroras, intervals **B**, **C**, **D** and **E** of [Sandholt et al., 1998] and the events **1** & **2** to be discussed in Section 5.6 are marked.

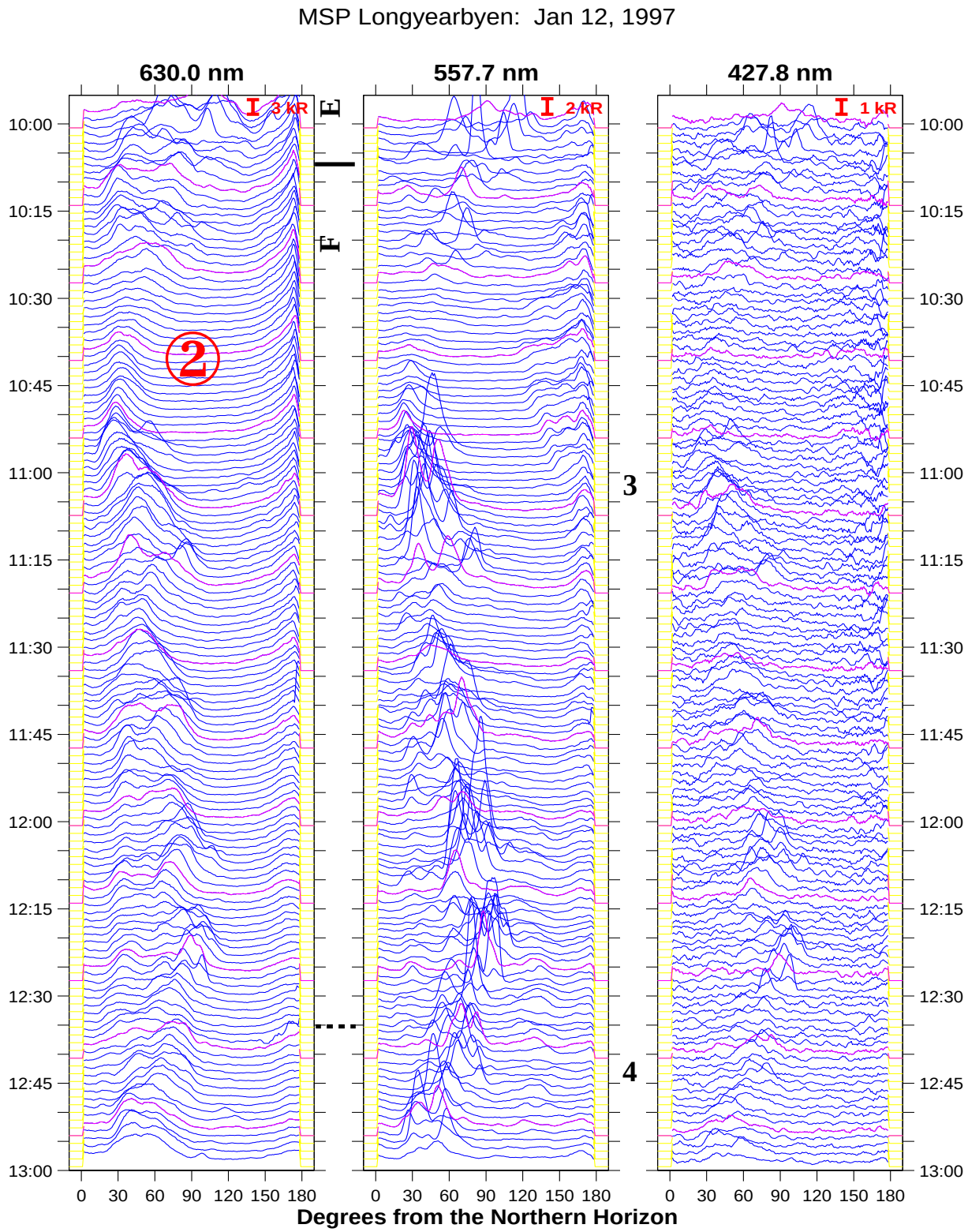

FIGURE 5.10 MSP from Longyearbyen January 12 1997, 10:00 to 13:00 UT. The Type ① and ② auroras, intervals **E** and **F** of [Sandholt et al., 1998] and the events **3** & **4** to be discussed in Section 5.6 are marked.

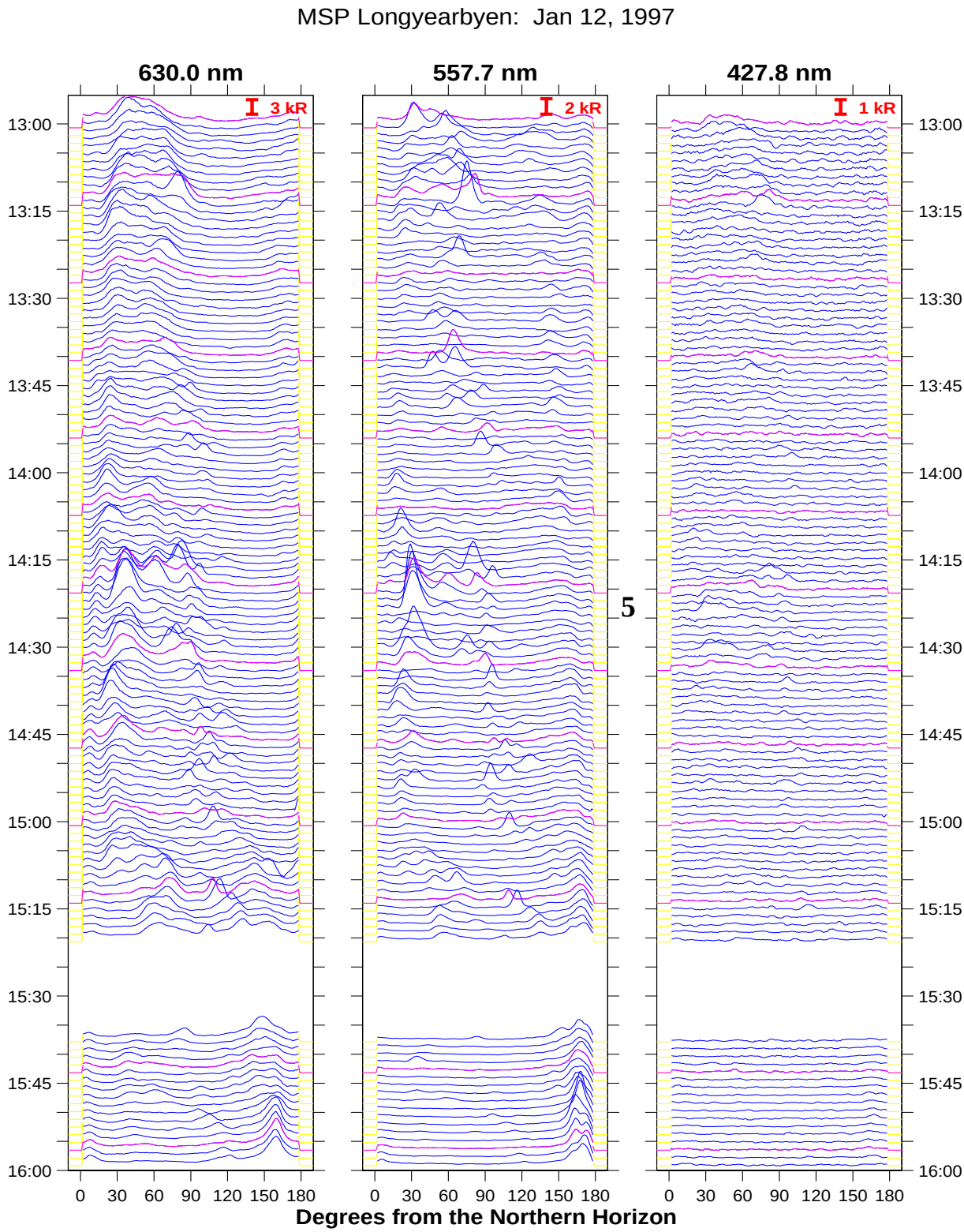

FIGURE 5.11 MSP from Longyearbyen January 12 1997, 13:00 to 16:00 UT. The event **5** to be discussed in Section 5.6 is marked.

There is one difficulty in using this method. If an offset or a background intensity is present, then each scan is shifted in time. This is clearly illustrated e.g. in the last scan in the 630.0 nm panel in Figure 5.9, where the scan looks shifted 3-4 min. backwards in time. This time shift is however not always easy to discover, so to prevent confusion a reference time (equal to when the intensity is 0) of each scan must be indicated. This is shown using grey lines to the left and right in each panel in Figure 5.9 to Figure 5.11. To more easily see the time of each scan, every 10th scan is also plotted using a heavy weighted dotted line.

The intensity of the 427.8 nm band (N_2^+) is nearly independent of the energy for electrons between 0.5 and 20 keV, [Omholt, 1971, and references therein; Carlson Jr. and Egeland, 1995]. Hence, the intensity of this band can be used to determine the net downward electron energy. But, as discussed by [Omholt, 1971] some practical problems arise. Optical instruments from the ground integrate along the line-of-sight, so a direct comparison is strictly valid only when the optical observations are made up along the magnetic field line, observing the light produced by the group of particles following exactly that field line. Away from this line the measurements are useful too, as an indicator, although here the connection is not this direct.

In Figure 5.9 to Figure 5.11 the 427.8 nm band more or less reproduces the main structures in 557.7 nm line, however, the intensities are less. The equatorward displacement of the aurora is also clearly seen in the interval denoted ‘B’. The intervals B, C, D, E and F have been adapted from the study of [Sandholt et al., 1998], and the marks 1, 2, 3, 4 and 5 refer to the NOAA-12 passes to be discussed in Section 5.6.

5.5 The All-Sky TV Camera

The MSP gives no azimuthal resolution, so to fulfil the picture, All-Sky TV Cameras are needed. The All-Sky TV Camera, having the largest field of view, is the best optical instrument to monitor spatial and temporal variations in the aurora as seen from the ground. Figure 5.12, Figure 5.13, Figure 5.14 and Figure 5.15 show the aurora in 5 minutes steps from 07:00 to 14:55 UT January 12 1997 as seen by the 630.0 nm UNIS/UiO camera. Each All-Sky TV image is cut at 70˚ zenith-angle and run through a projection routine, assuming the optical emissions are in 250 km altitude, a typical height for 630.0 nm emissions. This altitude is also in good agreement with the results obtained in Section 5.4.1.

The final image is then projected onto the world-map superposed with a geographical grid. Each image presented in this thesis is an integration over a 20 s interval, where the given time is the centre time of the interval, and the same colour table is used, so the relative intensities are comparable. The chosen 5 min. steps between each image, in this section, only gives the large-scale temporal variations. Rapid dynamics at smaller time-scales may disappear and is not shown here.

However, it is the overview of the more stable and long-lived features that are of most interest now. This overview will constitute a main framework for the discussion of the NOAA-12 satellite passes in the next section. Since each crossing last just for some few minutes, when interpreting only particle data from a satellite, it is therefore hard to separate the spatial variations from the temporal. Thus, the comprehensive review of the auroral activity during the period of observation as seen by an observer at the Auroral Station, will give an extended information. Consequently, the five NOAA-12 passes (**1**, **2**, **3**, **4** and **5**) through the

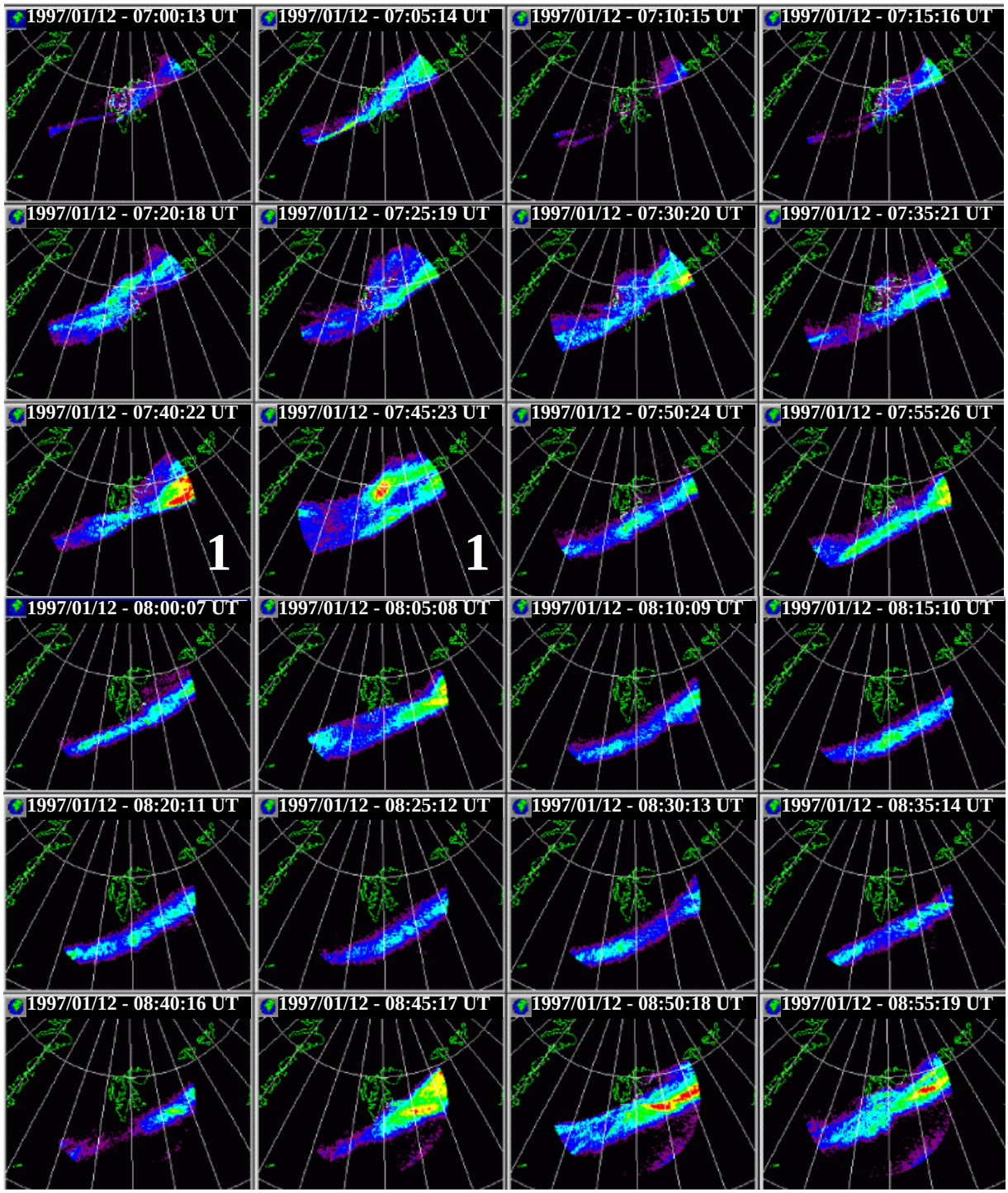

FIGURE 5.12 ASC TV images (630.0 nm) projected to 250 km altitude, from the Auroral Station in Longyearbyen 07:00 to 08:55 UT on January 12 1997. The event **1**, related to a NOAA-12 pass to be discussed in Section 5.6, is marked.

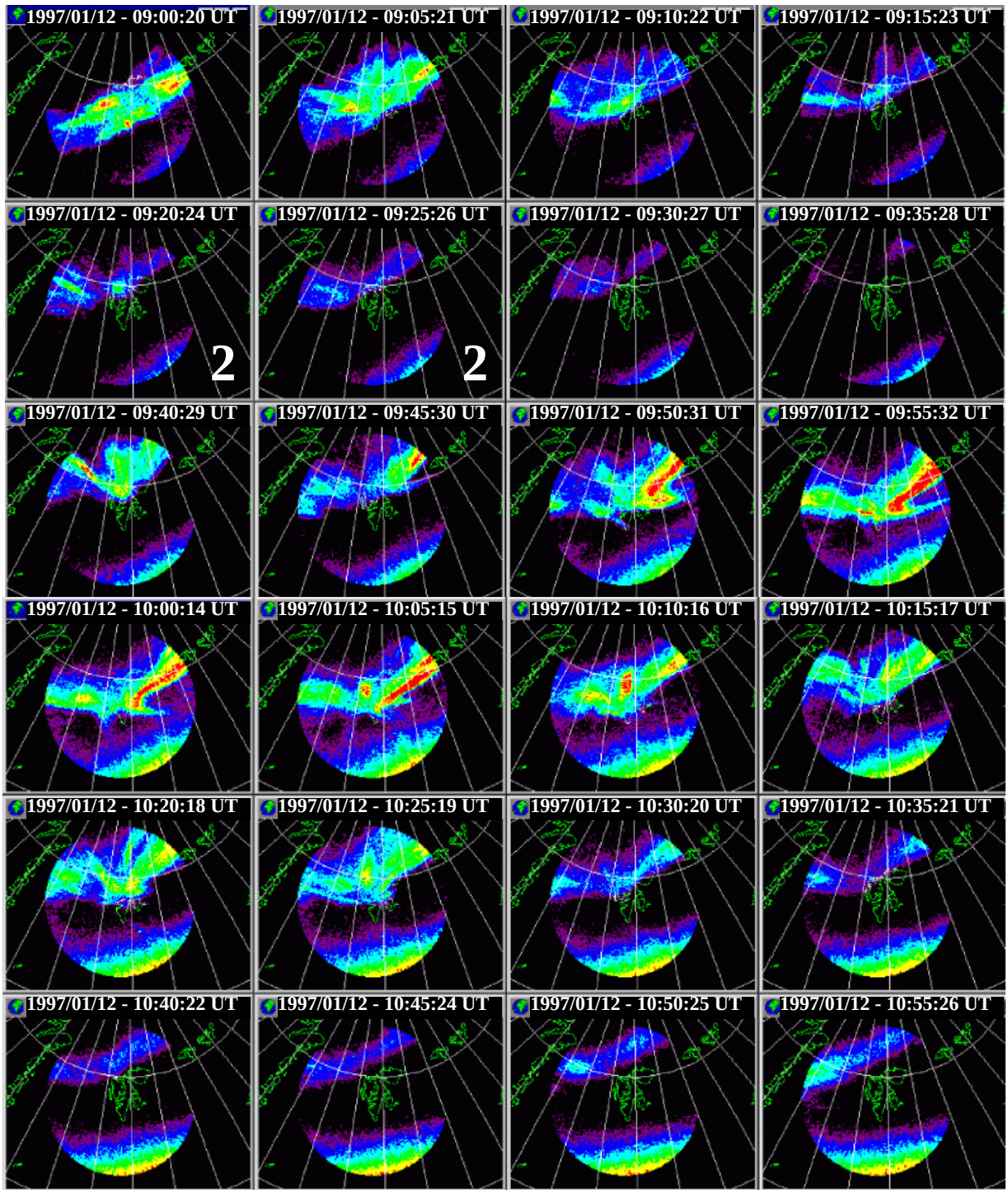

FIGURE 5.13 ASC TV images (630.0 nm) projected to 250 km altitude, from the Auroral Station in Longyearbyen 09:00 to 10:55 UT on January 12 1997. The event **2**, related to a NOAA-12 pass to be discussed in Section 5.6, is marked.

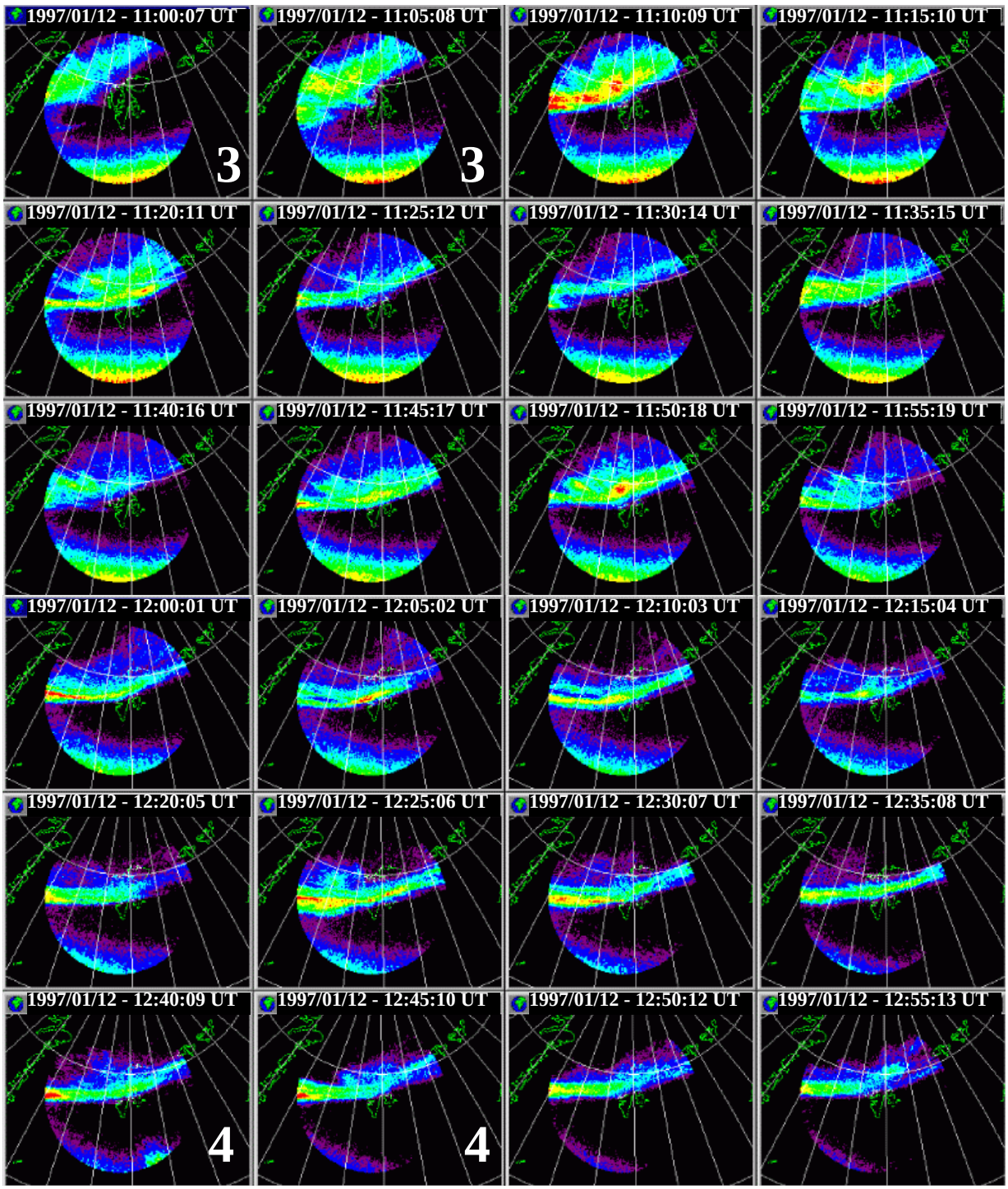

FIGURE 5.14 ASC TV images (630.0 nm) projected to 250 km altitude, from the Auroral Station in Longyearbyen 11:00 to 12:55 UT on January 12 1997. The events **3** & **4**, related to two NOAA-12 passes to be discussed in Section 5.6, are marked.

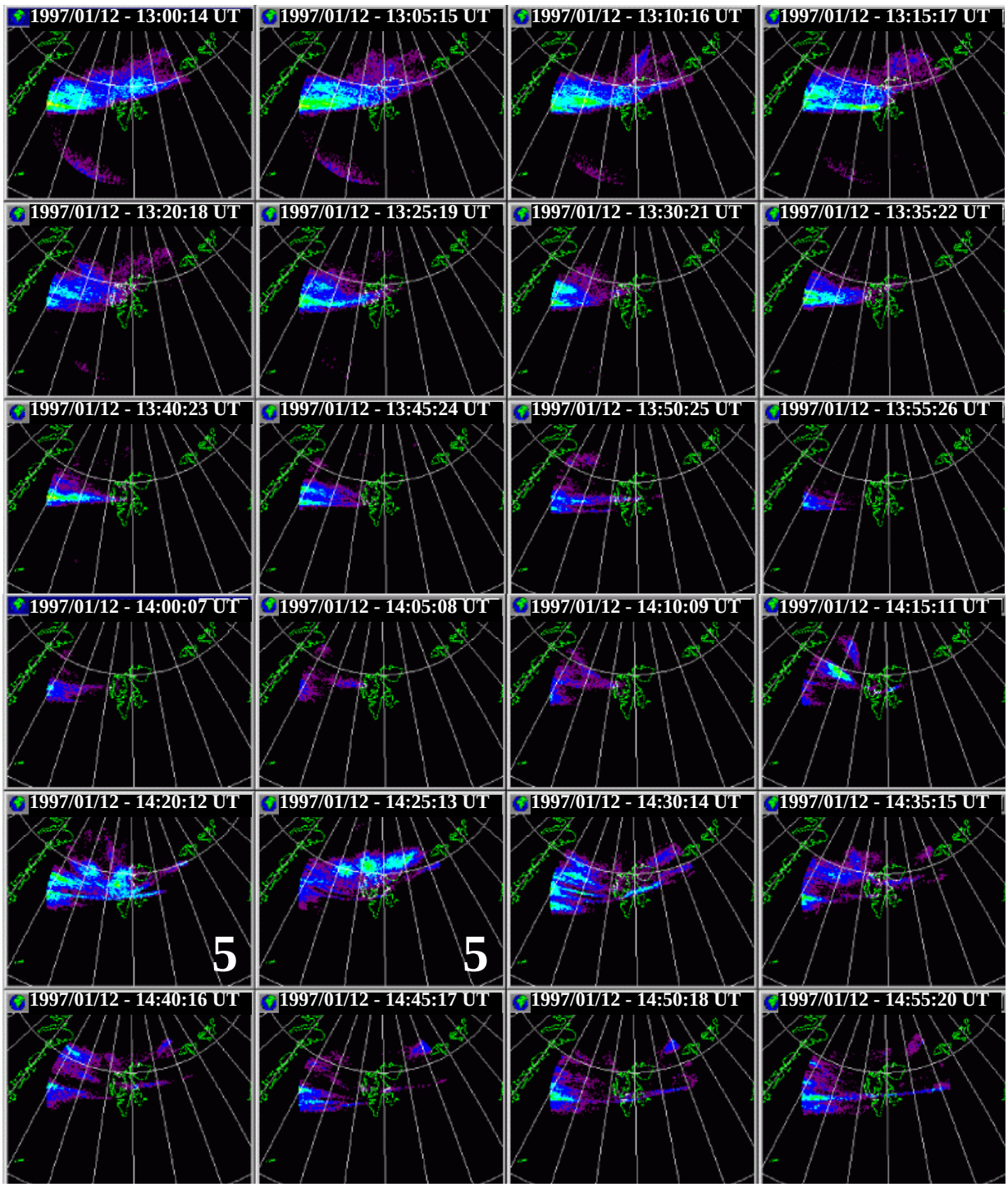

FIGURE 5.15 ASC TV images (630.0 nm) projected to 250 km altitude, from the Auroral Station in Longyearbyen 13:00 to 14:55 UT on January 12 1997. The event **5**, related to a NOAA-12 pass to be discussed in Section 5.6, is marked.

optical field-of-view are also marked in Figure 5.12 to Figure 5.16. The details during each of the five NOAA-12 passes will be presented in Section 5.6.

The equatorward motion of the 630.0 nm emissions from about 07:30 to 09:00 UT, described in Section 5.4 for the MSP, is also clearly seen in Figure 5.12 and Figure 5.13. These figures clearly demonstrates how the whole arc within the field-of-view is displaced equatorward, reaching the minimum magnetic latitude from about 08:10 to 08:40 UT. Therefore, the equatorward motion of the 630.0 nm intensity discussed in Section 5.4 is a real one and no artificial effects caused by auroral structures moving in the east/west direction through the MSP field-of-view.

5.6 Event Studies

Having presented the groundbased optical overview as seen from Svalbard and the matching solar wind parameters in the previous sections, it is now fruitful to compare with the simultaneous particle data from five NOAA-12 satellite passes over Svalbard. This comparison is partly motivated by the fact that it is sometimes very hard to distinguish the LLBL from the cusp using only groundbased optics, [Sandholt, 1990]. Since typically no clear transition signature is found in the electron fluxes near the cusp/LLBL border, [Newell and Meng, 1988], the electron aurora (630.0 nm) of these two regions is not expected to be separable.

5.6.1 The First Pass (07:42-07:45 UT)

NOAA-12 first passed over Svalbard at 07:42-07:45 UT on January 12, see Figure 5.17. The corresponding electron and proton observations from the MEDED and TED detectors are displayed in Figure 5.16. From the top the following is plotted:

1. The 0˚ TED electron integral number flux in the 300-458 eV energy range.
2. The 10˚ and 80˚ MEPED electron integral number fluxes (>30 keV) plotted as solid and dot-dashed lines, respectively.
3. The 10˚ and 80˚ MEPED electron integral number fluxes (>100 keV), plotted as solid and dot-dashed lines, respectively.
4. The characteristic TED electron energy in the 300 eV to 20 keV energy range.
5. The 0˚ TED proton integral number flux in the 300-2349 eV energy range. This is the sum of the 300-458 eV, 773-1088 eV and 1718- 2349 eV channels.
6. The 10˚ and 80˚ MEPED proton differential number fluxes (30-80 keV), plotted as solid and dot-dashed lines, respectively.
7. The 10˚ and 80˚ MEPED proton differential number fluxes (80-250 keV), plotted as solid and dot-dashed lines, respectively.
8. The characteristic TED proton energy in the 300 eV to 20 keV energy range.

Borders in the particle observations are marked by either dotted vertical guide lines (to be compared with ASC TV images) or arrows (to be commented on in the text). The grey shading indicates when NOAA-12 was within the ASC field-of-view.

As discussed in Section 2.1.1 on page 16 and Section 2.1.2 on page 18 both the 0˚ and 10˚ detectors are detecting particles within the atmospheric loss cone, while the 80˚ detector is monitoring the trapped particles. Furthermore, in Panel 1 and Panel 5 the time resolution varies through the satellite pass in a cycle of 8, 8, 8 and 16 seconds. In all the other panels the time resolution is 2 seconds, cf. Section 2.1.2 too.

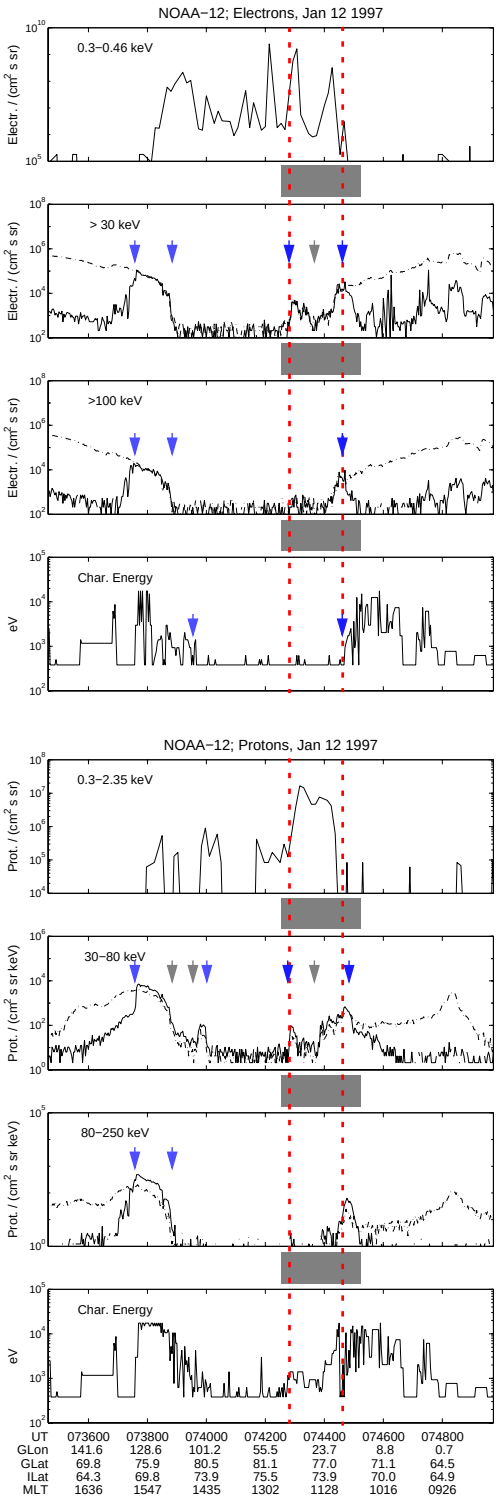

FIGURE 5.16 NOAA-12 particle observations from the first Svalbard pass, where the **LLBL onset** and the **sheath electron cutoff** are the two main borders. (Other borders, see text.)

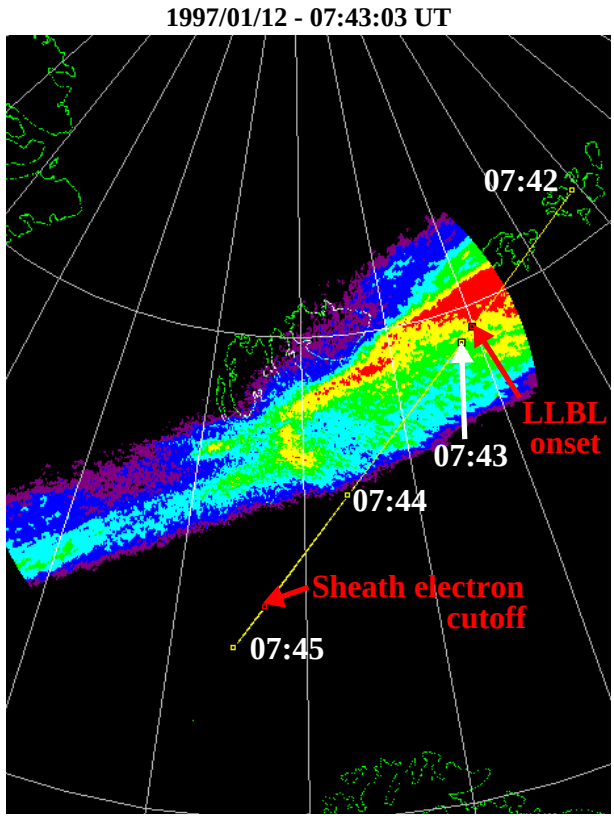

FIGURE 5.17 630.0 nm UiO/UNIS ASC from the Auroral Station in Longyearbyen at 07:43:03 UT on January 12 1997. The image is projected to 250 km, and the NOAA-12 footprint and two particle borders are added, see text.

The ASC TV image in Figure 5.17 was taken when the NOAA-12 satellite was in the centre of the optical field-of-view. Some useful coordinates obtained from the satellite data should therefore be listed:

- 07:42:00 UT (1302 MLT, 75.5˚ ILAT), the maximum invariant latitude of the pass.
- 07:43:00 UT (1213 MLT, 75.1˚ ILAT)
- 07:44:00 UT (1128 MLT, 73.9˚ ILAT)
- 07:45:00 UT (1049 MLT, 72.2˚ ILAT)

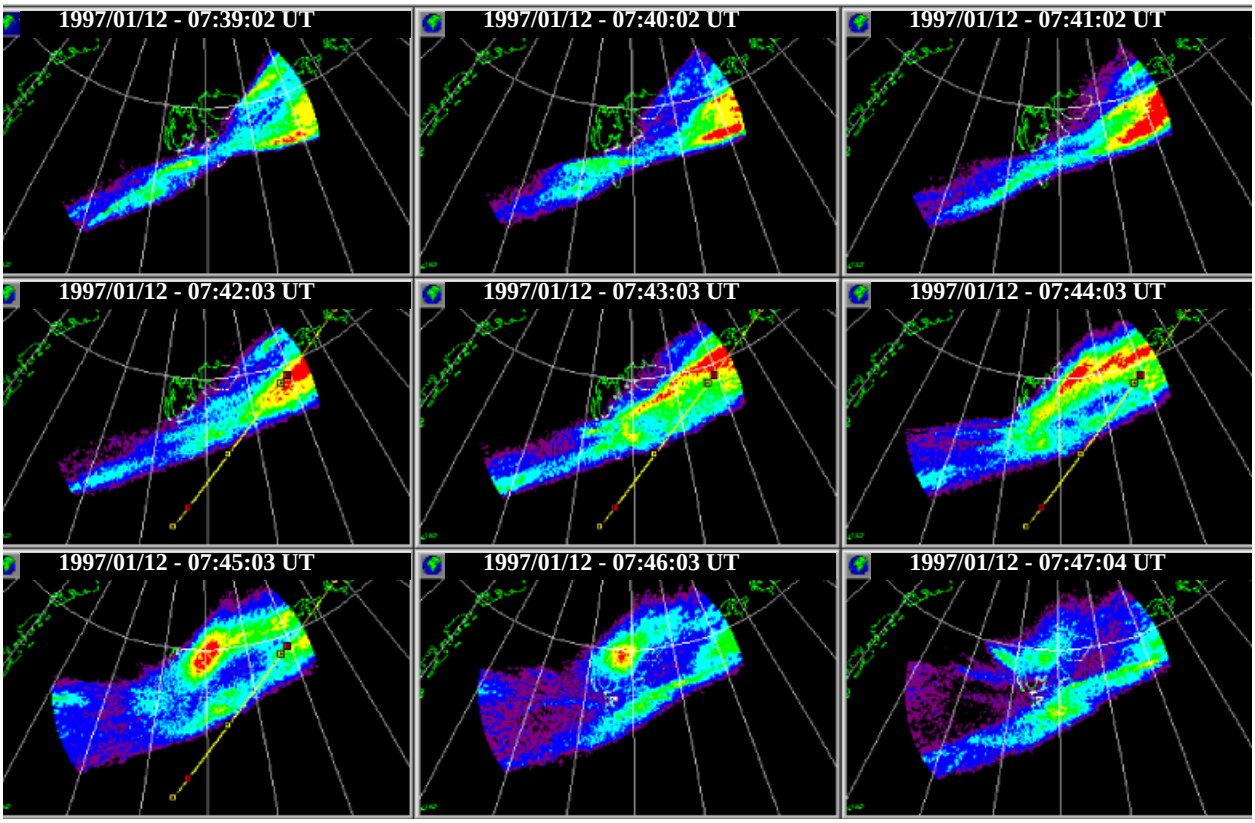

FIGURE 5.18 A westward and poleward moving auroral form during IMF By > 0. The 630.0 nm UiO/UNIS ASC TV images are projected to 250 km altitude, using a pseudo colour table, where red is maximum intensity and blue is minimum. The NOAA-12 footprint is indicated plotted in four of the images (when the satellite was within the field-of-view), see Figure 5.17 for reference.

NOAA-12 is thus moving equatorward through the ASC field-of-view. In order to separate magnetospheric particles from magnetosheath particles, two definitions must be made:

- If a region contains <1 keV electrons (characteristic electron energy <1 keV), magnetosheath particles are present.
- If a region contains >30 keV particles, magnetospheric particles are present.

These definitions are in good agreement with Chapter 4 and the classification used by [Moen et al., 1996].

From the particle data in Figure 5.16 the characteristic electron energy (Panel 4) is low and at the threshold level of 380 eV from 07:39:38 UT (1450 MLT,73.3˚ ILAT) to **07:44:44 UT** (1059 MLT, 72.7˚ ILAT). Thus in this interval magnetosheath electrons are present. The latter border is the **sheath electron cutoff** and is within the ASC field-of-view (Figure 5.17). It marks the equatorward border of the magnetosheath electron precipitation. This border is also indicated by the second vertical guide line in Figure 5.16.

Within both the ASC field-of-view and the region of magnetosheath electron precipitation, an extra very clear border is found in the energetic electrons and protons. At **07:42:54 UT** (1218 MLT, 75.1˚ ILAT) the >30 keV electron fluxes (Panel 2) and the 30-80 keV proton fluxes (Panel 6) abruptly rise from the background flux level. This marks the poleward boundary where magnetospheric particles are present; the **LLBL onset** in Figure 5.17. This border is marked by the first vertical guide line in Figure 5.16.

Between these two main borders (07:42:54-07:44:44 UT) particles of both magnetosheath and magnetospheric origin was detected. Therefore, this region can be interpreted as the LLBL, cf. Section 4.2.2. Poleward of the LLBL onset (07:42:54 UT) only particles of magnetosheath origin is detected, thus that region can be interpreted as the cusp, cf. Section 4.2.1.

A further inspection of the particle observations around the two main borders reveals that the characteristic proton energy (Panel 8) increased a bit when NOAA-12 crossed the LLBL onset. And, the >30 keV & >100 keV electron and 30-80 keV proton fluxes changed from isotropic to anisotropic at the magnetosheath electron cutoff, the equatorward boundary of the LLBL.

Within the LLBL a strong precipitation of 0.3-2.35 keV magnetosheath protons (Panel 5) was also found. These magnetosheath protons showed their maximum flux near the poleward border of the LLBL, weakly decreasing in intensity equatorward. At the poleward and equatorward borders of the LLBL an abrupt rise/fall in the flux (a factor about 100) was measured.

The strongest 630.0 nm intensity was observed in the cusp, poleward of the LLBL onset in Figure 5.17. The 0.3-0.46 keV electron flux does not explain the difference in the luminosity between the cusp and the LLBL, which suggests the presence of an intense flux of electrons <300 eV. If the NOAA-12 satellite could have measured electrons <300 eV, high fluxes would be expected in the cusp, cf. Section 4.2.1. If the magnetic local time (about 12 MLT) and the invariant latitude (75.1-75.5˚ ILAT) are considered, this cusp is in good agreement with the position of the statistical cusp of [Newell and Meng, 1992; Newell and Meng, 1994]. Just equatorward of the cusp, in the LLBL, the 630.0 nm intensity was less and decreased away from the LLBL onset.

The region equatorward of the LLBL and the magnetosheath electron cutoff (07:44:44 UT, 72.7˚ ILAT) in Figure 5.17 is most likely the dayside extension of the CPS. Here the magnetosheath plasma is absent, and the characteristic electron energy is high. Thus, only magnetospheric particles are detected.

Then the question arises whether there is a BPS within the so far classified LLBL? In the LLBL, between the LLBL onset and the magnetosheath electron cutoff, changing flux levels is observed in Figure 5.16. The high-energy electron and proton fluxes are seen to rise and fall off several times during this crossing. This can be caused by the satellite skimming along the boundaries of a temporarily varying aurora in the LLBL, cf. Figure 5.18.

However, from the energetic particles observations in Figure 5.16 and the ASC TV image (Figure 5.17), it looks as if an extra border may be present within this interval. At 07:43:50 UT (1135 MLT, 74.1˚ ILAT) the isotropic energetic electron and proton fluxes

experienced a local minimum, and around the same time NOAA-12 crossed the equatorward boundary of the 630 nm emissions (Display 6 in Figure 5.18). Further equatorward no significant 630 nm was observed and the energetic particle fluxes (>100 keV & 80-250 keV) also became important. Therefore, it is possible that this region (72.7-74.1˚ ILAT) could be the noon-prenoon BPS, where the LLBL is just poleward of it (74.1-75.5˚ ILAT). If so; the 30-80 keV proton flux increases vs. increasing latitude in the LLBL, all the energetic particle fluxes decrease vs. increasing latitude in the BPS, and the energetic particle fluxes are in average (during this satellite pass) larger in the BPS than in the LLBL. Nevertheless, we will not stress this point any further in this thesis and just leave the question open for future studies. The LLBL onset and the magnetosheath electron cutoff is still clear borders.

This auroral event is a typical moving auroral form as reported by [e.g. Sandholt et al., 1986; Sandholt et al., 1993; Moen et al., 1995; Sandholt et al., 1998]. During periods of southward IMF (CAR 3) auroral forms are seen moving poleward from the equatorward boundary of the background arc (Type 1 aurora). This motion is strongly dependent on the IMF By component and is westward (eastward) during By > 0 (By > 0). Allowing a time shift of ~ 25 min. from Wind to the noon ionosphere, the IMF around 07:20 UT (guide line 1 in Figure 5.1) is found to correspond with this event. At about 07:20 UT the IMF was approximately (-1, 3, -6) nT GSE. Therefore, according to e.g. [Sandholt et al., 1993; Sandholt et al., 1998] a westward moving auroral form is expected. This is also what is seen in Figure 5.18. An auroral form originating in the east (postnoon) is seen to move westward and poleward (prenoon) before it fades out, probably on mantle field lines. We do not have any particle observations from the fade out region, since NOAA-12 did not traverse that, however, [Sandholt et al., 1993] found a similar event to fade out on mantle field lines.

From the MSP (Figure 5.9) and ASC (Figure 5.12) observations this moving auroral form is seen to evolve from a rather narrow and stable in latitude, east-west elongated, Type 1 aurora. The equatorward boundary was moving very slowly equatorward, and no other (this clear) poleward moving candidates were observed 07:30 to 08:00 UT. The poleward moving form was also associated with very strong (>10 kR) 557.7 nm emissions at 07:44 to 07:47 UT ~ 45˚ north of zenith in Longyearbyen, Figure 5.9. The Ny Ålesund MSP observed this structure near zenith. Combining these two observations, from Figure 2.5 in 120 km altitude, this strong intensification is found to be associated with the strong 630 nm red patch in Display 7 and 8 of Figure 5.18. At the same time the Longyearbyen 427.8 nm line also intensified at the same elevation, indicating a major energy flux being precipitated. From Figure 5.9 the emissions of the 557.7 nm line also seemed to move poleward, but we do not have All-Sky images in that wavelength.

Looking closer at Figure 5.1, the IMF clock angle is seen to decrease from ~ 150˚ to ~ 120˚ 3-4 min. before the vertical guide line number 1 at 07:20 UT, suggesting the poleward moving auroral form might be associated with this. Since no other very strong moving forms are observed near this form (in time), such an interpretation seems reasonable. This leads to a question; is the occurrence of moving auroral forms not just dependent of IMF being southward, but also to some extent dependent of the degree of the southward turning? With other words; is there an extra clock angle regime CAR 4 within that of [Sandholt et al., 1998], where moving auroral forms are less frequent? From Figure 5.1 in region B the auroral forms look weaker and are almost absent from 08:05

to 08:35 UT, consistent with the IMF clock angle being very large (~ 170-180˚). Thus, should there be a fourth clock angle regime CAR 4 for e.g. θ >135˚, where poleward moving auroral forms are nearly absent and the background arc very stable? This is however outside the scope of this thesis, but it needs to be studied further. Nevertheless, this event looks to be associated with low-latitude reconnection at the magnetopause, and a decrease in the low-latitude reconnection rate may have initiated the poleward moving form.

This NOAA-12 satellite pass also contain interesting information outside the optical field-of-view. In the afternoon sector, encountered before the satellite passed over Svalbard, several other interesting borders are seen. At 07:37:26 UT (1603 MLT, 68.3˚ ILAT) NOAA-12 crossed the >100 keV electron and 80-250 keV proton isotropy boundaries (blue markers in Figure 5.16). About 10 sec. later (0.6˚ ILAT poleward) the satellite traversed the >30 keV electron and 30-80 keV proton isotropy boundaries. This is in good agreement with a study of [Sergeev et al., 1983]. They investigated the nightside isotropy boundary using ESRO IA energetic proton observations during quiet conditions and compared with magnetic field models. Their calculations showed the isotropy boundary to move equatorward for increasing geomagnetic activity, and for a higher proton energy the more equatorward is the isotropic boundary, controlled by the ratio of the field line curvature and the particle gyroradius, [cf. Sergeev et al., 1983, Figure 2].

Further poleward, at 07:38:48 UT (1521 MLT, 71.7˚ ILAT), are the >30 keV and >100 keV electron and 80-250 keV proton trapping boundaries found. An abrupt fall in the 30-80 keV isotropic proton flux is also observed here, however, this trapping boundary is not traversed before 07:40:00 UT (1435 MLT, 73.9˚ ILAT). In between, at 07:39:40 UT (1448 MLT, 73.4˚ ILAT), both a drop in the characteristic electron energy below 1 keV (magnetosheath electron onset) and a sudden rise in the 30-80 keV protons were detected. This latter rather narrow (0.5˚ ILAT wide) spike in the energetic protons looks very similar to another 0.2˚ ILAT wide local maximum in the noon sector within the ASC field-of-view, just equatorward of the LLBL onset. However, a difference between these two structures is that the first one was traversed almost straight poleward along the meridian, while the latter crossing also involved a significant longitudinal motion. Furthermore, the noon structure is also associated with an additional population of energetic electrons (as well as the magnetosheath electrons and protons and the energetic protons). It is likely to couple both these structures to the LLBL. If so, the region between is the cusp/mantle[‡‡], which is at least ~ 2.3 hours wide in MLT.

At first sight the noon LLBL event looks quite different from a NOAA-12 pass presented and discussed by [Moen et al., 1996; Lockwood and Moen, 1996], respectively. These authors concluded that they did not find energetic electrons in the LLBL, and they associated an abrupt cutoff in the magnetospheric electron flux, [cf. Moen et al., 1996, Figure 4 d) and f)], at the LLBL/CPS boundary with the last closed field line. However, Moen et al. used a linear ordinate (Y-axis) instead of the logarithmic scale we use (e.g. Figure 5.16). In a linear axis system the presence of a significant energetic electron flux, say a factor >10 less than the maximum CPS level, will effectively be squeezed towards and

[‡‡] Due to the very low particle energies in the mantle (cf. Section 4.2.3) the low energy TED detector is probably not able to distinguish between the mantle and the cusp.

hidden in the abscissa (X-axis). Therefore, a logarithmic ordinate is preferable, and the conclusion of [Moen et al., 1996; Lockwood and Moen, 1996] of no energetic electrons in the LLBL may be wrong.

Is the LLBL open? Several of the observations during the NOAA-12 crossing of the LLBL support the open field line model results of [Lyons et al., 1994], cf. Section 4.4.2:

- The abrupt decrease in the flux of magnetosheath plasma at the equatorward boundary of the LLBL
- The abrupt decrease to background intensity of magnetospheric particles across the LLBL/cusp border
- The isotropic magnetospheric protons within and equatorward of the LLBL
- The continuous flux of magnetospheric protons (30-80 keV) across the equatorward boundary of the LLBL
- The decrease in the magnetospheric electron flux at the equatorward boundary of the LLBL

However, the magnetospheric electrons had an isotropic pitch angle distribution rather than a trapped one within the LLBL, and only the magnetosheath electrons looked continuous across the cusp/LLBL boundary. The magnetosheath protons (present both in the cusp and LLBL) had a sharp rise in intensity from the cusp to the LLBL. The more results in agreement than in disagreement with the model suggest the LLBL was open in this case. This is also in accordance with an open LLBL near noon under normal conditions, [Newell and Meng, 1998]. However, the few discrepancies with Lyons et al.'s model results need to be studied further to draw more precise conclusions. That is without the scope of this thesis and is left for future work.

5.6.2 The Second Pass (09:23-09:26 UT)

The next pass (09:23-09:26 UT) is a completely different situation, displayed in Figure 5.19; the panels are similar to those of Figure 5.16. The All-Sky TV image when NOAA-12 was in the centre of the field-of-view, is shown in Figure 5.20. Some useful coordinates obtained from the satellite data files are:

- 09:23:00 UT (1406 MLT, 76.6˚ ILAT)
- 09:24:00 UT (1312 MLT, 77.0˚ ILAT), the maximum invariant latitude of the pass.
- 09:25:00 UT (1217 MLT, 76.6˚ ILAT)

From these coordinates NOAA-12 moved almost at a constant latitude through the ASC field-of-view. The most clear particle boundaries are the magnetosheath electron onset and cutoff. From 09:21:24 UT (1519 MLT, 74.6˚ ILAT) to **09:25:30 UT** (1150 MLT, 76.1˚ ILAT) magnetosheath electrons are present. This latter border is marked by a vertical guideline in Figure 5.19 and the **sheath electron cutoff** in Figure 5.20. Thus, for the 630.0 nm aurora crossed by NOAA-12 in Figure 5.20 a magnetosheath electron component is present.

From Figure 5.19 no trapping boundaries are found in this satellite pass. However, several isotropy boundaries are encountered both within and outside the ASC field-of-view.

Within the ASC field-of-view these isotropy boundaries are found: the >30 keV electron isotropy boundary at 09:25:10 UT (1208 MLT, 76.4˚ ILAT), the 30-80 keV proton isotropy boundary at 09:25:58 UT (1127 MLT, 75.5˚ ILAT), and the 80-250 keV proton isotropy boundary at 09:26:34 UT (1059 MLT, 74.6˚ ILAT). The >100 keV electron isotropy boundary was coincident with the magnetosheath electron cutoff at 09:25:30 UT.

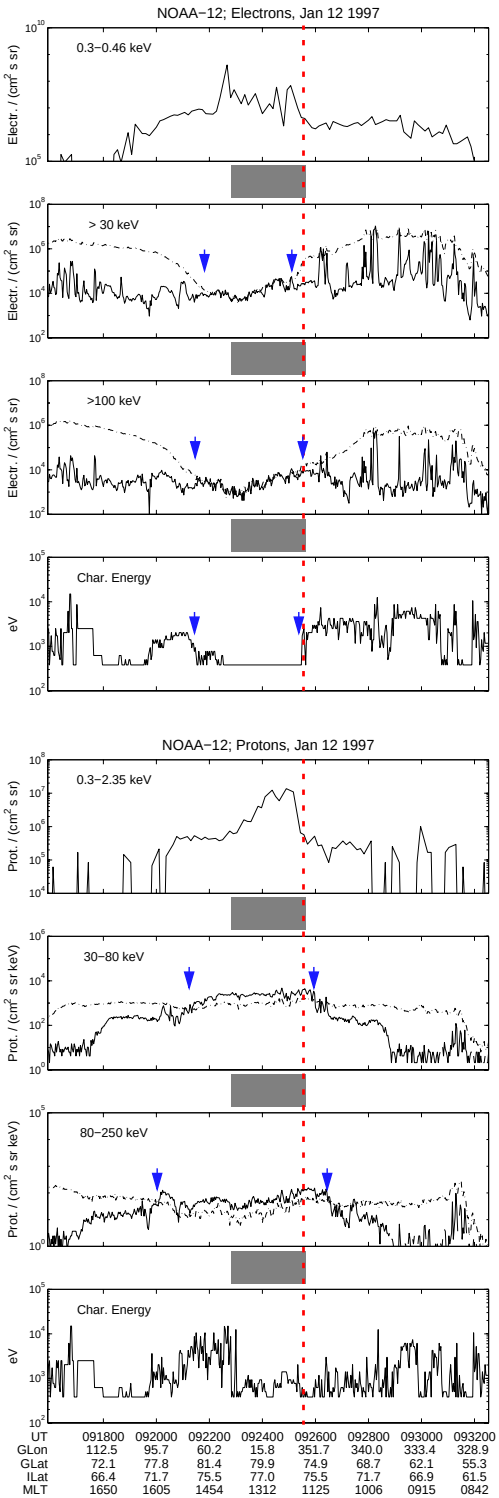

FIGURE 5.19 NOAA-12 particle observations from the second Svalbard pass, where the **magnetosheath electron cutoff** is the main border. (Other borders, see text.)

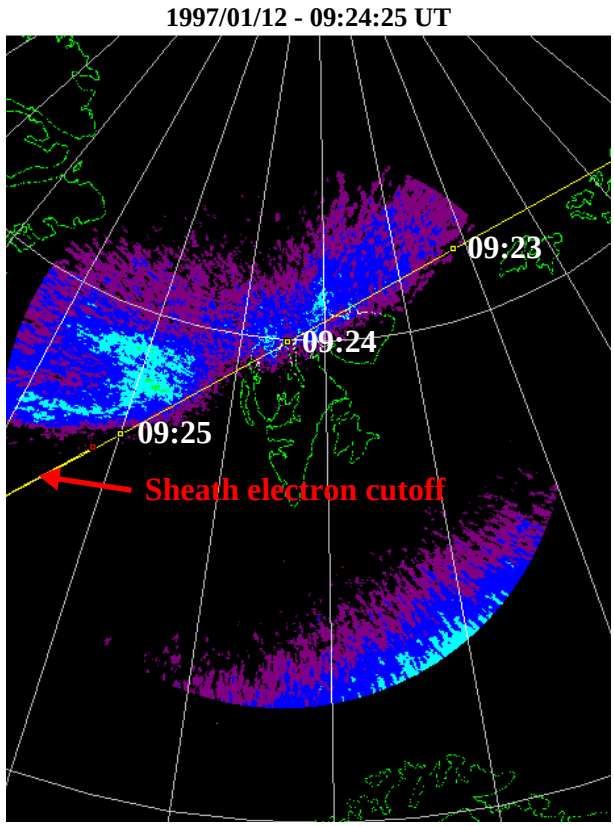

FIGURE 5.20 630.0 nm UiO/UNIS ASC from the Auroral Station in Longyearbyen at 09:25:24 UT on January 12 1997. The image is projected to 250 km, and the NOAA-12 footprint and a particle border are added, see text.

Other borders outside the optical field-of-view in the afternoon sector are; the 80-250 keV proton isotropy boundary at 09:20:06 UT (1603 MLT, 71.8˚ ILAT), the 30-80 keV proton isotropy boundary at 09:21:16 UT (1524 MLT, 74.4˚ ILAT), the >100 keV electron isotropy boundary at 09:21:34 UT (1512 MLT, 74.9˚ ILAT) and the >30 keV electron isotropy boundary at 09:22:12 UT (1445 MLT, 75.8˚ ILAT).

In Figure 5.21 the NOAA-12 footprint is added in the three displays in the middle row. This is where NOAA-12 was within the optical field-of-view. A weak reduction of the lumi-

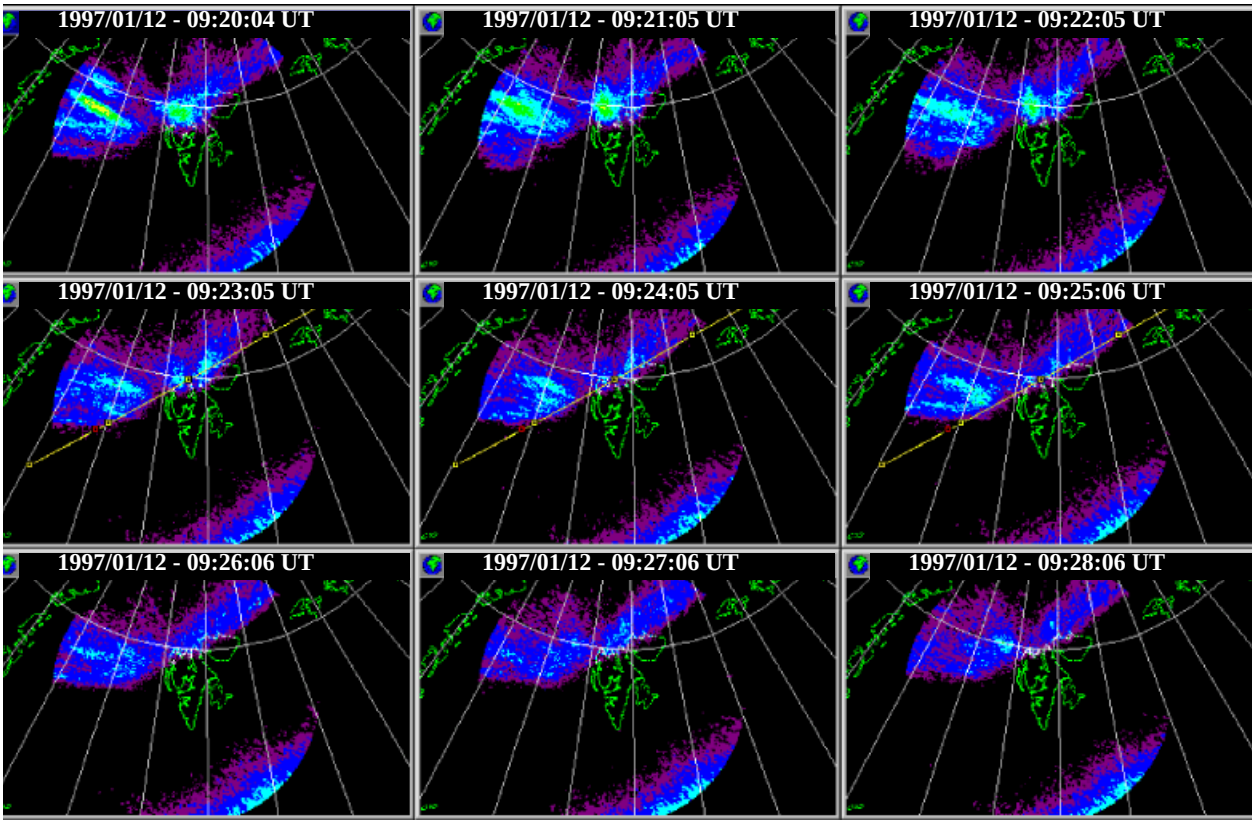

FIGURE 5.21 ASC 09:20:04 to 09:28:06 UT in 1 min. steps on January 12 1997. The images are projected to 250 km altitude using a pseudo colour table, where red is maximum intensity and blue is minimum. The NOAA-12 footprints are plotted in three of the images (when the satellite was within the field-of-view), see Figure 5.20 for reference.

nosity was seen 2-3 min. before the pass. From the MSP (Figure 5.9) and ASC (Figure 5.13) overviews, this second event occurred just after a transition from the presence of both Type 1 and Type 2 aurora to only Type 2 aurora. The fragments of this transition is displayed in the first two displays in Figure 5.21.

The IMF clock angle in Figure 5.1 also changed from regime CAR 2 to CAR 1 just before this event. Assuming a 25 min. time delay from Wind to the noon ionosphere, the IMF conditions observed by Wind (Figure 5.1) around 09:00 UT should correspond to the central time of this event. At 09:00 UT the IMF is found to be (-3, 5, 1) nT GSE. Thus, the IMF is northward and in CAR 1 during the NOAA-12 pass. Although, some few minutes earlier the IMF was in CAR 2.

Nevertheless, this event is much more stable in time than the first one (Section 5.6.1), and the 630 nm intensity is less, as shown in Figure 5.21. This is also supported by the maximum of the 0.3-0.46 keV electron flux being a factor ~ 10 less within the optical field-of-view in Figure 5.19 than in Figure 5.16. The main difference from the first event is the presence of an important population of isotropic energetic particles. The energetic electron and proton fluxes are a factor 100 larger than in the previous NOAA-12 pass. Therefore, this region can-

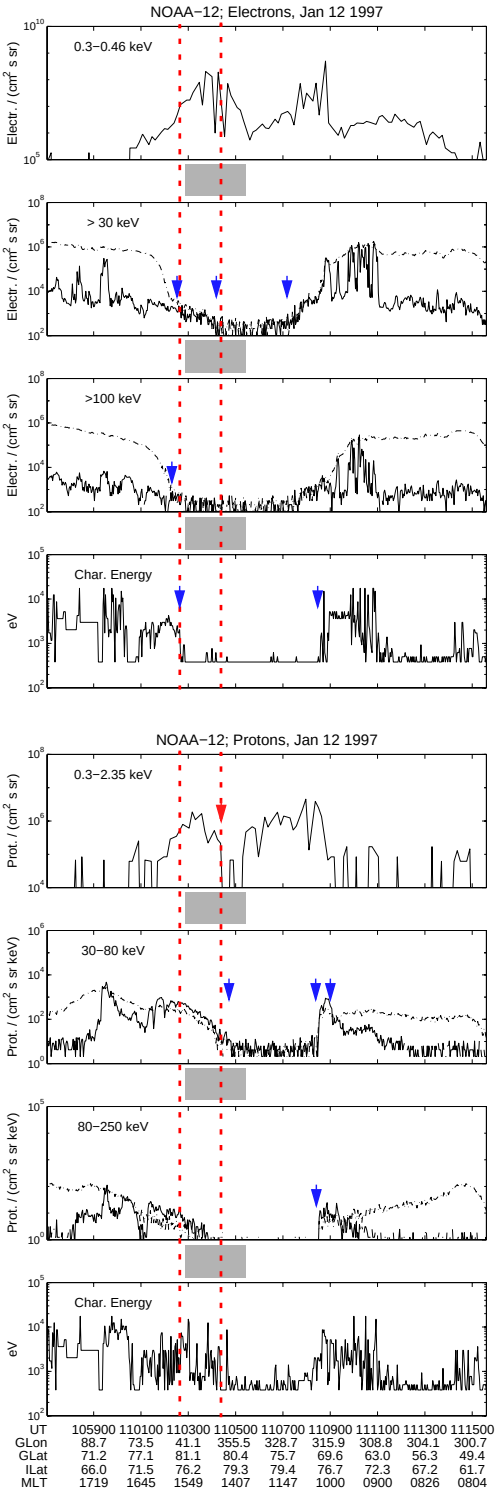

FIGURE 5.22 NOAA-12 particle observations from the third Svalbard. Borders: **Sheath electron onset** and **high-latitude sheath ion cutoff**.

not be cusp. Furthermore, in this satellite pass too a maximum in the magnetosheath proton precipitation (Panel 5) is found within the ASC field-of-view, but in average the characteristic proton energy (Panel 8) is lower. The region can be LLBL, but the very high-latitude position (>76.6˚ ILAT) of the aurora and the characteristic proton energy point at the mantle.

[Murphree et al., 1990] concluded from Viking UV observations that discrete auroral features can exist poleward of the normal dayside aurora in the northern hemisphere during periods of both northward IMF, Bx < 0 and By > 0, as for this event. Later, [Øieroset et al., 1997] studied several cases of northward IMF cusp aurora. They reported Type 2 aurora to occur for both IMF Bx polarities and found enhanced green line intensity during negative Bx conditions. This is in good agreement with the current event, since Figure 5.9 reveal some 557 nm enhancement (~ 1 kR) and Bx is negative. Thus, it is tempting to associate this aurora with high-latitude magnetopause reconnection, see [Øieroset et al., 1997; and references therein]. (Both this and the previous event are planned to be discussed more in detail in a future article, so only a very brief overview is given here.)

5.6.3 The Third Pass (11:03-11:06 UT)

The following NOAA-12 pass over Svalbard at 11:03 to 11:06 UT is displayed in Figure 5.22. The corresponding 630.0 nm ASC TV images are displayed in Figure 5.23. Before discussing the pass any further, some useful footprint coordinates, in the middle row of Figure 5.23, should be listed:

- 11:03:00 UT (1549 MLT, 76.2˚ ILAT)
- 11:04:00 UT (1505 MLT, 78.0˚ ILAT)
- 11:05:00 UT (1407 MLT, 79.3˚ ILAT)

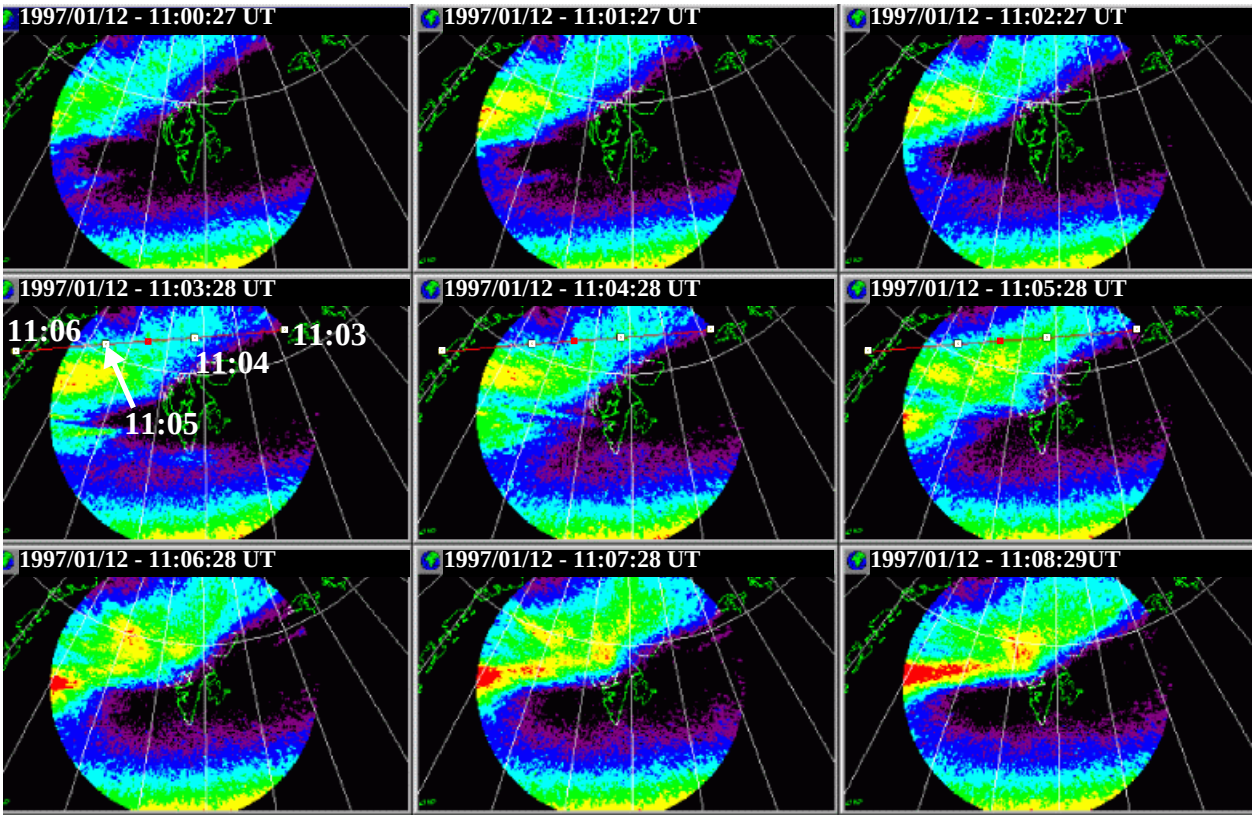

FIGURE 5.23 630.0 nm UiO/UNIS ASC images from the Auroral Station 11:00:27 UT to 11:08:29 UT January 12, 1997. The images are projected to 250 km altitude, using a pseudo colour table, where red is maximum intensity and blue minimum.

- 11:06:00 UT (1258 MLT, 79.8˚ ILAT), the maximum invariant latitude.

From these magnetic coordinates NOAA-12 was continuous moving towards a higher invariant latitude during this pass. Two borders were encountered before NOAA-12 entered the optical field-of-view. At 11:02:20 UT (1611 MLT, 74.8˚ ILAT) the >100 keV electron trapping boundary was crossed. 20 seconds later (**11:02:40 UT**, 1601 MLT, 75.5˚ ILAT) NOAA-12 passed across both the **magnetosheath electron cutoff** and the >30 keV electron isotropy boundary. The latter border is marked by the vertical guide line in Figure 5.22. This is, however, outside and just before NOAA-12 entered the optical field-of-view. Thus, all the optical signatures crossed by NOAA-12 in Figure 5.23 is above this border and poleward of the magnetosheath electron cutoff. No clear energetic proton isotropy boundaries are seen around this time. Nevertheless, around 11:04:12 UT (1454 MLT, 78.3˚ ILAT) the 30-80 keV proton trapping boundary was crossed.

Since NOAA-12 did not reach the maximum latitude before 11:06:00 UT, from the **low-energy protons** (Panel 5 of Figure 5.22) there is also a **poleward border** (indicated by the second vertical guide line in Figure 5.22 and the red spot in Figure 5.23):

- **11:04:22 UT** (1445 MLT, 78.6˚ ILAT)

The low-energy electrons do not show this border, but in the >30 keV electrons a trapping boundary is found.

Therefore, in this satellite pass significant fluxes of both low-energy magnetosheath particles and isotropic high-energy particles were present within the field-of-view. The >30 keV electron flux is a factor 10 larger and the 30-80 keV proton flux was a factor 100 larger than the minimum flux level of the detectors. Both fluxes also decreased as the latitude increased.

A 25 min. IMF time shift gives the matching IMF conditions observed by Wind around 10:38 UT. From Figure 5.1 and the vertical guide line 3, the IMF is found to be about (2, 2, -3) nT GSE, so the IMF is weakly southward. The IMF clock angle was turning from 90-100˚ to a 170˚ spike a couple of minutes later. In the bottom row of Figure 5.23 a probably associated eastward moving form is seen coming into the field-of-view from left. In Figure 5.14 this form is also seen at 11:10 and 11:15 UT.

This event is also associated with strong auroral intensities in the other auroral bands. In Figure 5.10 the 557.7 nm displays intensities of > 10 kR, which from the strong 427.8 nm line also is associated with a significant precipitated energy flux. This is consistent with the presence of the isotropic high-energy particles.

In the prenoon and morning sector (far outside the optical field-of-view) several other borders are observed; the >30 keV electron trapping boundary around 11:07:30 UT (1113 MLT, 79.0˚ ILAT), the 30-80 keV and 80-250 keV proton trapping boundaries at 11:08:30 UT (1022 MLT, 77.6˚ ILAT), the magnetosheath electron cutoff at 11:08:36 UT

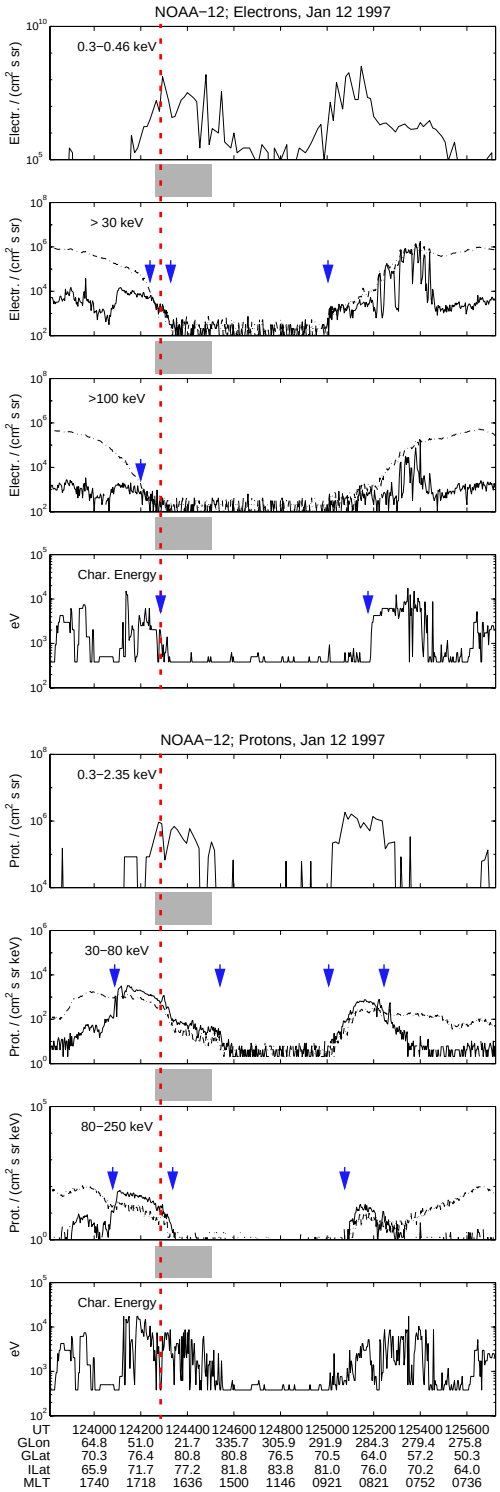

FIGURE 5.24 NOAA-12 particle observations from the fourth Svalbard pass. Border: **Sheath electron onset**.

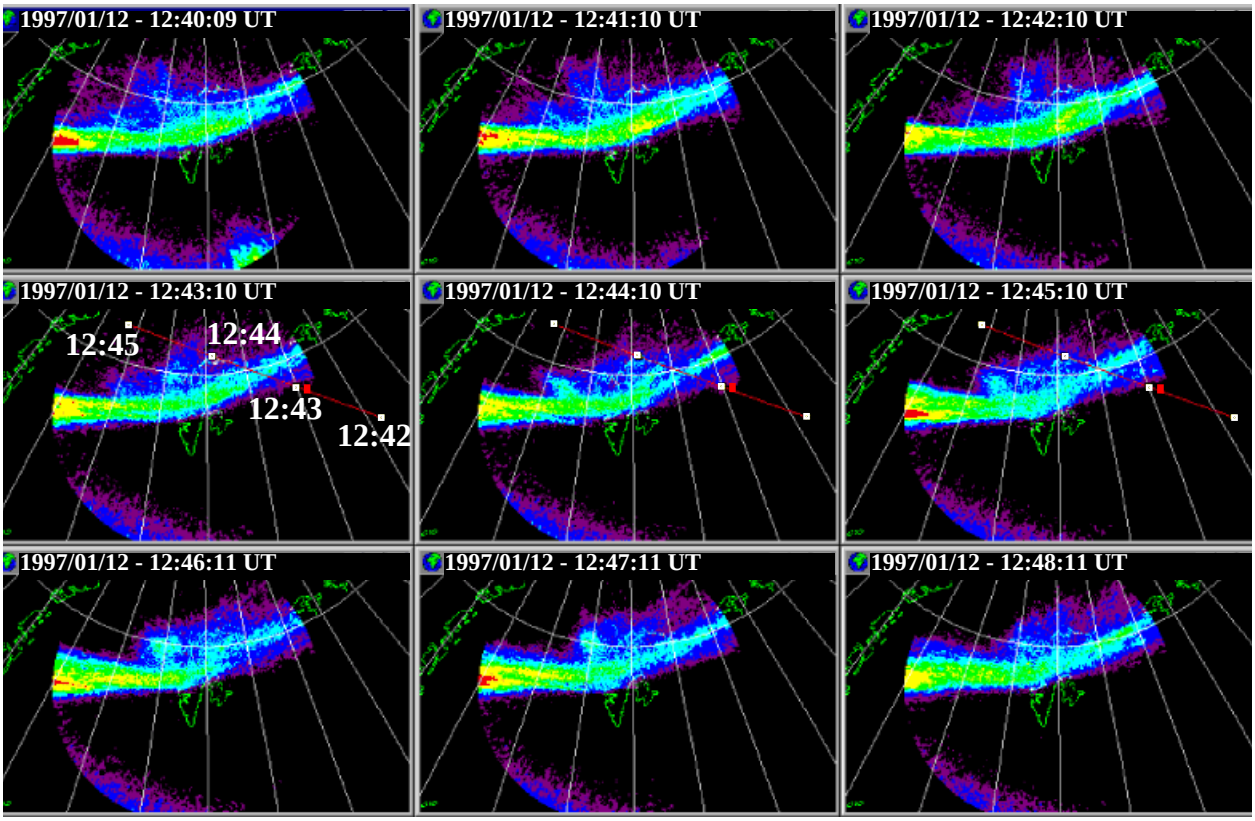

FIGURE 5.25 630.0 nm UiO/UNIS ASC images from the Auroral Station 12:40:09 UT to 12:48:11 UT January 12 1997. The images are projected to 250 km altitude, using a pseudo colour table, where red is maximum and blue minimum intensity.

(1017 MLT, 77.4˚ ILAT), and the 30-80 keV proton isotropy boundary at 11:09:18 UT (0949 MLT, 76.1˚ ILAT).

5.6.4 The Fourth Pass (12:42-12:45 UT)

The next NOAA-12 pass over Svalbard at 12:42 to 12:45 UT is displayed in Figure 5.24. The corresponding UiO/UNIS ASC TV images are displayed in Figure 5.25. Some useful footprint coordinates, marked in the middle row of Figure 5.25, are:

- 12:42:00 UT (1718 MLT, 71.7˚ ILAT)
- 12:43:00 UT (1701 MLT, 74.5˚ ILAT)
- 12:44:00 UT (1636 MLT, 77.2˚ ILAT)
- 12:45:00 UT (1559 MLT, 79.7˚ ILAT)

Here the NOAA-12 satellite also was moving towards higher latitudes through the optical field-of-view, where only one border is seen:

- **12:42:52 UT** (1704 MLT, 74.1˚ ILAT)

A fall in the characteristic electron energy gives this **equatorward boundary of the magnetosheath electrons**[***]. So, all the optical signatures in Figure 5.25 is poleward of this border. In fact, just poleward of this boundary a maximum i seen in the 0.3-0.46 keV magnetosheath electrons (Panel 1). From Figure 5.25

[***] The fall in the characteristic electron energy is flipping. Thus, the most poleward dropout has been chosen. The satellite skimming along a border may give raise to the flipping.

this precipitation maximum matches the maximum in the 630.0 nm aurora.

The magnetosheath electron cutoff (12:42:52 UT) was also poleward of both the >30 keV electron isotropy boundary at 12:42:24 UT (1712 MLT, 72.8˚ ILAT), the >100 keV electron isotropy boundary at 12:42:06 UT (1717 MLT, 72.0˚ ILAT), the 30-80 keV proton isotropy boundary at 12:41:02 UT (1730 MLT, 68.9˚ ILAT) and the 80-250 keV proton isotropy boundary at 12:40:52 UT (1732 MLT, 68.5˚ ILAT). Poleward of all these borders the fluxes of high-energy electrons were very low (near the lower threshold level), while a significant flux of high-energy protons was present. Just poleward of the magnetosheath electron cutoff an extra border was crossed; the >30 keV electron and 80-250 keV proton trapping boundaries at 12:43:10 UT (1658 MLT, 75.0˚ ILAT). The 30-80 keV proton flux had an abrupt fall at the same time, but its trapping boundary was not reached before 12:45:26 UT (1537 MLT, 80.7˚ ILAT).

From Figure 5.25 this event looks very stable in time, and combining the event 4 in Figure 5.14 and Figure 5.10 (630.0 nm) this is confirmed. The poleward boundary of the 630.0 nm is very stable ~ 60˚ north of zenith and does not move much about this event. The 557.7 nm line in Figure 5.10, however, display a poleward motion about the event, although the precipitating energy flux (427.8 nm) is far from intense.

A 25 min. IMF time delay gives the matching solar wind parameters observed by Wind around 12:18 UT. At 12:18 UT the IMF was (-2, 0, 1) nT GSE, and the clock angle was in CAR 1, see Figure 5.1. Thus, the IMF was northward. At this magnetic local time (1600-1700 MLT) the question also rises whether the ionospheric propagation delay T_{is}

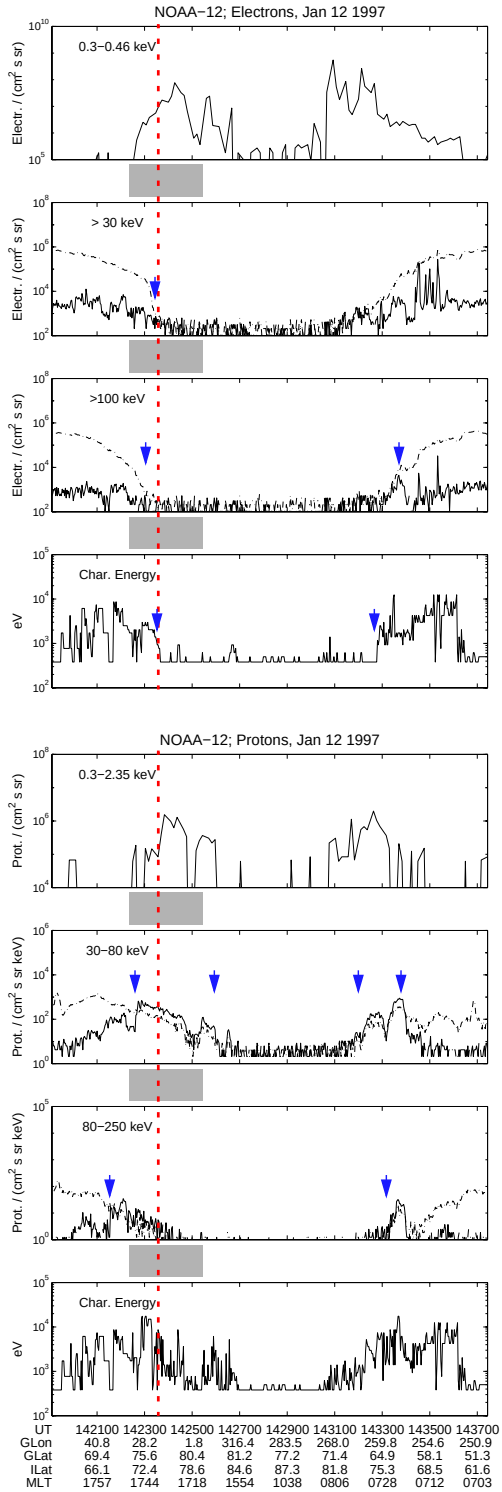

FIGURE 5.26 NOAA-12 particle observations from the fifth Svalbard pass. Main border: **Sheath electron onset**.

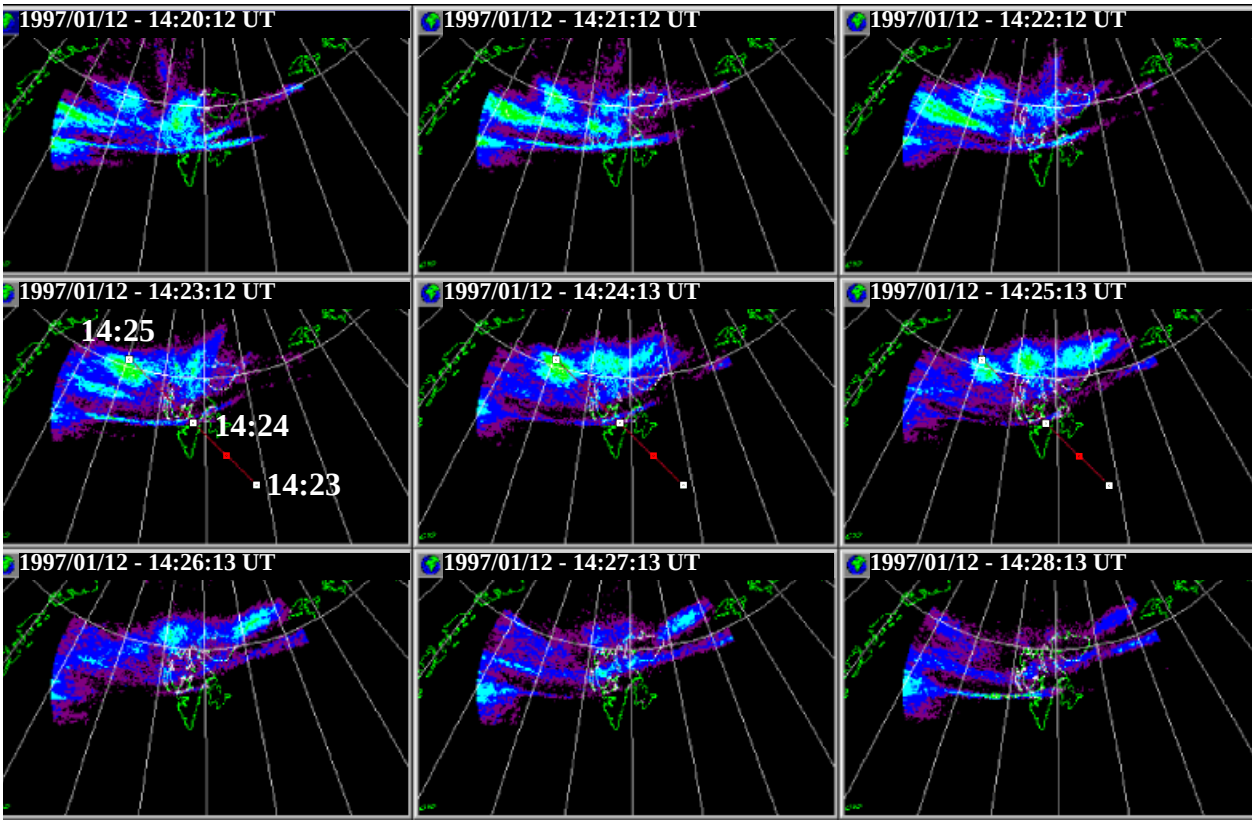

FIGURE 5.27 630.0 nm UiO/UNIS ASC images from the Auroral Station 14:20:12 UT to 14:28:13 UT January 12 1997. The images are projected to 250 km altitude, using a pseudo colour table, where red is maximum and blue is minimum intensity.

becomes important (i.e. ~ 10-15 min.) and must perhaps be included. However, since the solar wind parameters are very stable and do not change significantly before and after this time, just ignoring T_{is} gives the same results.

Some other interesting borders are also observed far outside the field-of-view. In the morning sector the trapping boundaries was crossed in the following way: >30 keV electrons at 12:50:04 UT (0918 MLT, 80.7˚ ILAT), 30-80 keV protons around 12:50:18 UT (0909 MLT, 80.3˚ ILAT) and 80-250 keV protons at 12:51:06 UT (0842 MLT, 78.4˚ ILAT). The >100 keV electron trapping boundary, the >30 & >100 keV electron isotropy boundaries and the 80-250 keV proton isotropy boundary are very hard to distinguish. The magnetosheath electron cutoff was traversed at 12:51:54 UT (0823 MLT, 76.2˚ ILAT), and the 30-80 keV proton isotropy boundary at 12:52:42 UT (0809 MLT, 74.0˚ ILAT).

5.6.5 The Fifth Pass (14:23-14:25 UT)

The last NOAA-12 pass over Svalbard on January 12 1997 is shown in Figure 5.26. UiO/UNIS ASC TV images around this satellite pass are displayed in Figure 5.27. The footprint coordinates, marked in the middle row of Figure 5.27, are:

- 14:23:00 UT (1744 MLT, 72.4˚ ILAT)
- 14:24:00 UT (1734 MLT, 75.5˚ ILAT)
- 14:25:00 UT (1718 MLT, 78.6˚ ILAT)

From these coordinates NOAA-12 now moves almost straight poleward along the same magnetic local time, where only one border within the optical field-of-view is seen in Figure 5.26 in the characteristic electron energy:

- 14:23:30 UT (1740 MLT, 73.9˚ ILAT)

This border is indicated in Figure 5.26 by a vertical guide line and by a red spot in Figure 5.27. This magnetosheath electron onset is also very close to and just poleward of the electron isotropy and trapping boundaries. The >30 keV electron isotropy and trapping boundary was crossed around 14:23:22 UT (1741 MLT, 73.5˚ ILAT), and the >100 keV electron isotropy and trapping boundary around 14:23:00 UT (1744 MLT, 72.4˚ ILAT). The 30-80 keV proton isotropy boundary at 14:22:42 UT (1747 MLT, 71.4˚ ILAT) and the 80-250 keV proton isotropy boundary at 14:21:34 UT (1754 MLT, 67.9˚ ILAT) were even further equatorward.

All the 630.0 nm emissions took place well poleward of both these borders, where only low-energy electrons and protons including 30-80 keV protons were present and the high-energy electron absent. The flux of these high-energy 30-80 keV protons also decreased vs. increasing latitude. Their trapping boundary was first reached at 14:25:58 UT (1651 MLT, 72.4˚ ILAT).

From Figure 5.27, Figure 5.15 and Figure 5.11 this event 5 was not as stable in time as event 4. The auroral activity had been very low for a long time (about 1 hour), before a structure appeared around 14:20 UT. This multi-patch aurora reached its maximum intensity during this NOAA-12 pass and faded some minutes later. This event was also associated with some 557.7 nm intensity (>5 kR), however, the 427.8 nm line did not show significant energy flux being precipitated.

A 25 min. IMF time delay gives the interplanetary conditions observed by Wind around 14:00 UT. At 14:00 UT the IMF was (-4, -1, 2) nT, see Figure 5.1. The clock angle was ~ 40˚ and in CAR 1. As for the last event, ignoring the T_{is} makes no difference, since the solar wind parameters remained nearly constant for a longer period about this time (except some few and very sporadic excursion of the clock angle to CAR 2 on 1 min. time scales).

In the morning sector some extra borders are seen in the particle spectra; the 30-80 keV proton trapping boundary at 14:32:12 UT (0739 MLT, 77.9˚ ILAT), the magnetosheath electron cutoff at 14:32:48 UT (0730 MLT, 76.0˚ ILAT), the 80-250 keV proton trapping boundary at 14:33:20 UT (0724 MLT, 74.2˚ ILAT), the >100 keV electron isotropy boundary at 14:33:42 UT (0721 MLT, 73.0˚ ILAT) and the 30-80 keV proton isotropy boundary at 14:34:00 UT (0719 MLT, 71.9˚ ILAT). The other boundaries; the >30 keV electron isotropy and trapping boundaries, the >100 keV electron trapping boundary and the 80-250 keV proton isotropy boundary, are very hard to determine in this magnetic local time sector.

5.7 Polar - PIXIE

Now an event detected by the PIXIE[†††] X-ray camera on-board the Polar satellite is very briefly presented (Figure 5.28). The purpose is to show the lack of severe precipitation of energetic electrons in the high latitude dayside cusp/cleft region. The energetic electron precipitation is instead very typical in the night and morning sectors on closed magnetic field

[†††] Polar Ionospheric X-ray Imaging Experiment. For a complete description of PIXIE, see [Imhof et al., 1995]

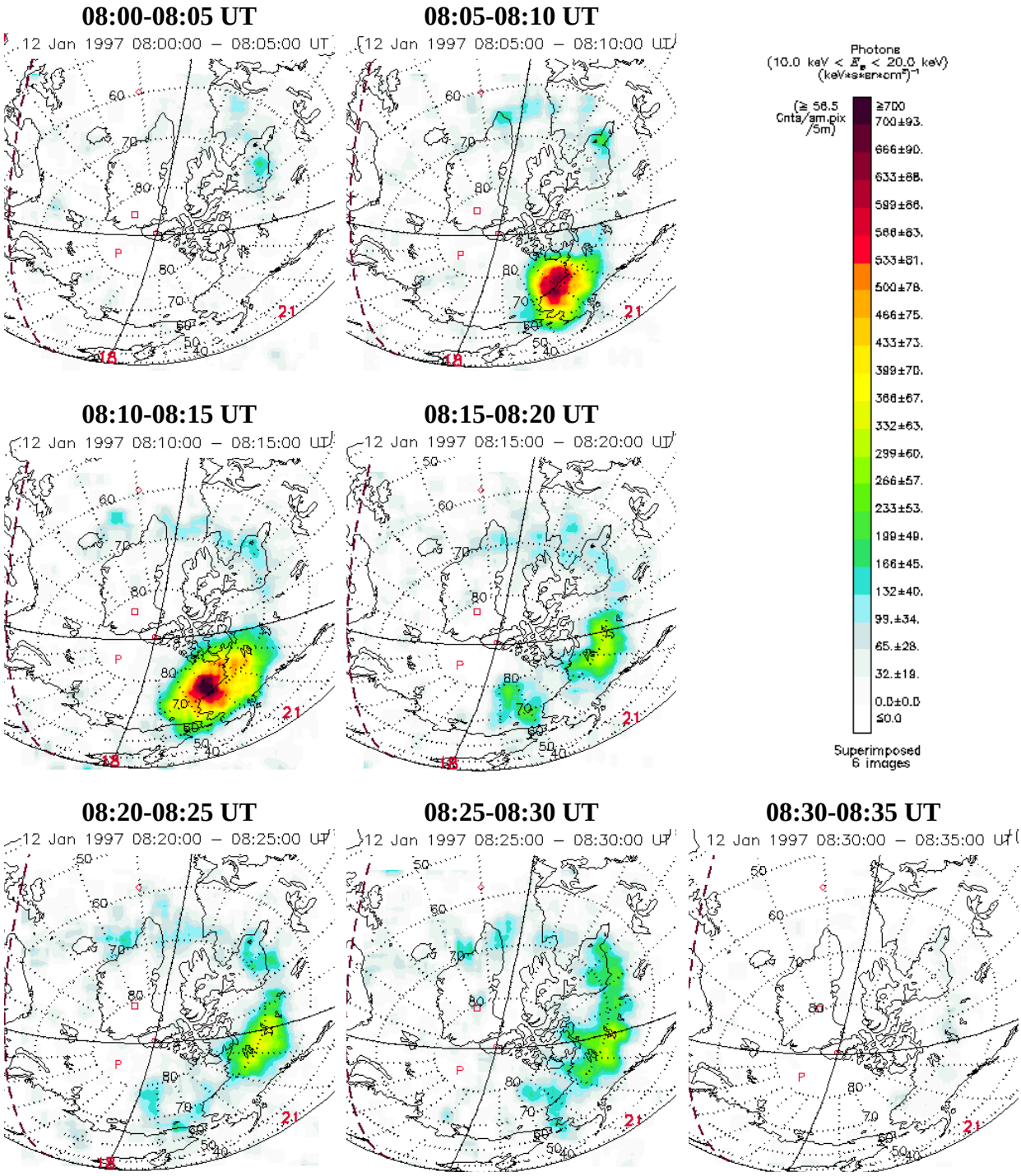

FIGURE 5.28 10-20 keV X-ray aurora from the PIXIE camera on-board the Polar satellite, 08:00 to 08:35 UT on January 12 1997. Each image, a 5 min. exposure, is projected onto a MLT/ CGMLAT grid (dotted lines), where the 00, 06, 12 and 18 meridians are marked by solid lines. The terminator (dashed line) and magnetic noon are to the left. Also indicated are the geographic North Pole **P**, the sub-satellite point ◊ and the centre of the field-of-view ❑.

lines. Due to the magnetic drift these energetic electrons drift westward from an injection region near magnetic midnight.

5.7.1 Observations Related to the January 12 Event

Figure 5.28 shows a sequence of PIXIE 10-20 keV X-ray images from 08:00 to 08:35 UT on January 12 1997. Each image is superposed onto a MLT/CGMLAT grid, cf. [Thorsen, 1998]. The terminator, the border between the sunlit and dark ionosphere, is marked by the heavy dashed line in the left edge of each display, so magnetic noon is to the left. The meridians 00, 06, 12 and 18 MLT are marked by solid lines, while the others are dotted. The magnetic latitude (CGM) is plotted from 40-80˚ CGMLAT in 10˚ steps.

A strong intensification in the X-ray aurora is observed in the 21 MLT sector from 08:05 to 08:15 UT. This intensity then slowly decrease and the X-ray aurora starts to evolve eastwards towards the morning side. No significant flux of X-rays was detected near Svalbard at this time, consistent with Svalbard being within the cusp/cleft region (~ 75˚ CGMLAT, ~ 1115-1145 MLT). In the cusp the average electron energy and the fluxes of precipitating energetic electrons are typically very low [e. g. Newell et al., 1991b and others]. However, Newell et al. did not measure electrons above 30 keV, but that contribution is probably very low, since the cusp is often defined to originate from direct entry of low-energy magnetosheath plasma along open magnetic field lines.

This X-ray event is the most active part of the event studied by [Bjordal et al., 1997]. From the AE/A0 indices (Figure 5.2) they found the start of a geomagnetic substorm, with negative bays near magnetic midnight, at 07:28 UT, which also corresponds very well with the equatorward motion seen in the dayside MSP data from Longyearbyen (e.g. Figure 5.6 to Figure 5.8).

5.8 Summary

Having presented an optical overview of January 12 1997, with special focus on the time about the five NOAA-12 passes over Svalbard, it is time to summarize the observations and results.

First, a brief overview of both the solar wind parameters from Wind 06:00-16:00 UT and the AE indices were presented as a framework for the discussion. The time delay from Wind to the noon ionosphere was calculated to be 25 min.

Secondly, meridian scanning photometer data from both Longyearbyen and Ny Ålesund was showed. The data was displayed in three different ways; traditional colour plot, traditional stack plot and projected onto a MLT/MLAT grid. In order to do this projection the altitudes of the auroral emissions had to be assumed. Therefore, a simple estimate (Figure 5.5) was made for the 557 nm and 630 nm emissions based on the MSP observations from Longyearbyen and Ny Ålesund. This was in reasonable good agreement with Figure 5.4, taken from [Carlson Jr. and Egeland, 1995]. The projections using these altitudes (Figure 5.6 and Figure 5.7) also gave more or less the same image, indicating the assumed heights was not too wrong. Taking the calculated time delay into account, a fair correspondence was found between the north-south motion of the aurora and the IMF clock angle, especially the equatorward displacement around 07:30-09:00 UT.

Subsequently, a sequence of All-Sky images from 07:00-17:00 UT was presented as an overview and a basis for the succeeding discussion of the five NOAA-12 passes over Svalbard. The first two passes took place during substorm activity (Figure 5.2), while the others were in the middle of quiet conditions.

Table 5.1 presents a brief review of the most clear particle borders (isotropy boundaries, trapping boundaries and magnetosheath electron cutoffs) identified in the satellite data at given UT, MLT and ILAT.

Table 5.2 summarizes the groundbased and NOAA-12 particle observations during the five passes over Svalbard:

1. The first pass traversed the cusp and the LLBL (perhaps also the BPS equatorward of the LLBL). In the cusp, poleward of the first border, only particles of magnetosheath origin were detected, and the 630.0 nm emissions reached the maximum intensity. In the LLBL, between the two borders, particles of both magnetosheath and magnetosphere origin were measured, and the 630,0 nm emissions decreased in intensity moving away from the cusp. This event was also associated with a moving auroral form.
2. The second pass crossed the mantle, where particles of both magnetosheath and magnetosphere origin was detected poleward of the electron isotropy boundary and magnetosheath electron onset. This event was stable in time.
3. The third pass also crossed the aurora poleward of the magnetosheath electron onset, which was before NOAA-12 entered the field-of-view. This aurora was also characterized by the presence of particles of both magnetosheath and magnetosphere origin, however, the high-energy electron flux was low. The border within the field-of-view is the high-latitude cutoff in the 0.3-2.35 keV magnetosheath protons.
4. The fourth pass traversed a thin east-west elongated arc poleward of both the magnetosheath electron onset and the electron trapping boundary. A population of magnetosheath particles and magnetosphere protons (no magnetosphere electrons) was detected.
5. The fifth pass crossed a stable multi-patch aurora poleward of both the magnetosheath electron onset and the electron trapping boundary. This aurora was also associated with precipitation of magnetosheath particles and magnetosphere protons, (no magnetosphere electrons).

Finally, a sequence from the PIXIE camera on-board the Polar satellite of a X-ray aurora substorm event was introduced to illustrate the absence of severe energetic electron precipitation in the cusp/cleft region. This X-ray aurora was instead very active on the night and morning sides, and afterwards (not shown) some activity on the dayside at lower latitudes (60-70˚ CGMLAT).

In the next Chapter the conclusions of this thesis will be drawn, and planned future work will be pointed at.

NOAA-12 Particle Borders		1	2	3	4	5
		UT MLT | ILAT	UT MLT | ILAT	UT MLT | ILAT	UT MLT | ILAT	UT MLT | ILAT
Electrons >30 keV	IB	07:37:38 1557 | 68.9˚	09:22:12 1445 | 75.8˚	11:02:40 1601 | 75.5˚	12:42:24 1712 | 72.8˚	14:23:22 1741 | 73.5˚
	TB	07:38:48 1521 | 71.7˚	-	11:04:22 1445 | 78.6˚	12:43:10 1658 | 75.0˚	14:23:22 1741 | 73.5˚
	TB	07:42:54 (1218 | 75.1˚)	-	11:07:30 1113 | 79.0˚	12:50:04 0918 | 80.7˚	-
	IB	07:44:44 1059 | 72.7˚	09:25:10 1208 | 76.4˚	-	-	-
Electrons >100 keV	IB	07:37:26 1603 | 68.3˚	09:21:34 1512 | 74.9˚	11:02:20 1611 | 74.8˚	12:42:06 1717 | 72.0˚	14:23:00 1744 | 72.4˚
	TB	07:38:48 1521 | 71.7˚	-	-	-	14:23:00 1744 | 72.4˚
	TB	-	-	-	-	-
	IB	07:44:44 1059 | 72.7˚	09:25:30 1150 | 76.1˚	-	-	14:33:42 0721 | 73.0˚
Protons 30-80 keV	IB	07:37:38 1557 | 68.9˚	09:21:16 1524 | 74.4˚	-	12:41:02 1730 | 68.9˚	14:22:42 1747 | 71.4˚
	TB	07:40:00 1435 | 73.9˚	-	11:04:12 1454 | 78.3˚	12:45:26 1537 | 80.7˚	14:25:58 1651 | 81.6
	TB	07:42:54 (1218 | 75.1˚)	-	11:08:30 1022 | 77.6˚	12:50:18 0909 | 80.3˚	14:32:12 0739 | 77.9˚
	IB	07:44:44 1059 | 72.7˚	09:25:58 1127 | 75.5˚	11:09:18 0949 | 76.1˚	12:52:42 0809 | 74.0˚	14:34:00 0719 | 71.9˚
Protons 80-250 keV	IB	07:37:26 1603 | 68.3˚	09:20:06 1603 | 71.8˚	-	12:40:52 1732 | 68.5˚	14:21:34 1754 | 67.9˚
	TB	07:38:48 1521 | 71.7˚	-	-	12:43:10 1658 | 75.0˚	-
	TB	-	-	11:08:30 1022 | 77.6˚	12:51:06 0842 | 78.4˚	14:33:20 0724 | 74.2˚
	IB	-	09:26:34 1059 | 74.6˚	-	-	-
Magnetosheath Electron Cutoff		07:39:38 1450 | 73.3˚	09:21:24 1519 | 74.6˚	11:02:40 1601 | 75.5˚	12:42:52 1704 | 74.1˚	14:23:30 1740 | 73.9˚
		07:44:44 1059 | 72.7˚	09:25:30 1150 | 76.1˚	11:08:36 1017 | 77.4˚	12:51:54 0823 | 76.2˚	14:32:48 0730 | 76.0˚

TABLE 5.1 A brief summary of particle borders (UT, MLT & ILAT) the found in the NOAA-12 observations during the five satellite passes on January 12 1997. The isotropy boundaries (**IB**), trapping boundaries (**TB**) and the magnetosheath electron cutoffs are given.

Events January 12 1997		1	2	3	4	5
		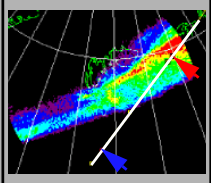	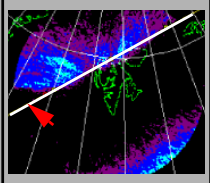	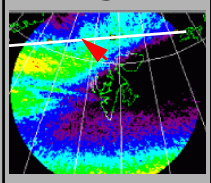	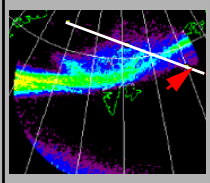	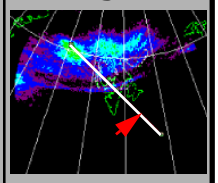
Time	**UT**	**07:42-07:45**	**09:23-09:26**	**11:03-11:06**	**12:42-12:45**	**14:23-14:25**
	MLT	1000-1230	1200-1400	1330-1600	1530-1730	1630-1900
Clock Angle		CAR 3	CAR 1	CAR 3	CAR 1	CAR 1
IMF [nT]		(-1, 3, -6)	(-3, 5, 1)	(2, 2, -3)	(-2, 0, 1)	(-4, -1, 2)
Sheath	**Electr.**	Y	Y	Y	Y	Y
	Ions	Y	Y	Y	Y	Y
Sphere	**Electr.**	N / Y	Y	weak	N	N
	Ions	N / Y	Y	Y	Y	Y
Equatorward Borders		**1.** 1218 MLT, 75.1˚ ILAT **2.** 1059 MLT, 72.7˚ ILAT	1150 MLT, 76.1˚ ILAT	1445 MLT, 78.6˚ ILAT	1704 MLT, 74.1˚ ILAT	1740 MLT, 73.9˚ ILAT
MSP [nm]	**630.0**	strong	strong	strong	strong	strong
	557.7	very strong spikes	very weak	very strong	strong	strong spikes
	427.8	strong	weak	strong	some	some
Auroral Position		south	north	north, expanding southward	north	north
Stable		poleward moving form	Y	Y (?)	Y	Y
Source Regions		**1.** Cusp (?) **2.** LLBL (?)	Mantle (?)		BPS (?)	BPS (?)

TABLE 5.2 A summary of the observations during the five NOAA-12 passes over Svalbard on January 12 1997. (The **red** and **blue** coloured text matches the arrows in the image displays in the first row.)

Chapter 6

CONCLUSIONS

Summarize the observations,
draw the lines and point at future work

6.1 Results

The combination of particle observations from the NOAA-12 satellite and simultaneous groundbased observations from Svalbard has proved to be useful. The existing infrastructure at Svalbard, including the ideal geomagnetic position, makes Svalbard the natural centre for studies of the high-latitude dayside aurora. And, the NOAA satellites carry suitable instruments detecting particles in a wide energy range from 300 eV to several MeV. In fact, the new generation NOAA satellites from NOAA-15 (launched 1998) and onwards are even more flexible having a lower energy threshold (50 eV).

6.1.1 January 9-12 1997

An overview of the NOAA-12 observations during this CME event has been presented in Chapter 3. The satellite observations revealed a huge intensification in the fluxes of both trapped and precipitating particles on January 10. A good correspondence between the particle fluxes and the Dst index was also found. An equatorward displacement of the particle precipitation in the northern evening sector was consistent with a strongly negative IMF Bz component. The energetic protons showed the largest fluxes in the evening sector, while the energetic electrons dominated in the morning sector. This was explained by the magnetic drifts. The low-energy protons displayed the opposite pattern, which was explained by the $E \times B$ drift in the corotating electric field. An interhemispherical difference in the particle fluxes was found, where the southern (summer) hemisphere was dominating. This suggests the presence of a time of year effect, however, it needs to be further studied in a statistical study also including observations from other times of the year.

A problem of calculating the solar wind time delay from the Wind spacecraft to the ionosphere was encountered using the method of [Lockwood et al., 1989], so the formulae had to be redefined. And, the 80° high-energy MEPED proton detector showed a reduced efficiency vs. the 10° detector, which was

explained as radiation damage to the front window. The electron detector did not exhibit this.

6.1.2 January 12 1997

The overview of the observations in Chapter 3 and the brief review of the dayside aurora in Chapter 4 constituted the framework for a study of five NOAA-12 passes over Svalbard on January 12 1997 (Chapter 5) in the noon and postnoon sector. These passes included different interplanetary conditions and the borders in the particle spectra were especially examined.

First, an overview of the groundbased optical observations were presented, using both the UiO/UNIS All-Sky camera and MSP in Longyearbyen and the MSP in Ny Ålesund. A new way of displaying MSP data was also suggested, and approximate emission altitudes were found using a simple automatic method.

The five NOAA-12 passes were briefly summarized in Table 5.1 and Table 5.2. The first pass crossed the cusp and the LLBL (perhaps also the BPS), while the second one traversed the mantle. The three other passes were in the postnoon sector and showed the 630.0 nm auroral structures to be primarily associated with precipitation of soft magnetosheath particles including high-energy ions (probably BPS candidates). All these satellite passes will be considered in more detail in order to be published.

6.2 Future Work

The software developed to analyze the NOAA-12 data is suitable for studies of other events too. Further event and statistical studies of the sources and losses in the ring current and the consistency with the Dst index, using the summary plots in Chapter 3, will give more knowledge about these important processes. Ring current studies using polar satellites (NOAA, Polar) combined with equatorial satellites (CRRES, GOES) are fruitful here. It would also be of great interest to estimate the precipitated energy flux based on the NOAA satellite observations.

The NOAA satellites can also be used in a statistical study of the particle source regions to create maps like [Newell and Meng, 1992; Newell and Meng, 1994]. Newell and Meng's data set was limited to field aligned particles in the 32 eV to 30 keV energy range only. Therefore, the contribution from the higher energy particles is not included. Newell and Meng have not studied the pitch angle dependency in the particle population either. The NOAA satellites are useful here, having a very wide energy range and an enormous data set available (more than 2 decades). It will also be very interesting to create energy spectrums (from 300 eV to ~ 1 MeV) vs. time from the MEPED and TED data. This is a much wider energy range than is covered by the DMSP satellites.

Today, the more large-scale patterns in the dayside aurora are thought to be reasonable well understood. The large scale currents (Region 1, Region 2 and cusp/mantle) and the associated large-scale ionospheric flows are accepted by most researchers. However, the more small scale structures are less studied as noted by [Yamauchi et al., 1998]. A future study looking at these phenomena also including data from e.g. the Polar and Fast satellites is planned.

Appendix A

ABBREVIATIONS

Often abbreviations are used without any further explanation. However, sometimes this causes confusion, so here is a listing of some of the acronyms used in this thesis:

Abbreviation	Explanation
3-DP	3-D Plasma experiment
AE	Auroral Electrojet
ASC	All-Sky Camera
BPS	Boundary Plasma Sheet
CAR	Clock Angle Region (see definition in Section 3.2.2)
CDEM	Continuous Dynode Electron Multiplier
CME	Coronal Mass Ejection
CPS	Central Plasma Sheet
CRB	Convection Reversal Boundary
DE	Dynamics Explorer
DMSP	Defence and Meteorological Satellite Program
DPU	Data Processing Unit

EISCAT	European Incoherent SCATter facility
EISCAT ESR	EISCAT Svalbard Radar
ESA	Electrostatic Analyser
ESRO	European Science Research Organisation
ESRO IA	ESRO 1 Aurorae
ESRO IB	ESRO 1 Boreas
FTE	Flux Transfer Events
GLAT	Geographic LATitude
GLON	Geographic LONgitude
GSE	The Geocentric Solar Ecliptic coordinate system, see [Hapgood, 1992]
ILAT	Invariant LATitude
IMF	The Interplanetary Magnetic Field
IR	InfraRed radiation
ISSE	International Sun Earth Explorer
ISTP	International Solar Terrestrial Physics program
LASCO	Large Angle Spectrometric COronagraph
LLBL	Low Latitude Boundary Layer
NATO	North Atlantic Treaty Organization
NOAA	National Oceanic and Atmospheric Administration
NSSDC	National Space Science Data Center
MEPED	Medium Energy Proton and Electron Detector
MFI	Magnetic Field Investigation
MLT	Magnetic Local Time
MSP	Meridian Scanning Photometer
PC	Personal Computer
PIXIE	Polar Ionospheric X-ray Imaging Experiment

SEM	Space Environment Monitor
SOHO	The SOlar and Heliospheric Observatory
sr	steradian
SSD	Solid State Detector
SWE	Solar Wind Experiment
TED	Total Energy Detector
TIROS	Television and InfraRed Observation Satellite
UiB	University of Bergen
UiO	University of Oslo
UNIS	University Courses on Svalbard
UT	Universal Time
UV	UltraViolet radiation
WWW	World Wide Web

Appendix B

CONVERSION

A description of the procedure converting from MSP elevation angle to equivalent magnetic latitude

B.1 From Elevation Angle to Latitude

By making altitude assumptions of the auroral emissions one is able to convert from elevation angles to latitudes and longitudes. Given the geomagnetic coordinates at a station and assuming the optical emissions to take place only in a very thin curved layer, the calculations are as follows for a curved Earth surface.

Figure B.1 shows a sketch of the trigonometric transformation. The thick curved solid line is the Earth's surface, and the dashed one is the assumed very thin layer of optical emissions in *h* km altitude, e.g. 250 km for 630 nm emissions. λ is the angle between the station and the emission as seen from the centre of the Earth, at a given MSP elevation angle θ. R_e is 6370 km, the radius of the Earth. *a*, *b*, *c*, and *d* are trigonometric parameters used in the calculations:

$$a^2 = R_e^2 + (b+c)^2 - 2R_e(b+c)\cos\lambda \qquad \textbf{(B.1)}$$

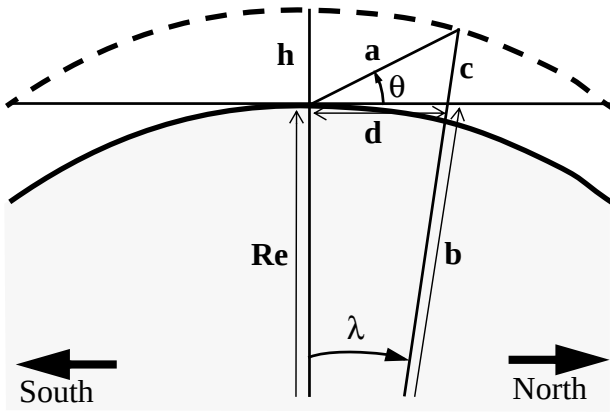

FIGURE B.1 A sketch of the trigonometric transformation, from elevation angle to invariant latitude, see text.

$$b = \frac{R_e}{\cos\lambda} \qquad \textbf{(B.2)}$$

$$c + b = R_e + h \qquad \textbf{(B.3)}$$

$$d = R_e\tan\lambda \qquad \textbf{(B.4)}$$

$$c^2 = d^2 + a^2 - 2ad\cos\theta \qquad \textbf{(B.5)}$$

Equation B.3 is inserted in Equation B.1, and Equation B.2, Equation B.3 and Equation B.4 are combined with Equation B.5 giving:

$$a^2 = {R_e}^2 + (R_e + h)^2 - 2R_e(R_e + h)\cos\lambda \quad \textbf{(B.6)}$$

$$\left(R_e + h - \frac{R_e}{\cos\lambda}\right)^2 = (R_e\tan\lambda)^2 + a^2 - 2aR_e\tan\lambda\cos\theta \quad \textbf{(B.7)}$$

Using both Equation B.6 and Equation B.7 gives:

$$\left(R_e + h - \frac{R_e}{\cos\lambda}\right)^2 \quad \textbf{(B.8)}$$
$$= (R_e\tan\lambda)^2 + {R_e}^2 + (R_e + h)^2 - 2R_e(R_e + h)\cos\lambda - 2\sqrt{{R_e}^2 + (R_e + h)^2 - 2R_e(R_e + h)\cos\lambda} \times R_e\tan\lambda\cos\theta$$

which may be simplified to:

$$(R_e + h) \times \left(\frac{1}{\cos\lambda} - \cos\lambda\right) = \tan\lambda\cos\theta \times \sqrt{R_e^2 + (R_e + h)^2 - 2R_e(R_e + h)\cos\lambda} \quad \textbf{(B.9)}$$

Quadrating both sides and collecting terms, leads to

$$\cos^2\lambda - 2\left(\frac{R_e}{R_e + h}\right)\cos^2\theta\cos\lambda + \left(\frac{R_e}{R_e + h}\right)^2\cos^2\theta - \sin^2\theta = 0 \quad \textbf{(B.10)}$$

which has the two solutions:

$$\lambda = \operatorname{acos}\left\{\frac{R_e}{R_e + h}\left[\cos^2\theta \pm |\sin\theta| \sqrt{\left(\frac{R_e + h}{R_e}\right)^2 - \cos^2\theta}\right]\right\} \quad \textbf{(B.11)}$$

A careful examination gives:

$$\lambda = \begin{cases} \operatorname{acos}\left\{\frac{R_e}{R_e + h}\left[\cos^2\theta + |\sin\theta| \sqrt{\left(\frac{R_e + h}{R_e}\right)^2 - \cos^2\theta}\right]\right\} & (0° \le \theta \le 90°) \\ -\operatorname{acos}\left\{\frac{R_e}{R_e + h}\left[\cos^2\theta + |\sin\theta| \sqrt{\left(\frac{R_e + h}{R_e}\right)^2 - \cos^2\theta}\right]\right\} & (90° < \theta \le 180°) \end{cases} \quad \textbf{(B.12)}$$

where θ is the elevation angle taken from the northern horizon, R_e is the Earth's radius and h is the assumed height of the auroral emissions.

Having found the angle between the station and the emissions as seen from the centre of Earth, the equivalent magnetic latitude may be calculated. Since the two MSPs in Longyearbyen and Ny Ålesund are approximately scanning along the local magnetic meridian, the transformation is as follows:

$$\Lambda_{eq} = \Lambda + \lambda \qquad \textbf{(B.13)}$$

Here Λ is the magnetic latitude of the given station (75.1^o CGM in Longyearbyen and 76.0^o CGM in Ny Ålesund), and λ follows directly from evaluation of Equation B.12. During the transformation the magnetic longitude or MLT at each elevation angle is just the same as that of the station, because the scanning along a meridian.

This procedure does not take into account the effect of a varying effective thickness of the emission layer, as seen with the MSP, as the elevation angle changes from 0^o through 90^o to 180^o. Therefore the intensities near the horizon (those farthest from the station in magnetic latitude) become too high. However, the positioning of an auroral structure in magnetic latitude is correct if the height assumption is valid.

Equation B.12, as given here, is valid both in the northern and southern hemisphere, though only the northern is used here. There is only one problem; when the station is too close to one of the magnetic poles. Then the projection may become incorrect, $|\Lambda + \lambda| > 90°$. This is however not any problem at Longyearbyen and Ny Ålesund for normal emission altitudes.

References

During my studies the World Wide Web (WWW) has been a very important source to get information. However, the Internet is a continuously changing medium, so the addresses (URL) are often modified. It is therefore not constructive to list the URLs. Instead, some keywords (indicating where the information was taken from) are mentioned in the text.

Printed material (books, papers, theses and reports) cited in the text:

Baker, K. B., Greenwald, R. A., Ruohoniemi, J. M., Dudeney, J. R., Pinnock, M., Newell, P. T., Greenspan, M. E., and Meng, C.-I.. Simultaneous HF-radar and DMSP observations of the cusp. *Geophys. Res. Lett.*, **17** (11), 1869–1872, 1990.

Berg, L. E. and Søraas, F.. Observations suggesting weak pitch angle diffusion of protons. *J. Geophys. Res.*, **77** (34), 6708–6715, 1972.

Bjordal, J., Brittnacher, M., Chenette, D. L., McKenzie, D. L., Parks, G. K., Stadsnes, J., Thorsen, E., and Østgaard, N., 1997. X-ray and optical auroral imaging from the POLAR satellite. In **Wold, H., Hansen, G., Hoppe, U.-P., Måseide, K., and Søraas, F.**, editors, *Proceedings of The 24th Annual European Meeting on Atmospheric Studies by Optical Methods*, pages 96–107, Andenes, Norway. Sentraltrykkeriet A/S, Bodø. ISBN 82-994583-0-7.

Burch, J. L., Reiff, P. H., Heelis, R. A., Winningham, J. D., Hanson, W. B., Gurgiolo, C., Menietti, J. D., Hoffman, R. A., and Barfield, J. N.. Plasma injection and transport in the mid-altitude polar cusp. *Geophys. Res. Lett.*, **9** (9), 921–924, 1982.

Carlson Jr., H. C. and Egeland, A., 1995. The aurora and the auroral ionosphere. In **Kivelson, M. G. and Russell, C. T.**, editors, *Introduction to space physics*, chapter 14, pages 459–500. Cambridge University Press, New York, USA.

Cogger, L. L., Murphree, J. S., Ismail, S., and Anger, C. D.. Characteristics of dayside 5577Å and 3914Å aurora. *Geophys. Res. Lett.*, **4** (10), 413–416, 1977.

Crooker, N., Joselyn, J. A., and Feynman, J., editors. *Coronal Mass Ejections*, volume 99 of *Geophysical Monograph Series*. American Geophysical Union, Washington.

Crooker, N. U. and Burke, W. J.. The cusp/cleft. *U.S. National Report to International Union of Geodesy and Geophysics 1987-1990, Rev. Geophys.*, **29**, 1017–1027, 1991.

Curran, D. B. and Goertz, C. K.. Particle distributions in a two-dimensional reconnec-

tion field geometry. *J. Geophys. Res.*, **94** (A1), 272–286, 1989.

Eastman, T. E. and Frank, L. A.. Observations of high-speed plasma flow near the Earth's magnetopause: Evidence for reconnection? *J. Geophys. Res.*, **87** (A4), 2187–2201, 1982.

Eastman, T. E., Popielawska, B., and Frank, L. A.. Three-dimensional plasma observations near the outer magnetospheric boundary. *J. Geophys. Res.*, **90** (A10), 9519–9539, 1985.

Erlandson, R. E., Zanetti, L. J., Potemra, T. A., and Bythrow, P. F.. IMF By dependence of region 1 Birkeland currents near noon. *J. Geophys. Res.*, **93** (A9), 9804–9814, 1988.

Evans, D. S., 1985. The characteristics of a persistent auroral arc at high latitude in the 1400 MLT sector. In **Holtet, J. A. and Egeland, A.**, editors, *The Polar Cusp*, pages 99–109. D. Reidel Publishing Company, Dordrecht, Holland.

Fälthammar, C.-G., 1973. Motion of Charged Particles in the Magnetospere. In **Egeland, A., Holter, Ø., and Omholt, A.**, editors, *Cosmical Geophysics*, pages 121–142. Universitetsforlaget, Oslo, Norway.

Feldstein, Y. I. and Starkov, G. V.. Dynamics of auroral belt and polar geomagnetic disturbances. *Planet. Space Sci.*, **15**, 209–229, 1967.

Frank, L. A.. Plasma in the Earth's polar magnetosphere. *J. Geophys. Res.*, **76** (22), 5202–5219, 1971.

Gosling, J. T., Thomsen, M. F., Bame, S. J., Onsager, T. G., and Russell, C. T.. The electron edge of the low latitude boundary layer during accelerated flow events. *Geophys. Res. Lett.*, **17** (11), 1833–1836, 1990.

Gussenhoven, M. S., Hardy, D. A., and Carovillano, R. L., 1985. Average electron precipitation in the polar cusps, cleft and cap. In **Holtet, J. A. and Egeland, A.**, editors, *The Polar Cusp*, pages 85–97. D. Reidel Publishing Company, Dordrecht, Holland.

Hapgood, M. A.. Space physics coordinate transformations: A user guide. *Planet. Space Sci.*, **40** (5), 711–717, 1992.

Harten, R. and Clark, K.. The design features of the GGS Wind and Polar spacecraft. *Space Sci. Rev.*, **71**, 23–40, 1995.

Hauge, R. and Søraas, F.. Precipitation of >115 keV protons in the evening and forenoon sectors in relation to the magnetic activity. *Planet. Space Sci.*, **23**, 1141–1154, 1975.

Heikkila, W. J., 1985. Definition of the cusp. In **Holtet, J. A. and Egeland, A.**, editors, *The Polar Cusp*, pages 387–395. D. Reidel Publishing Company, Dordrecht, Holland.

Heikkila, W. J. and Winningham, J. D.. Penetration of magnetosheath plasma to low altitudes through the dayside magnetospheric cusps. *J. Geophys. Res.*, **76** (4), 883–891, 1971.

Iijima, T. and Potemra, T. A.. Large-scale characteristics of field-aligned currents associated with substorms. *J. Geophys. Res.*, **83** (A2), 599–615, 1978.

Imhof, W. L., Spear, K. A., Hamilton, J. W., Higgins, B. R., Murphy, M. J., Pronko, J. G., Vondrak, R. R., McKenzie, D. L., Rice, C. J., Gorney, D. J., Roux, D. A., Williams, R. L., Stein, J. A., Bjordal, J., Stadsnes, J., Njøten, K., Rosenberg, T. J., Lutz, L., and Detrick, D.. The Polar Ionospheric X-ray Imaging Experiment (PIXIE). *Space Sci. Rev.*, **71**, 385–408, 1995.

Kremser, G. and Lundin, R.. Average spatial distributions of energetic particles in the midaltitude cusp/cleft region observed by Viking. *J. Geophys. Res.*, **95** (A5), 5753–5766, 1990.

Lepping, R. P., Acuña, M. H., Burlaga, L. F., Farrell, W. M., Slavin, J. A., Schatten, K. H., Mariani, F., Ness, N. F., Neubauer, F. M., Whang, Y. C., Byrnes, J. B., Kennon, R. S., Panetta, P. V., Scheifele, J., and Worley, E. M.. The Wind magnetic field investigation. *Space Sci. Rev.*, **71**, 207–229, 1995.

Lin, R. P., Anderson, K. A., Ashford, S., Carlson, C., Curtis, D., Ergun, R., Larson, D., McFadden, J., McCarthy, M., Parks, G. K., Rème, H., Bosqued, J. M., Coutelier, J., Cotin, F., D'Uston, C., Wenzel, K.-P., Sanderson, T. R., Henrion, J., Ronnet, J. C., and Paschmann, G.. A three-dimensional plasma and energetic particle investigation for the Wind spacecraft. *Space Sci. Rev.*, **71**, 125–153, 1995.

Liou, K., Newell, P. T., Meng, C.-I., Brittnacher, M., and Parks, G.. Synoptic auroral distribution: A survey using Polar ultraviolet imagery. *J. Geophys. Res.*, **102** (A12), 27197–27205, 1997a.

Liou, K., Newell, P. T., Meng, C.-I., Lui, A. T. Y., Brittnacher, M., and Parks, G.. Dayside auroral activity as a possible precursor of substorm onsets: A survey using Polar ultraviolet imagery. *J. Geophys. Res.*, **102** (A9), 19835–19843, 1997b.

Lockwood, M., Cowley, S. W. H., and Onsager, T. G.. Ion acceleration at both the interior and exterior Alfven waves associated with the magnetopause reconnection site: Signatures in cusp precipitation. *J. Geophys. Res.*, **101** (A10), 21501–21513, 1996.

Lockwood, M. and Moen, J.. Ion populations on open field lines within the dayside low-latitude boundary layer: theory and observations during a transient event. *Geophys. Res. Lett.*, **23** (21), 2895–2898, 1996.

Lockwood, M., Sandholt, P. E., Cowley, S. W. H., and Oguti, T.. Interplanetary magnetic field control of dayside auroral activity and the transfer of momentum across the dayside magnetopause. *Planet. Space Sci.*, **37** (11), 1347–1365, 1989.

Lundblad, J. Å., Søraas, F., and Aarsnes, K.. Substorm morphology of >100 keV protons. *Planet. Space Sci.*, **27**, 841–865, 1979.

Lundin, R.. Processes in the magnetospheric boundary layer. *Physica Scripta*, **T18**, 85–102, 1987.

Lundin, R.. Acceleration/heating of plasma on auroral field lines: Preliminary results from the Viking satellite. *Annales Geophysicae*, **6** (2), 143–152, 1988.

Lyons, L. R., Schulz, M., Pridmore-Brown, D. C., and Roeder, J. L.. Low-latitude boundary layer near noon: An open field line model. *J. Geophys. Res.*, **99** (A9), 17367–17377, 1994.

Lyons, L. R. and Williams, D. J.. *Quantitative aspects of magnetospheric physics*. "Geophysics and astrophysics monographs", edited by B. M. McCormac, Reidel publishing company, Dordrecht, Holland.

Marklund, G. T., Blomberg, L. G., Fälthammar, C.-G., Erlandson, R. E., and Potemra, T. A.. Signatures of the high-altitude polar cusp and dayside auroral regions as seen by the Viking electric field experiment. *J. Geophys. Res.*, **95** (A5), 5767–5780, 1990.

Marøy, S., 1977. "Et morfologi-studium av oppførselen til >100 keV protoner på høye

invariante bredder". Master's thesis, Physics Department, University of Bergen, Allegt. 55, 5007 Bergen, Norway. (In Norwegian).

Maynard, N. C. and Siscoe, G. L., 1998. Space weather - the practice of space physics. In **Moen, J., Egeland, A., and Lockwood, M.**, editors, *Polar Cap Boundary Phenomena*, pages 403–414, P. O. Box 17, 3300 AA Dordrecht, The Netherlands. NATO Scientific Affairs Division, Kluwer Academic Publishers. ISBN 0-7923-4976-8.

Maynard, N. C., Weber, E. J., Weimer, D. R., Moen, J., Onsager, T., Heelis, R. A., and Egeland, A.. How wide in magnetic local time is the cusp? An event study. *jgr*, **102** (A3), 4765–4776, 1997.

McDiarmid, I. B., Burrows, J. R., and Budzinski, E. E.. Particle properties in the day side cleft. *J. Geophys. Res.*, **81** (1), 221–226, 1976.

Mead, G. D. and Beard, D. B.. Shape of the geomagnetic field solar wind boundary. *J. Geophys. Res.*, **69** (7), 1169–1179, 1964.

Meng, C.-I., Lui, A. T. Y., Krimigis, S. M., Isamil, S., and Williams, D. J.. Spatial distribution of energetic particles in the distant magnetotail. *J. Geophys. Res.*, **86** (A7), 5682–5700, 1981.

Moen, J., Evans, D., Carlson, H. C., and Lockwood, M.. Dayside moving auroral transients related to LLBL dynamics. *Geophys. Res. Lett.*, **23** (22), 3247–3250, 1996.

Moen, J. and Lorentzen, D. A., 1997. On the registrated instruments at Nordlysstasjonen: Auroral season 1996-97, Preprint. Technical Report 1, The University Courses on Svalbard, N-9170 Longyearbyen, Norway.

Moen, J., Lorentzen, D. A., and Sigernes, F.. Dayside moving auroral forms and bursty proton auroral events in relation to particle boundaries observed by NOAA-12. *J. Geophys. Res.*, **103** (A7), 14855–14863, 1998.

Moen, J., Sandholt, P. E., Lockwood, M., Denig, W. F., Løvhaug, U. P., Lybekk, B., Egeland, A., Opsvik, D., and Friis-Christensen, E.. Events of enhanced convection and related dayside auroral activity. *J. Geophys. Res.*, **100** (A12), 23917–23934, 1995.

Murphree, J. S., Elphinstone, R. D., Hearn, D., and Cogger, L. L.. Large-scale high-latitude dayside auroral emissions. *J. Geophys. Res.*, **95** (A3), 2345–2354, 1990.

Newell, P. T., Burke, W. J., Meng, C.-I., Sanchez, E. R., and Greenspan, M. E.. Identification and observations of the plasma mantle at low altitude. *J. Geophys. Res.*, **96** (A1), 35–45, 1991a.

Newell, P. T., Burke, W. J., Sanchez, E. R., Meng, C. I., Greenspan, M. E., and Clauer, C. R.. The low-latitude boundary layer and the boundary plasma sheet at low altitude: Prenoon precipitation regions and convection reversal boundaries. *J. Geophys. Res.*, **96** (A12), 21013–21023, 1991b.

Newell, P. T., Lyons, K. M., and Meng, C.-I.. A large survey of electron acceleration events. *J. Geophys. Res.*, **101** (A2), 2599–2614, 1996.

Newell, P. T. and Meng, C. I.. The cusp and the cleft/boundary layer: Low-altitude identification and statistical local time variation. *J. Geophys. Res.*, **93** (A12), 14549–14556, 1988.

Newell, P. T. and Meng, C. I.. Mapping the dayside ionosphere to the magnetosphere according to particle precipitation characteristics. *Geophys. Res. Lett.*, **19** (6), 609–612, 1992.

Newell, P. T. and Meng, C. I.. Ionospheric projections of magnetospheric regions under low and high solar wind pressure conditions. *J. Geophys. Res.*, **99** (A1), 273–286, 1994.

Newell, P. T. and Meng, C. I., 1998. Open and closed low latitude boundary layer. In **Moen, J., Egeland, A., and Lockwood, M.**, editors, *Polar Cap Boundary Phenomena*, pages 91–101, P. O. Box 17, 3300 AA Dordrecht, The Netherlands. NATO Scientific Affairs Division, Kluwer Academic Publishers. ISBN 0-7923-4976-8.

Newell, P. T. and Sibeck, D. G.. By fluctuations in the magnetosheath and azimuthal flow velocity trancients in the dayside ionosphere. *Geophys. Res. Lett.*, **20** (16), 1719–1722, 1993.

Newell, P. T., Wing, S., Meng, C.-I., and Sigillito, V.. The auroral oval position, structure, and intensity of precipitation from 1984 onward: An automated on-line data base. *J. Geophys. Res.*, **96** (A4), 5877–5882, 1991c.

Ogilvie, K. W., Chornay, D. J., Fritzenreiter, R. J., Hunsaker, F., Keller, J., Lobell, J., Miller, G., Scudder, J. D., Sittler JR., E. C., Torbert, R. B., Bodet, D., Needell, G., Lazarus, A. J., Steinberg, J. T., Tappan, J. H., Mavretic, A., and Gergin, E.. SWE, a comprehensive plasma instrument for the Wind spacecraft. *Space Sci. Rev.*, **71**, 55–77, 1995.

Ogilvie, K. W., Fitzenreiter, R. J., and Scudder, J. D.. Observations of electron beams in the low-latitude boundary layer. *J. Geophys. Res.*, **89** (A12), 10723–10732, 1984.

Øieroset, M., Sandholt, P. E., Denig, W. F., and Cowley, S. W. H.. Northward interplanetary magnetic field cusp aurora and high-latitude magnetopause reconnection. *J. Geophys. Res.*, **102** (A6), 11349–11362, 1997.

Omholt, A.. *The optical aurora*. Springer-Verlag, Berlin.

Onsager, T. G., Kletzing, C. A., Austin, J. B., and MacKiernan, H.. Model of magnetosheath plasma in the magnetosphere: Cusp and mantle particles at low-altitudes. *Geophys. Res. Lett.*, **20** (6), 479–482, 1993.

Raben, V. J., Evans, D. S., Sauer, H. H., Sahm, S. R., and Huynh, M., 1995. TIROS/NOAA satellite environment monitor data archive documentation: 1995 update. Technical report, Space Environment Laboratory, Boulder, Colorado, National Technical Information Service, 5285 Port Royal Road, Springfield, VA 22161, USA.

Reiff, P. H., Hill, T. W., and Burch, J. L.. Solar wind plasma injection at the dayside magnetospheric cusp. *J. Geophys. Res.*, **82** (4), 479–491, 1977.

Rodger, A. S., 1998. Ionospheric signatures of magnetopause processes. In **Moen, J., Egeland, A., and Lockwood, M.**, editors, *Polar Cap Boundary Phenomena*, pages 115–125, P. O. Box 17, 3300 AA Dordrecht, The Netherlands. NATO Scientific Affairs Division, Kluwer Academic Publishers. ISBN 0-7923-4976-8.

Roederer, J. G.. *Dynamics of geomagnetically trapped radiation*. Springer Verlag, Berlin - Heidelberg - New York.

Sandholt, P. E.. Dayside auroral activity and magnetospheric boundary layer phenomena. *J. Geomag. Geoelectr.*, **42**, 711–726, 1990.

Sandholt, P. E., Deehr, C. S., Egeland, A., Lybekk, B., Viereck, R., and Romick, G. J.. Signatures in the dayside aurora of plasma transfer from the magnetosheath. *J.*

Geophys. Res., **91** (A9), 10063–10079, 1986.

Sandholt, P. E., Farrugia, C. J., Moen, J., and Cowley, S., 1997. Dayside auroral configurations as a function of the orientation of the interplanetary magnetic field. In **Wold, H., Hansen, G., Hoppe, U.-P., Måseide, K., and Søraas, F.**, editors, *Proceedings of the 24th Annual European Meeting on Atmospheric Studies of Optical Methods*, pages 194–202, Andenes, Norway. Sentraltrykkeriet A/S Bodø. ISBN 82-994583-0-7.

Sandholt, P. E., Farrugia, C. J., Moen, J., and Lybekk, B., 1998. The dayside aurora and its regulation by the interplanetary magnetic field. In **Moen, J., Egeland, A., and Lockwood, M.**, editors, *Polar Cap Boundary Phenomena*, pages 189–208, P. O. Box 17, 3300 AA Dordrecht, The Netherlands. NATO Scientific Affairs Division, Kluwer Academic Publishers. ISBN 0-7923-4976-8.

Sandholt, P. E., Farrugia, C. J., Øieroset, M., Stauning, P., and Cowley, S. W. H.. Auroral signature of lobe reconnection. *Geophys. Res. Lett.*, **23** (14), 1725–1728, 1996a.

Sandholt, P. E., Farrugia, C. J., Stauning, P., Cowley, S. W. H., and Hansen, T.. Cusp/cleft auroral forms and activities in relation to ionospheric convection: Responses to specific changes in solar wind and interplanetary magnetic field conditions. *J. Geophys. Res.*, **101** (A3), 5003–5020, 1996b.

Sandholt, P. E., Lybekk, B., Egeland, A., Nakamura, R., and Oguti, T.. Midday auroral breakup. *J. Geomag. Geoelectr.*, **41**, 371–387, 1989.

Sandholt, P. E., Moen, J., Rudland, A., and Opsvik, D.. Auroral event sequences at the dayside polar cap boundary for positive and negative interplanetary magnetic field By. *J. Geophys. Res.*, **98** (A5), 7737–7755, 1993.

Saunders, M. A., Freeman, M. P., Southwood, D. J., Cowley, S. W. H., Lockwood, M., Samson, J. C., Farrugia, C. J., and Hughes, T. J.. Dayside ionospheric convection changes in response to long-period interplanetary magnetic field oscillations: Determination of the ionospheric phase velocity. *J. Geophys. Res.*, **97** (A12), 19373–19380, 1992.

Sergeev, V. A., Sazhina, E. M., Tsyganenko, N. A., Lundblad, J. Å., and Søraas, F.. Pitch-angle scattering of energetic protons in the magnetotail current sheet as the dominant source of their isotropic precipitation into the nightside ionosphere. *Planet. Space Sci.*, **31** (10), 1147–1155, 1983.

Shelley, E. G., Sharp, R. D., and Johnson, R. G.. He^{++} and H^{+} flux measurements in the day side cusp: Estimates of convection electric field. *J. Geophys. Res.*, **81** (13), 2363–2370, 1976.

Smith, M. F. and Lockwood, M.. Earth's magnetospheric cusps. *Rev. Geophys.*, **34** (2), 233–260, 1996.

Søraas, F., 1972. ESRO IA/B observations at high latitudes of trapped and precipitating protons with energies above 100 keV. In **McCormac, B. M.**, editor, *Earth's magnetospheric processes*, pages 120–132. D. Reidel Publishing Company, Dordrecht - Holland.

Søraas, F., Aarsnes, K., Lundblad, J. Å., and Evans, D. S.. Localized enhancement of energetic particles at mid-latitudes during geomagnetic storms. *J. Geophys. Res.*, 1998. submitted.

Søraas, F., Gustafsson, G., and Borg, H.. Field line topology in the dayside cusp region inferred from low altitude particle

observations. *Planet. Space Sci.*, **28**, 525–533, 1980.

Søraas, F., Lundblad, J. Å., and Hultqvist, B.. On the energy dependence of the ring current proton precipitation. *Planet. Space Sci.*, **25**, 757–763, 1977.

Störmer, C.. *The polar aurora*. Oxford: Clarendon Press.

Thorsen, E., 1998. "Utvikling av programvare for behandling og analyse av målinger fra røntgenkameraet PIXIE på Polar-satellitten". Master's thesis, Physics Department, University of Bergen, Allegt. 55, 5007 Bergen, Norway. (In Norwegian).

Vorobjev, V. G., Gustafsson, G., Starkov, G. V., Feldstein, Y. I., and Shevnina, N. F.. Dynamics of day and night aurora during substorms. *Planet. Space Sci.*, **23**, 269–278, 1975.

Wedde, T., Skovli, G., Amundsen, R., Aarsnes, K., Lindalen, H. R., and Søraas, F.. High latitude electron and proton precipitation at different local times and magnetic activity. *J. atmos. terr. Phys.*, **35**, 2191–2203, 1973.

Winningham, J. D. and Heikkila, W. J.. Polar cap auroral electron fluxes observed with Isis 1. *J. Geophys. Res.*, **79** (7), 949–957, 1974.

Yamauchi, M., Lundin, R., Eliasson, L., Ohtani, S., and Clemmons, J. H., 1998. Relationship between large-, meso-, and small-scale field-aligned currents and their current carriers. In **Moen, J., Egeland, A., and Lockwood, M.**, editors, *Polar Cap Boundary Phenomena*, pages 173–188, P. O. Box 17, 3300 AA Dordrecht, The Netherlands. NATO Scientific Affairs Division, Kluwer Academic Publishers. ISBN 0-7923-4976-8.